LEAD HALIDE PEROVSKITE NANOCRYSTALS: PHOTOPHYSICAL AND PHOTOCHEMICAL DYNAMICS

A Dissertation
Submitted to the Graduate Faculty
of the
North Dakota State University
of Agriculture and Applied Science

By

Aaron Arthur Forde

In Partial Fulfillment of the Requirements
for the Degree of
DOCTOR OF PHILOSOPHY

Major Program:
Materials and Nanotechnology

June 2021

Fargo, North Dakota

North Dakota State University
Graduate School

Title

LEAD HALIDE PEROVSKITE NANOCRYSTALS: PHOTOPHYSICAL AND PHOTOCHEMICAL DYNAMICS

By

Aaron Arthur Forde

The Supervisory Committee certifies that this ***disquisition*** complies with North Dakota State University's regulations and meets the accepted standards for the degree of

DOCTOR OF PHILOSOPHY

SUPERVISORY COMMITTEE:

Dmitri Kilin
Chair

Erik Hobbie

Andrei Kryjevski

Simone Ludwig

Approved:

July 11,2021
Date

Erik Hobbie
Department Chair

ABSTRACT

Lead halide perovskites nanocrystals (LHP NCs) are a recent novel material of 'high-defect tolerance' that has been synthesized which have provided a new platform for opto-electronic devices, such as photovoltaics and light-emitting diodes. Development of these materials for commercial devices requires a thorough understanding of their photo-physical properties. A comprehensive understanding of photo-physical properties involves studying the interplay between light-matter interactions, which produce photo-excited charge carriers and govern radiative recombination mechanism, carrier-lattice interactions, which play a dominate role in non-radiative dynamics such as hot-carrier cooling and recombination, and the NC surface chemistry which plays an important role in passivating surface sites which can potentially act as non-radiative recombination centers.

In chapter 1 a review of the photo-physical phenomena and electronic processes which occur in materials is established and the motivation for incorporating nanomaterials into opto-electronic devise is provided. Chapter 2 describes in formal details the theoretical methods used to compute electronic structure, light-matter interactions, and carrier-lattice interactions are. Chapter 3 overviews simple physical models, such as particle-in-a-box photo-physics and two-level Redfield theory, which give intuition on how to understand the results of the research. Finally chapters 4-7 are devoted to original research on charge-carrier dynamics within a LHP NC atomistic model as free carriers, bound polarons, in the presence of surface defects, and finally in the presence of transition metal dopants.

Chapter 4 provides computational evidence of slow electron cooling due to strong electronic confinement and large spin-orbit coupling contributed from Pb^{2+} *6p* orbitals. Chapter 5 considers the effect of polaron formation on hot-carrier dynamics with the prediction of low

efficiency polaron infrared photoluminescence. Chapter 6 provides mechanism for ‘defect tolerance’ due to bright electron surface trap states that form due to polaron reorganization. Chapter 7 models dual exciton-dopant luminescence due to Mn^{2+} doping.

ACKNOWLEDGMENTS

The work presented in this dissertation would not be possible without the guidance of Dr. Dmitri Kilin. He has fostered a combination of scientific and career development which I am greatly thankful for. I am also grateful for his allowance of me pursing various ‘side-projects’ which I believe have been invaluable for my studies.

Here I would like to thank the Kilin group members. Dr. Yulun Han and Dr. Jon Vogel provided valuable comments and help early on as a graduate student. It has been a pleasure to work with David Graupner, Daniel Ramierez, Landon Johnson, Kevin Gima, and Brandon Disrud as group members over the years. They all where good company to have at the Sanibel Symposium.

I would like to thank Dr. Erik Hobbie for allowing me to pursue one of the ‘side-projects’ in his laboratory by synthesizing and characterizing LHP NCs. I have to thank Dr. Sam Brown for showing me the ropes of the optics setups along with processing procedures and Salim Thomas for always being a team-player and helping do optical measurements and processing. Thanks also to Reed Peterson and Tim Twohig (along with his doodads and gizmos) for providing company in the lab.

Thanks to Dr. Svetlana Kilina and her group members Dr. Levi Lystrom, Dr. Jabed Muhammad, Dr. Branden Gifford and Alyssa Roberts for providing stimulating group meetings and critical questions which have helped development of manuscripts and understanding of concepts.

Thanks to Dr. Andrei Kryjevski for allowing me to sit in on a semester of discussions with Braden Weight and Nathan Walker.

DEDICATION

This work is dedicated to Wildlands School for reimagining education

TABLE OF CONTENTS

LIST OF TABLES

LIST OF FIGURES

LIST OF ABBREVIATIONS

ADF ..... Angular Distribution Function

CB ..... Conduction Band

DOS ..... Density of States

IOA ..... Independent Orbital Approximation

GS ..... Ground State

KS ..... Kohn Sham

KSO ..... Kohn Sham Orbital

LED ..... Light-Emitting Diode

LHP ..... Lead Halide Perovskite

L-ES ..... Lowest Excited-State

MD ..... Molecular Dynamics

MDPL ..... Molecular Dynamics Photoluminescence

NAC ..... Nonadiabatic Coupling

NC ..... Nanocrystal

PL ..... Photoluminescence

PLQY ..... Photoluminescence Quantum Yield

PBE ..... Perdew-Burke-Ernzerhof

pADF ..... Partial Angular Distribution Function

pRDF ..... Partial Radial Distribution Function

PV ..... Photovoltaic

RDF ..... Radial Distribution Function

TEM ..... Transmission Electron Microscopy

SKSO ..... Spinor Kohn Sham Orbital

VASP ..... Vienna ab Initio Simulation Package

VB.....Valence Band

1. INTRODUCTION TO MATERIALS SCIENCE AND THE ROLE OF NANOTECHNOLOGY

Overall philosophy of materials science. The vast time and length scales involved in characterizing a material. Materials science in opto-electronic devices. Motivation for incorporating nanomaterials into opto-electronic devices. Kinetics of charge-carriers in opto-electronic devices. interfacial dynamics that play primary roles in the excited-state dynamics of charge-carriers. Experimental characterization of nanomaterials and charge-carrier dynamics. Emergence of atomistic simulations as an additional tool for characterization. Novel lead-halide perovskite nanocrystals.

1.1. Paradigm of Materials Science

There is a branch of philosophy known as materialism. Its claim is that the only thing that exists is composed of matter and that all of the 'macro scale' objects we interact with are emergent phenomena as a result of interactions between fundamental units of matter. In this sense, materials science is the application of the scientific method (prediction, hypothesis, measurement, and analysis) from a set of diverse backgrounds (physics, chemistry, and biology) towards understanding the mechanisms which underlay a materials fundamental properties. From the understanding of how a materials physical structure and chemical composition on the 'micro' scale impacts the emergent macroscopic properties it is then possible to engineer a materials properties to perform a specified function which provides benefit and utility to society. Overall, this process is summarized as the interrelations between how *processing* impacts a materials *structure-property relationships* which are determined through *characterization*.

One of the most challenging aspect of materials science is having a precise control or understanding of a materials properties over the vast length scales and time scales involved. **Figure 1.1** illustrates the vast length and time scales to consider when trying to work with a specific material. On the very small length scales (nanometers to micometers) and timescales (femtoseconds to nanoseconds) a materials properties are dominated by molecular interactions, where molecules and atoms are composed of discrete parts, while at larger length (millimeters to meters) and timescales (microseconds to seconds) materials are assumed to be fully continuous.

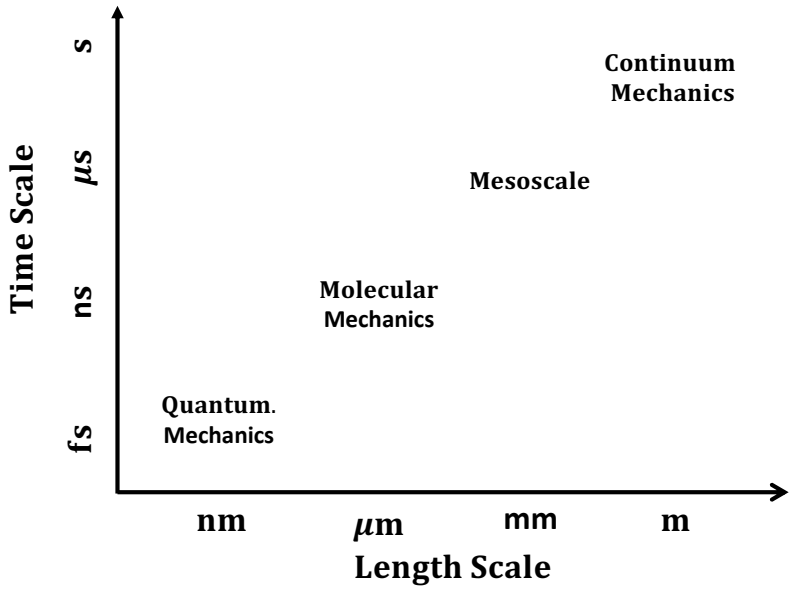

Figure 1.1: Length scale and time scales to consider when processing a material or characterizing a materials properties. The time dimension spans a space of 10^{15} and the spatial dimension spans 10^{9}.

Materials can be broadly classified into three categories: metals, polymers, and ceramics. Within ceramics, the class of materials referred to as semi-conductors form the core of electronic devices. This dissertation will focus on the optical and electronic properties of semiconductor nanomaterials. The goal of this chapter is to overview the main operating principles of opto-electronic devices, describe the microscopic phenomena leading to charge-carrier relaxation

kinetics, and how computational simulations can be an additional tool to characterize material structure-property relations and the dynamics of charge-carriers in the material.

1.2. Opto-Electronic Devices

One of the most influential technologies to date has been opto-electronic devices, where the opto prefix refers to optical signals. Opto-electronic devices are based on the principle that light absorbed by a material can generate electronic currents and voltages which can be converted into useful work. Conversely, electrical currents and voltages can also be converted into light. Some of the more well known commercial applications are photovoltaics (PVs), which convert sunlight into electricity, and light-emitting diodes (LEDs), which converts electricity into light. More generally LEDs and PVs are classified as photo-diodes.

Fundamentally, the operation of opto-electronic devices rely on the manipulation of electronic charge-carriers (i.e. electrons and holes). Charge-carriers can be generated in a semiconducting material by either electrical pumping, such as being apart of a circuit, or by photo-excitation, such as sunlight. Once generated, the kinetics of relaxation and recombination pathways of the charge-carriers will be one of the most important processes which determine the overall device efficiencies. Generally, there are two competing relaxation pathways: radiative and non-radiative. Radiative relaxation involves the emission of light (photons) and non-radiative involves the emission of heat (phonons). For solar cells it is desirable to minimize the non-radiative and radiative lifetimes, relative to the rate of charge extraction from the material, so that the maximum amount of useable power can be generated. For LEDs it is desirable to minimize the non-radiative relaxation and maximize the radiative recombination so that the maximum amount of injected/generated charges are converted to useful light emission.

To persuade charge-carriers to flow in a desired direction requires an engineered device architecture. The primary components are the (i) active material which is the primary layer which absorbs or emits light, (ii) electron or hole transport layers which interface with the primary material to either extract (for PVs) or inject (for LEDs) charge-carriers, and (iii) metal contacts to increase the conductivity. For silicon PVs, the active layer is composed of p and n doped silicon where the interface produces a pn-junction. The junction serves as a region to spatially separate negative and positive charges and the doped silicon regions provide enhanced conductivity for the charges to migrate. Overall the important variables to consider when constructing an opto-electronic device are the kinetics of charge-carrier recombination pathways within the active material, charge transfer at the interface between the active material and the charge transport layers, charge transport in the transport layers, and charge extraction/injection at the contact layers.

Taking into consideration the numerous potentials for energy losses within a typical single pn-junction silicon solar cell there is a maximum theoretical efficiency known as the Shockley-Queisser (SQ) limit. The SQ limit places the maximum efficiency at ~29%. There have been a few proposed methods to increase the maximum possible efficiency, such as extraction of hot carriers before thermalization to reduce heat loss, generate multiple charge-carriers from a single absorbed photon, and down conversion of high energy light, which generates significant heat loss, into lower energy light.

The motivation of incorporating nanomaterials as the active materials in these devices is that they are predicted to go beyond the SQ limit and increase the maximum possible efficiency for the devices. The next two sections will look at how nanomaterials provide a tunable

electronic structure and the possibility of engineering the kinetics of charge-carriers within the nanomaterial.

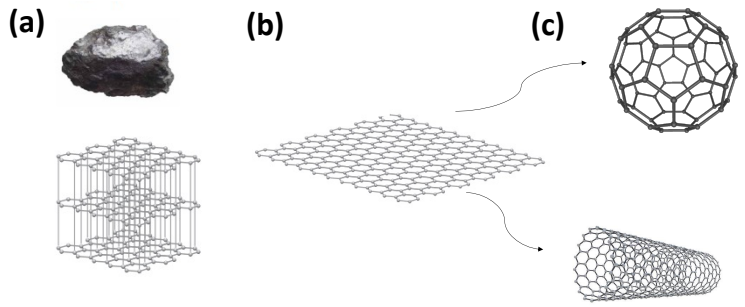

Figure 1.2: Examples of nanomaterial dimensionality for fullerene compounds. (a) 3D graphite which is composed of single layers of conjugated carbon sheets which stack on top of each other. (b) 2D graphene (c) the 2D graphene can be wrapped into a 0D material, such as the buckyball (top), or a 1D material, such as a carbon nanotube (bottom).

1.3. Dimensionality of Nanostructures: Effect on Opto-Electronic Properties

One of the defining features of a nanomaterial is their 'dimensionality'. Dimensionality refers to the length scale for each spatial dimension of the nanomaterials structure. The typically defined cutoff distance (somewhat arbitrarily chosen) for a structure to show reduced dimensionality is 100 nm (source). Thus a 2D material which shows two dimensions longer than 100 nm and one dimension less than 100nm, a 1D material shows two dimension longer than 100 nm and two dimensions less than 100nm, and a 0D material has all three dimensions less than 100 nm. A prototypical architype for material dimensionality are the fullerenes, which are structures that only contain carbon but vary in their nanostructure. This is illustrated in **Figure 1.2** which shows the bulk 3D graphite, 2D material graphene, 1D material carbon nanotube, and a 0D buckyball.

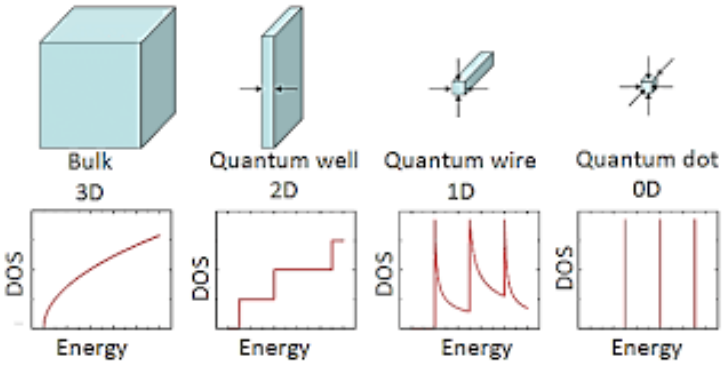

Figure 1.3: Density of electronic energy levels which changing dimensionality of the nanomaterial.

Although the 100 nm classification is arbitrary, there are distinct differences in the electronic and optical characteristics of the nanomaterial as a function of their dimensionality. This is due to the spatial confinement of charge-carriers within the nanomaterial. Spatial confinement can have two prominent effects: reduction in the degrees of freedom for spatial movement and the confinement of charge-carriers below their 'natural' size. The consequences of the reduced degrees of freedom are show in **Figure 1.3** which show that the reduced dimensionality affects the distribution of possible energy states that charge-carriers can occupy. From this perspective it can be seen that for opto-electronic devices there are attractive features of controlling the dimensionality of the nanomaterial where 2D and 1D materials could provide benefits for controlled charge-transport, best suited for PVs, and 0D materials could be tuned for highly controlled light-emitting applications, such as LEDs and bioimaging.

An important consequence of reducing the dimensionality of a nanomaterial is increasing the surface-to-volume ratio. Surfaces are inherently higher in energy than the bulk periodic lattice and are prone to degradation. This makes surface effects, such as surface vacancy defects, more pronounced. For opto-electronic applications the most common impact of the surface is the introduction of undercoordinated surface atoms (ie dangling bonds). If a surface atom is

undercoordinated an electronic ‘trap-state’ can be introduced in the nanomaterial. Trap-states are considered undesirable as they are sources for non-radiative recombination which reduce the overall efficiencies of the device.

Here I will finish this section with an interesting case study of how a nanostructured materials properties can be fundamentally different than a bulk material. Bulk silicon, the predominate material for commercial photovoltaics, shows high efficiencies as a photo-voltaic cell which can largely be attributed to its indirect electronic bandgap. This is due to charge-carriers having long microsecond non-radiative lifetimes due to its indirect bandgap (which requires both energy and momentum conservation for the transition to occur, a low probability 2nd order process). The long non-radiative lifetime allows the charge-carriers to be extracted from silicon into the circuit instead of being turned into heat waste. But when silicon is fabricated as a confined nanostructure it has been observed that they are able to emit photoluminescence with reasonable efficiencies up to 60% [1]. Developing large scale high-quality fabrication for silicon nanostructures could provide a technological breakthrough for silicon based photonic devices which would not be possible for bulk silicon.

Silicon provides an excellent example of how a materials properties can be modulated based on their nanostructure. Manipulating a materials nanostructure provides two possible ways to alter its opto-electronic properties: altering the density of electronic states by making energy levels more discrete with increased spatial confinement and altering the rates of recombination with increased confinement. In the next section I will explore in more depth the various types of radiative and non-radiative relaxation pathways.

1.4. Relaxation Kinetics: Carrier-Phonon and Carrier-Carrier Interactions

When considering the atomistic description of opto-electronic processes there are three processes to distinguish. First is light-matter interactions which describe the absorption and emission of light by matter. Second is carrier-carrier interactions. Since charge-carriers can be either positive (holes) or negative (electrons) there can be various types of carrier-carrier interactions. Formation of a bound exciton, through attraction between positive and negative charges, is one form of carrier-carrier interaction. Positive-positive and negative-negative carrier interactions, which contribute to exciton-exciton interactions and result in Auger recombination, are not stable as one should expect from their Coulomb repulsion and have a very fast non-radiative recombination. The third is carrier-phonon interactions. Carrier-phonon interactions allow the non-radiative exchange of energy between an electronic charge-carrier and the phonon lattice vibrations within the material. There are responsible for carrier-cooling after photo-excitation and non-radiative recombination.

The initial step of photo-induced charge-carrier dynamics is optical absorption which occurs on the femtosecond (fs) timescale. After absorption occurs non-radiative relaxation events occur which lead to a meta-stable excited-state state. These two processes are decoherence, a quantum mechanical correlation which occurs on the 10-100 fs timescale, and carrier-cooling, which is vibrational relaxation where the charge-carriers deposit energy into the lattice which emit phonons. Once the carrier-cooling is completed the charge-carriers relax to the lowest energy excited-state. From this state, the carriers can recombine radiatively or non-radiatively. Radiative relaxation typically occurs on the scale of 1-10 ns. The relative timescales are depicted in **Figure 1.4.**

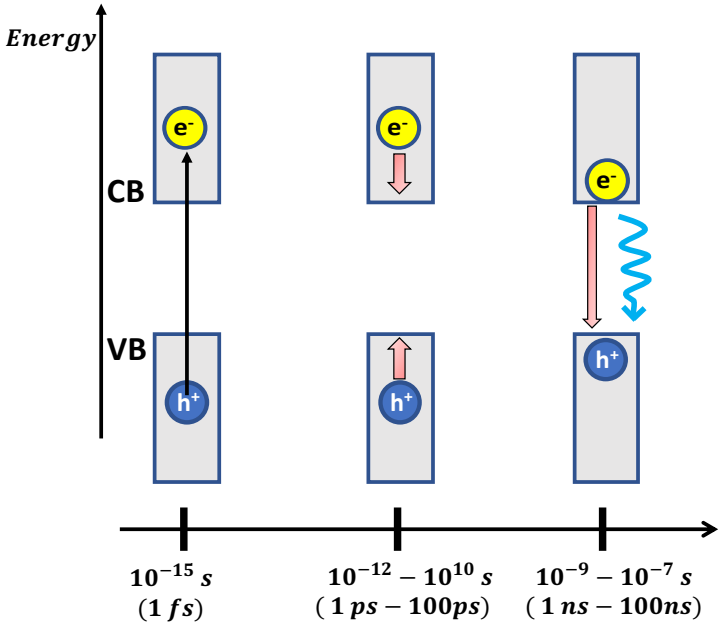

Figure 1.4: Illustration of photo-induced dynamics of charge-carriers in a semiconductor. From left to right represents absorption (black arrow), non-radiative hot-carrier cooling, and non-radiative and radiative recombination. Red (blue) arrows represent non-radiative (radiative) relaxation events.

The spatial dimensions of the nanostructures relative to 'size' of the charge-carriers can have a large impact on the interactions which determine the dominate kinetic relaxation pathways. Within a bulk material, negative (electrons) and positive (holes) charge carriers can interact with one another through the Coulomb interaction to form quasi-particles known as excitons. The spatial size of the exciton is referred to as the Bohr radii r_{Bohr}. When the spatial dimension of the nanomaterial becomes smaller than the Bohr radii this introduces confinement effects, such as blue-shifting of the electronic bandgap[2] and increases in the radiative relaxation [3].

In the case of a single exciton, spatial confinement can be seen to have beneficial aspects for increasing the efficiency of luminescence. Ideally, increasing the number of excitons in the nanostructure would proportionally increase the resultant luminescence intensity. But in scenarios when multiple excitons reside in the same confined nanostructure new non-radiative

relaxation pathways become accessible due to exciton-exciton interactions. These new relaxation pathways, known as Auger recombination and illustrated in **Figure 1.5(a)**, compete with the beneficial single-exciton relaxation kinetics. Non-radiative Auger recombination occurs on ultra-fast timescales (~10-100 fs) relative to photoluminescence (~1 ns) which limits the potential for optical gain and efficiency of using confined nanostructures as media for diode lasers. Within the last ten years progress has been made in solving this issue with creative nanomaterial architectures designed to suppress Auger recombination [4 5 6].

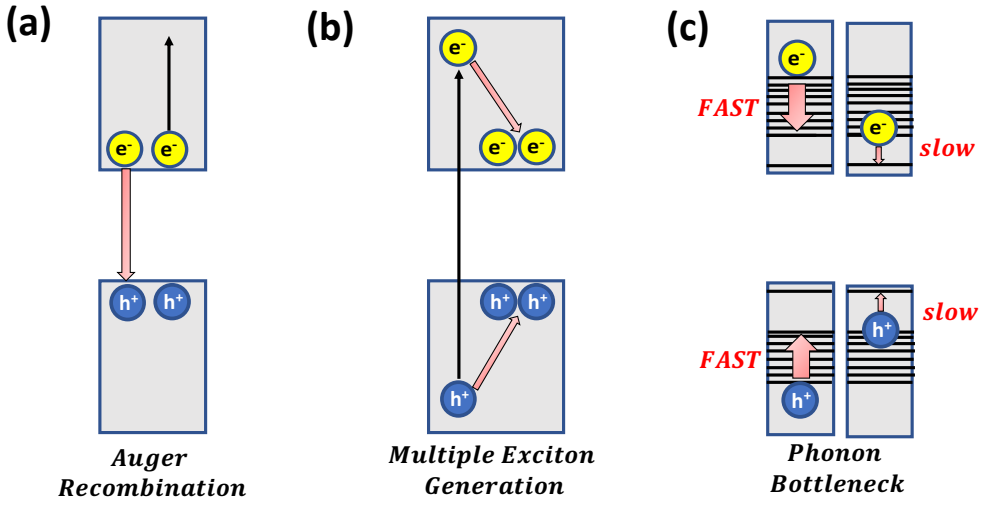

Figure 1.5: (a)-(b) Carrier-carrier and **(c)** carrier-phonon mediated relaxation pathways in semiconductor materials.

From the perspective of using strongly confined nanostructures for lasing, Auger recombination seems to be purely detrimental. But from a parallax view the Auger process has been theorized to possibly benefit PVs. Auger recombination is the rate from a low lying multiple exciton state to a high energy single exciton (or trion) state. In principle it is possible to try and start from a high energy single exciton, by photo-exciting the nanostructure with energies of integer multiples of the bandgap, and produce a low lying multiple exciton state. This process, known as multiple exciton generation and illustrated in **Figure 1.5(b)**, has been experimentally

observed in NCs of various chemistries[7-8] [9-10] [11] and has been implemented in various solar cells [12] [13] showing enhanced power conversion efficiencies.

The last kinetic relaxation phenomena to discuss is the prediction of a 'phonon-bottleneck', illustrated in **Figure 1.5(c)**. This phenomena was predicted to occur in strongly confined nanomaterials where there is a mis-match between the 'large' energetic offsets between electronic energy levels of the nanomaterial and the 'small' phonon energies in the lattice. The mis-match would result in a significant decrease of the hot carrier-cooling rates due to the inability of the charge-carrier to dissipate energy which the lattice would be able to absorb[14]. The predicted result is that the non-radiative relaxation would slow down by orders of magnitude and allow for hot-carrier extraction. Note that this process is distinct from Auger recombination type processes in that the phonon-bottleneck involves only a single exciton while Auger recombination is a multi-exciton process. Experimental signatures of the phonon-bottleneck and Auger recombination will look similar in time-resolved spectroscopic studies making it hard to distinguish. The expectation would be that at low excitation densities Auger recombination is limited and can isolate for the phonon-bottleneck. The phonon-bottleneck effect is still an open subject which has been elusive to determine experimentally. One proposal is that due to the strong coupling of electron and holes an Auger-like process occurs where one charge is able to overcome the phonon-bottleneck by depositing the excess energy into the opposite charge [15]. Other rationalizations have invoked the coupling of the charge-carriers to surface states which provide pathways that bypass the bottleneck [16] [17]. A recent work has claimed that doping mediated ultra-fast uncoupling of the charge-carriers has allowed experimental observation of the bottleneck [18].

1.5. Characterization of Nanomaterials and Dynamics of Charge-Carriers: Emergence of Atomistic Simulations

For nanomaterials there are three primary characteristics to consider: physical structure, chemical composition, and electronic structure. Physical characterization can give information about the size distributions, morphology, topology, and crystal structure of the nanomaterial. Size distributions and morphology can be quantified using methods such as TEM and DLS. TEM irradiates the sample with x-rays and collects the transmitted rays to construct the image, with an example shown in **Figure 1.6(a)-(b)**, while DLS measures the scattering of monochromatic light, in the UV-VIS range, over time and uses correlation functions (with respect to signal intensity) to determine the size distribution. Topology can be assessed by the use AFM and STM. AFM uses a nanometer scale cantilever which rasters the materials surface and generates a topology by the deflection force from the surface while STM uses tunneling current to raster the surface. Chemical characterization, such as mass spectroscopy and EELS, can give information about the nanomaterials chemical composition and stoichiometry. In mass spectroscopy the sample is thermally atomized and then ionized. The atomic species is then determined by the magnitude of deflection when passed through an electric/magnetic field. EELS can give information about a materials chemical composition by measuring inelastic core-shell excitations.

CW UV-VIS spectroscopy can give information on the nanomaterials electronic structure. The electronic bandgap can be estimated using the Beer-Lambert law to determine the wavelength dependent extinction. Absorbance is found from the natural log of transmittance. If the sample is photoluminescent its PLQY can be determined using an integrating sphere. Integrating spheres are designed to minimize the absorption of the excitation source and luminescence from the sample so that the spectrometer receives the full signal. Corrections have

to be implemented to account for wavelength dependent dispersion as the signal passes through optical fibers. From the spectrometer reading the ratio of the power spectrum of the luminescence and the absorbance gives the samples PLQY. An example of a nanocrystals absorption and PL spectra are shown in **Figure 1.6(c).**

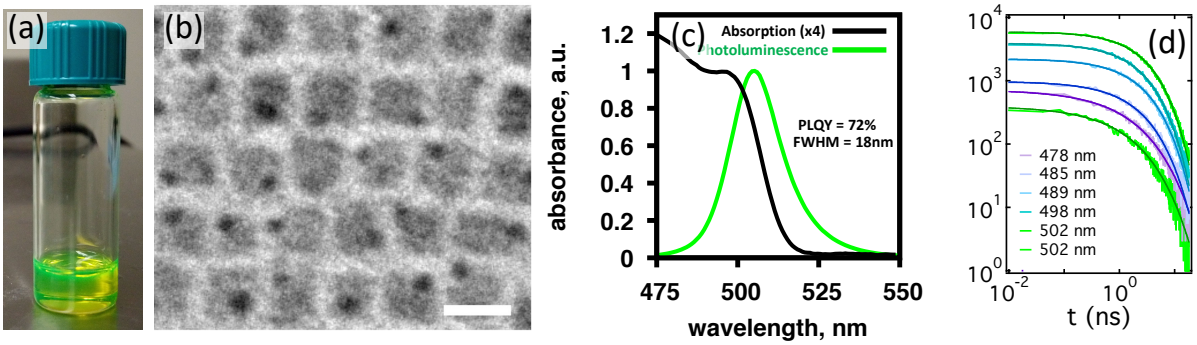

Figure 1.6: (a) Colloidal sample of $CsPbBr_3$ NCs which are deposited onto a graphene grid for **(b)** visual analysis of individual NCs using TEM (scale size is 5 nm). **(c)** Comparison of absorption (black) and photoluminescence spectrum (green) for $CsPbBr_3$ NCs. **(d)** Photoluminescence decay for $CsPbBr_3$ NCs as a function of emission wavelength. **Figures (a)-(c)** are from Dr. Erik Hobbies lab and **(d)** was measured in Dr. Richard Schallers lab.

To characterize the excited-state dynamics of charge-carriers, such as photoluminescence lifetime and transient absorption, time-resolved spectroscopic measurements are needed which requires the use of pulsed lasers. Time-Correlated Single Photon Counting is a method which pumps the sample into an excited-state with a pulsed laser and then measures the time between excitation and when a photon hits the detector from the sample photoluminescence. After measuring the time offset between excitation and photoluminescence the intensity decay will emerge which can be fit to exponential decay models. An example PL decay curve is shown in **Figure 1.6(d)**. Note that this experiment measures both the radiative and non-radiative decay, but when combined with quantum yield experiments the intrinsic radiative lifetime can be determined. In transient absorption experiments the sample is first 'pumped' with a pulsed laser into the excited-state and then 'probed' with a white-light source to measure absorption while the sample is in the excited-state. By changing the offset times between pump and probe

measurements it is possible to infer changes of occupations in time. measure carrier-cooling and MEG.

With the advancement of supercomputing capabilities over the last twenty years, *ab Initio* atomistic simulations have become a complementary approach for characterizing nanomaterials. Commercial implementation of software that computes electronic structure, such as Gaussian and VASP, has provided a platform to model photo-induced dynamics of charge-carriers in nanostructured materials. Atomistic simulations also provide another way to investigate structure-property relationships.

Typical implementations of electronic structure software rely on the adiabatic Born-Oppenheimer approximation which assumes that atomic displacements do not induce changes in electronic occupations. For modeling phonon-induced non-radiative relaxation one needs to go beyond the Born-Oppenheimer approximation and include the contributions of non-adiabatic coupling. Modeling of phonon-induced non-radiative relaxation has provided valuable insights into the dynamics at complex interfaces. Some of the earliest reports of atomistic based non-adiabatic simulations where of molecular adsorbates onto TiO_2 surfaces[19-21], a common architecture for dye-sensitized solar cells where the molecular adsorbate is photo-excited with the photo-induced electron injected into TiO_2. Femtosecond spectroscopy experiments found that electron injection occurred on the ultrafast ~10 fs timescale. The non-adiabatic simulations showed strong agreement with injection rates very comparable to the experiments and gave insight that the injection was due to vibrationally induced non-adiabatic relaxation as opposed to adiabatic transfer or coherently driven transfer. Thus the collaborations between ultra-fast spectroscopists and computational chemists have allowed for knowledge growth in the interfacial

processes that play primary roles in the excited-state dynamics of charge-carriers for important opto-electronic devices.

1.6. Lead Halide Perovskites: Novel Material For Opto-Electronic Devices

Lead halide perovskites are a semiconducting material which have found a renewed focus over the last 15 years in the energy community. Perovskite refers to the specific crystalline structure originally named after calcium titanate ($CaTiO_3$) with an overall general chemical composition of $A^+B^{2+}X^-_3$. Lead-halide perovskites are semiconductors where $B^{2+}=Pb^{2+}$, $X^-=(F^-,Cl^-,Br^-,I^-)$, and the A^+ cation can be composed of either inorganic alkali metals Cs^+ or organic molecules such as methylammonium $CH_3NH_3^+$. The initial report in 2009 for using LHP in a dye-sensitized PV architecture where the LHP sensitized TiO_2 with a solar energy conversion efficiency of 3.8% [22]. From that point there where substantial developments in engineering LHP PVs with increased conversion efficiencies in the form of thin-film LHP [23] [24], 0D nanostructured quantum dots[25], and 2D RP phased LHP [26]. Currently, LHPs used in research based cell devices have shown a maximum conversion efficiency of 25.5% which is comparable to single crystal silicon at 27.6%.

One of the curious aspects of LHP materials is that they can be fabricated using solution processing which are notorious for having relatively large defect densities, such as point defects. In conventional semiconductor materials, such as silicon and chalcogenides, defects provide deep trap states which reduce their functionality for PVs and LED applications. Despite these defects LHP based opto-electronic devices show competitive efficiencies LHPs are distinct from these materials in that they are a ‘soft’ semiconductors. This is evident by their Youngs Modulus which is about an order of magnitude lower than silicon[27] meaning they are much more deformable. This has led to speculation that polarons, the coupling of charge-carriers to the LO

phonon modes, could allow for high opto-electronic functionality even with the presence of defects [28].

The material of focus for this dissertation will be lead-halide perovskite 0D nanocrystals. From their initial report in 2015 it was found that they show high PLQYs with color tune able PL by changing halide composition with very high color purity [29]. From the initial study these materials have been had a spotlight in the research community to understand their unusual photo-physics and liable surface chemistry. The focus of the atomistic simulations in this dissertation will focus on the role of electron-phonon couplings of hot-carriers in a strongly NC and comparing the impact of polaron formation and surface chemistry induced defects on the opto-electronic properties.

1.7. Conclusion

This introductory chapter had the following goals: introduce the reader to the philosophy of materials science, basic operating principles and design of opto-electronic devices, the promise of using nanomaterials as the active components in opto-electronic devices, and the most prominent interactions within the nanomaterial. The prominent interactions are light-matter, which describe absorption and emission of light, charge-carrier – lattice, which describe thermal equilibrium between lattice vibrations and charge-carrier energies, and carrier-carrier interactions, which describe multiexciton processes. A brief review of nanomaterials and charge-carrier dynamics characterization was also presented which outlined the utility of using atomistic simulations to investigate photo-induced processes in nanomaterials. These paradigms will be applied to investigate the opto-electronic properties of LHP NCs. Chapter 2 will describe the methodology used to compute photo-induced radiative and non-radiative relaxation. Chapter 3

will provide chemical and physical background for the material system of focus for this dissertation. Chapters 4-7 will be on original published research.

2. AB INITIO METHODOLOGY FOR ELECTRONIC STRUCTURE AND PHOTO-INDUCED EXCITED-STATE DYNAMICS

2.1. Introduction

The purpose of this chapter is to give an overview and definitions of terms for the foundational theories used for *ab Inito* modeling used in this dissertation. Then in each subsequent chapter there will be a methods section which details the additional novelties that where implemented for each specific study. This section will provide background for three important elements: electronic structure, light-matter interactions, and electron-phonon interactions. In the final section all three aspects will be combined to describe the treatment of photo-induced radiative and non-radiative dynamics.

2.2. Density Functional Theory

Electronic structure for the atomist models investigated is found from solving the fictious one electron Kohn-Sham (KS) equation[30] from density function theory[31]:

$$[-\frac{h}{2m}\nabla^2 + v^{eff}(\vec{r})]\,\varphi_i^{KS}(\vec{r};\vec{R}) = \varepsilon_i[\rho(\vec{r});\vec{R}]\,\varphi_i^{KS}(\vec{r};\vec{R}) \tag{2.1}$$

$\varphi_i^{KS}(\vec{r};\vec{R})$ is the i^{th} KS orbital that depends on electronic coordinates $\vec{r}$ and parametrically on nuclear coordinates $\vec{R}$, $\varepsilon_i([\rho(\vec{r});\vec{R}])$ is the energy of the i^{th} KS orbital which is a functional of the electron density $\rho(\vec{r})$ and also depends parametricly on nuclear coordinates $\vec{R}$. The $-\frac{h}{2m}\nabla^2 + v^{eff}(\vec{r})$ term is analogous to the one electron Hamiltonian for the Schrodinger Equation, but with a modified external potential $v^{eff}(\vec{r})$ which is a functional of the electron density $\rho(\vec{r})$.

$$v^{eff}(\vec{r}) = v_{ext}(\vec{r};\vec{R}) + e^2\int d\vec{r}'\,\frac{\rho(\vec{r}')}{|\vec{r}-\vec{r}'|} + \frac{\delta E_{xc}[\rho(\vec{r})]}{\delta\rho(\vec{r})} \tag{2.2}$$

Here $v^{eff}(\vec{r})$ includes the external potential $v_{ext}(\vec{r};\vec{R})$ which contains information on electron-nuclei interaction, the Hartree term which describes the Coulomb electrostatic interaction of the electron and the atomic nuclei, and the many-electron exchange-correlation interactions $v_{xc}(\vec{r}) = \frac{\delta E_{xc}[\rho(\vec{r})]}{\delta\rho(\vec{r})}$. The total electron density $\rho(\vec{r})$ is found by summing together the electron density of all electrons N_{elect}.

$$\rho(\vec{r}) = \sum_i^{N_{elect}} \varphi_i^{KS}(\vec{r})^* \varphi_i^{KS}(\vec{r}) \tag{2.3}$$

The Coulomb term and the exchange-correlation potentials are functionals of the electronic density $\rho(\vec{r})$: $V_{xc}(\vec{r}) = V_{xc}[\rho(\vec{r})]$ and $V_{ee}(\vec{r}) = V_{ee}[\rho(\vec{r})]$. Since the potential is determined by the electronic density this allows for the Kohn-Sham equations to be solved self-consistently to minimize the total energy of the system with respect to nuclear coordinates of the atomistic model $\frac{dE_{total}[\rho(\vec{r});\vec{R}]}{d\vec{R}} = 0$.

An issue arises due to the fact that the Kohn-Sham equations are exact, but the exact functional form of $V_{xc}[\rho(\vec{r})]$ is unknown and has to be approximated. The most common approaches for approximating the exchange-correlation functional are local-density approximations, generalized-gradient approximations[32], and hybrid functionals[33-34] which include portions of the exact Hartree-Fock exchange interaction into the functional dependence.

A note on the basis used to construct the single-electron KS orbitals. For the work done in the dissertation the KS orbitals are constructed using a plane-wave basis set

$$\varphi_{i,\vec{k}}^{KS}(\vec{r}) = e^{i\vec{k}\vec{r}} \sum_{|\vec{G}|\leq|\vec{G}_{cut}|} C_{\vec{G}i,\vec{k}} e^{i\vec{G}\vec{r}} \tag{2.4}$$

where $\vec{k}$ is the momentum vector in reciprocal space, $\vec{G}_{cut}$is the cut-off frequency (energy) for the plane-wave expansion. For the work in this dissertation, the calculations are done on a spatially confined nanocrystal where momentum dispersion is ill-defined. This means all

calculations are done at a single k-point and the momentum dependence of the KS orbital is dropped.

Also note that the external potential from DFT also uniquely determines the nuclear coordinates which minimizes the total energy of the system. To quantify the position of nuclear coordinates radial distribution functions (RDFs) are used

$$g(r) = \frac{1}{4\pi r^2}\frac{dn}{dr} = \frac{1}{4\pi r^2}\sum_{IJ}\delta\left(r - \left|\vec{R}_I - \vec{R}_J\right|\right) \tag{2.5}$$

where n is the coordination number, $\vec{R}$ are nuclear coordinates, and r represents radial distances from a specified ion.

The main takeaway from this section is that though the self-consistent DFT procedure we use eigenvalues ε_i and eigenvectors $\varphi_i^{KS}(\vec{r})$ as the electronic basis to compute observables for light-matter and electron-phonon interactions, as described in the next sections. For the actual work done in this dissertation a spinor Kohn-Sham orbital basis is used to account for strong spin-orbit coupling interactions. This will be described in later chapters.

2.3. Light-Matter Interactions

Absorption and emission of electro-magnetic (EM) radiation serves as the basis for many technologies. Solar cells operate by absorbing solar energy, creating electron and hole charge carriers in the semiconductor, and transforming those charge carriers into electrical potential. Light-emitting diodes operate by applying an electric potential to a semiconductor, resulting in the injection of charges into the semiconductor, and having the semiconductor emit EM radiation at specific frequencies to generate pure colors. Development is being done to use opto-electronic components to process and store digital data.

Here I will start by describing the first-principles treatment of ‘matter’, the EM field, and their interaction. Then approximations will be made so that the ‘matter’ will be described by

first-principles, through DFT, but the EM fields will be described classically though Maxwells equations. This formalism is commonly known as mixed quantum-classical description.

2.3.1. 2nd Quantization. Formalism – Jaynes-Cumming Hamiltonian

The coupling of quantized modes of the EM field couple to the dipoles of the atom are found through the following Hamiltonian

$$H = H_{atom} + H_{field} + H_{interaction} \tag{2.6}$$

the atom Hamiltonian is approximated as a two level system

$$H_{atom} = E_g\ |g\rangle\langle g| + E_e|e\rangle\langle e| \tag{2.7}$$

where E_g and E_e are the eigen-energies of the ground and excited-state with $|g\rangle$ and $|e\rangle$ are the eigenstates of the ground and excited-state. The electric field Hamiltonian is

$$H_{field} = \hbar \sum_{\vec{k},\lambda} \omega_{\vec{k}} \left(\hat{a}^{\dagger}_{\vec{k},\lambda} \hat{a}_{\vec{k},\lambda} + \frac{1}{2} \right) \tag{2.8}$$

where $\hat{a}^{\dagger}_{\vec{k},\lambda}$ and $\hat{a}_{\vec{k},\lambda}$ are the bosonic creation and annihilation operators for vibrational mode $\vec{k}$ with polarization state λ. The interaction Hamiltonian between the quantized electro-magentic field $\hat{E}$ and the dipoles of the atom $\hat{d}$, in the rotating wave approximation (RWA), is

$$H_{interaction} = \hbar \sum_{\vec{k},\lambda} g_{\vec{k},\lambda} (\hat{\sigma}_{+} \hat{a}_{\vec{k},\lambda} + \hat{\sigma}_{-} \hat{a}^{\dagger}_{\vec{k},\lambda}) \tag{2.9}$$

where $\hat{\sigma}_{+}$ and $\hat{\sigma}_{-}$ are fermion raising and lowering operators and $g_{\vec{k},\lambda}$ is the coupling constant

$$\hbar g_{\vec{k},\lambda} = i \sqrt{\frac{2\pi\hbar\omega_k}{V}} \left\langle e \left| \hat{\vec{d}} \right| g \right\rangle \cdot \vec{u}_{\vec{k},\lambda} \tag{2.10}$$

where $\vec{u}_{\vec{k},\lambda}$ are the orthogonal modes of the field, V is the volume of the cavity, and $\hat{\vec{d}}$ is the dipole operator. As a simple physical model it can be assumed that the atom is placed in a cavity that allows only a single mode of the quantized EM field to interaction with the atom. This allows to drop the summations and write the Jaynes-Cumming Hamiltonian H_{JC} as

$$H_{JC} = \hbar\omega_c \left(\hat{a}^{\dagger}{}_c \hat{a}_c + \frac{1}{2}\right) + E_g\,|g\rangle\langle g| + E_e|e\rangle\langle e| + g_c(\hat{\sigma}_+ \hat{a}_c + \hat{\sigma}_- \hat{a}^{\dagger}{}_c) \qquad (2.11)$$

The utility of the Jaynes-Cumming Hamiltonian is that it allows to describe the time-evolution of coherent field states which is necessary for describing quantum-optics phenomena, such as vacuum collapse and revival Rabi oscillations. When considering the coupling of multiple atomic dipoles to the coherent field, such as a superlattice of quantum dots, to a cavity EM mode it is possible to describe superradiance, an enhancement of spontaneous emission due to coherent coupling of dipoles.

For this thesis I will focus only the interaction strength of the coupling of an EM field to the atomic dipole and neglect coherences. This will be described in the mixed quantum-classical treatment described next.

2.3.2. Quantum-Classical Treatment: Transition Dipoles and Oscillator Strengths

Light-matter interactions are treated semi-classically where EM waves are treated classically and the electronic levels of our atomistic models are treated quantum mechanically using DFT.

With the semi-classical Hamiltonian

$$H = \frac{(\vec{p} + e\vec{A}(\vec{r},t))^2}{2m} - V(\vec{r}) \qquad (2.12)$$

where $\vec{A}(\vec{r},t)$ is the vector potential of the EM field and $V(\vec{r})$ is the spherically symmetric Coulomb potential lead to matrix element $\left\langle \varphi_i^{KSO}(\vec{r})\,|e^{\frac{i\omega}{c}\vec{r}}\,\hat{\epsilon}\,\vec{p}\;\,|\varphi_j^{KSO}(\vec{r})\right\rangle$ which connects two quantum states due to resonant EM radiation can be simplified using the electric dipole approximation[35]. The exponential term can be expanded in a Taylor series $e^{\frac{i\omega}{c}\vec{r}} = 1 - \frac{i\omega}{c}\vec{r} + \cdots$

using the relation $\frac{\omega}{c} = \frac{1}{\lambda}$ it can be seen that if the wavelength λ of the radiation field is much longer than the physical dimension $\vec{\boldsymbol{r}}$ of the absorbing material the exponential term can be truncated to 0th order $e^{\frac{i\omega}{c}\vec{\boldsymbol{r}}} \approx 1$. This simplifies $\left\langle \varphi_i^{KSO}(\vec{r}) \left| e^{\frac{i\omega}{c}\boldsymbol{r}} \, \vec{p} \, \right| \varphi_j^{KSO}(\vec{r}) \right\rangle \approx$ $\left\langle \varphi_i^{KSO}(\vec{r}) \mid \vec{p} \, \left| \varphi_j^{KSO}(\vec{r}) \right\rangle \right.$ which can be transformed to $\left\langle \varphi_i^{KSO}(\vec{r}) \mid \vec{r} \, \left| \varphi_j^{KSO}(\vec{r}) \right\rangle \right.$ using the momentum-energy commutation relationship. The value $e\left\langle \varphi_i^{KSO}(\vec{r}) \mid \vec{r} \, \left| \varphi_j^{KSO}(\vec{r}) \right\rangle \right.$ represents the matrix elements for static dipoles (diagonal elements) and transition dipoles (off-diagonal elements) which are used are used to calculate oscillator strengths, where e is the charge of the electron.

As a first order approximation, optical transitions between electronic states can be considered in the independent orbital approximation (IOA)[36-37] which neglects the Coulombic correlation between photo-excited electron-hole pairs. For strongly confined particles, such as an exciton in a quantum dot that has a radial dimension smaller than the material dependent Bohr radius, the IOA can be considered as a good approximation for transition dipoles and transition energies. This is due to the orbital kinetic energy of the charge carrier being more significant than the Coulomb potential energy[38]. Higher order analysis of optical transitions, including the photo-excited electron-hole Coulomb interaction, requires computing transition densities using methodologies such as linear-response time-dependent DFT (TD-DFT) or the Bethe-Salpeter equation[39]. For the purposes of this dissertation the author will use the IOA approximation.

Within the DFT framework transitions dipoles $\langle \vec{D}_{ij} \rangle$ (eq 2.13), oscillator strengths of transition f_{ij} (eq 2.14), and resultant absorption spectra $\alpha^{KSO}(\varepsilon)$ (eq 2.15) can be expressed as[40-41]

$$\langle \vec{D}_{ij} \rangle = \mathrm{e}\left\langle \varphi_i^{KSO}(\vec{r}) \mid \vec{r} \, \left| \varphi_j^{KSO}(\vec{r}) \right\rangle \right. = e\int d\vec{r} \varphi^{*KSO}_{\ i}(\vec{r}) \, \varphi_i^{KSO}(\vec{r}) \tag{2.13}$$

$$f_{ij} = \left|\vec{D}_{ij}\right|^2 \frac{4\pi m_e v_{ij}}{3\hbar e^2} \tag{2.14}$$

$$\alpha^{SKSO}(\varepsilon) = \sum_{i\leq HO}\sum_{j\geq LU} f_{ij}\,\delta\left(\varepsilon - \Delta\varepsilon_{ij}\right) = \sum_{i<j} f_{ij}\delta\left(\hbar\omega - \hbar\omega_{ij}\right) \tag{2.15}$$

where v_{ij} is the transition frequency between $\varphi_i^{KSO}(\vec{r})$ and $\varphi_j^{KSO}(\vec{r})$, $\Delta\varepsilon_{ij}$ is the transition energy, and $\left\{\rho_{ii}^{eq} - \rho_{jj}^{eq}\right\}$ is the difference in occupations of $\varphi_i^{KSO}(\vec{r})$ and $\varphi_j^{KSO}(\vec{r})$, Note that states i are defined to be in the valence band and states j in the conduction band.

In the excited state, when the conduction band is occupied by a photo-excited electron and valence band has a photo-induced hole, the concept of population inversion can be applied. The rate of radiative emission can be found from the Einstein coefficient for spontaneous emission[42] A_{ij}

$$\mathrm{A_{ij}} = \frac{8\pi^2 \mathrm{v_{ij}^2 e^2}}{\varepsilon_0 \mathrm{m_e c^3}} \;\; \frac{\mathrm{g_i}}{\mathrm{g_j}} f_{ij} \tag{2.16}$$

where $\mathrm{g_i}$ and $\mathrm{g_j}$ represent the degeneracy of states $\varphi_i^{KSO}(\vec{r})$ and $\varphi_j^{KSO}(\vec{r})$.

2.4. Electron-Phonon Interactions

Photo-excited charge-carriers (electrons and holes) in semiconductor materials interact with the lattice vibrations and can exchange energy. Excess photo-excitation energies above the bandgap, $E_{excitation} - E_{gap}$ is usually transferred to the lattice by the emission of phonons where the electron and hole relax to the bandgap edges (LUMO and HOMO). From this state the electron-hole pair can either recombine radiatively, as luminescence, or non-radiatively. Here we describe the electron-phonon interactions that give rise to non-radiative transitions. The observable of most importance is the non-adiabatic coupling vector which describes the coupling of orthogonal electronic states due to thermal motion.

Rigorously, phonons are quantized particles and have nuclear wavepackets to describe their time evolution. Treating all nuclear degrees of freedom on a first-principles basis scales

exponentially, so it is impractical to implement for most atomic systems. For the work done in this dissertation nuclear degrees of freedom are treated as point particles and neglect the quantum features, such as tunneling. First I will describe the formalism for treating nuclear and electronic degrees of freedom on first principles basis. Then I will describe the quantum-classical methodology used for calculations used in this dissertation.

2.4.1. 2nd Quantization Formalism – Frohlich Hamiltonian

The coupling of electronic and nuclear degrees of freedom is generally described by the Frohlich Hamiltonian[43]. In eq (2.17)-(2.20) the Frohlich Hamiltonian is described in 2nd quantization formalism

$$H_{total} = H_e + H_{ph} + H_{e-ph} \tag{2.17}$$

H_e is the on-site electronic energy, H_{ph} is the phonon energy of a harmonic oscillator, and H_{e-ph} is the cross-term which described interaction between electronic and nuclear degrees of freedom.

$$H_e = \sum_{n,k,s} \zeta_{nks} c^{\dagger}_{nks} c_{nks} \tag{2.18}$$

In eq 2.18 n, k, s represent band, crystal momentum, and spin indices with $c^{\dagger}_{nks}$ and c_{nks} being the Fermionic annihilation and creation operators. ζ_{nks} is the on-site electronic matrix element.

$$H_{ph} = \sum_{q,\nu} \hbar\omega_{q\nu} \left(a^{\dagger}_{q\nu} a_{q\nu} + \frac{1}{2} \right) \tag{2.19}$$

In eq. 2.19 q and ν represent phonon momentum and mode index with $\hbar\omega_{q\nu}$ being the phonon mode energy. $a^{\dagger}_{q\nu}$ and $a_{q\nu}$are the Boson creation and annihilation operators. Note that for a spatially confined particle $< k >= 0$ and $< q >= 0$.

$$H_{e-ph} = \sum_{k,q,n,n',\nu,s} \gamma_{nn'}(q,k,\nu) \omega_{q\nu} c^{\dagger}_{n'ks} c_{n,k-q,s} a_{q\nu} + h.c. \tag{2.20}$$

Eq 2.20 describes the interaction of electronic degrees of freedom with nuclear degrees of freedom with $\gamma_{nn'}(q,k,\nu)$ being the matrix element. H_{e-ph} can be decomposed into two distinct interactions: a 'static' interaction when $n = n'$

$$H_{e-ph}^{static} = \sum_{n=n',\nu} \gamma_{nn} \omega_\nu c_n^\dagger c_n (a_\nu + a_\nu^\dagger) \tag{2.21a}$$

and a dynamic interaction $H_{e-ph}^{dynamic}$ when $n \neq n'$

$$H_{e-ph}^{dynamic} = \sum_{n\neq n',\nu} \gamma_{nn'} \omega_\nu c_n^\dagger c_{n'} (a_\nu + a_\nu^\dagger) \tag{2.21b}$$

H_{e-ph}^{static} corresponds to a change of nuclear coordinates along an adiabatic potential energy surface (PES). $H_{e-ph}^{dynamic}$ corresponds to changes in occupations of electronic and nuclear states allowing for dissipative dynamics. Analytic solutions of are available from the Feynman path integration approach[44] and Lee-Low-Pines transformations. In the previous approaches both electronic and nuclear degrees of freedom are treated quantum mechanically. Here we focus on using numerical simulations to describe the formation and dynamics of polarons using a quantum-classical method by treating nuclear degrees of freedom classically while treating electronic degrees of freedom quantum mechanically as described in the next sub-section.

2.4.2. Quantum-Classical Treatment: Non-Adiabatic Couplings

To make the excited-state calculations tractable a common, and justified, approach is to use a mixed-quantum classical approximation where the electrons are treated quantum mechanically and nuclei are treated classically. For inorganic semiconducting materials this is a valid approximation due to the large nuclei where quantum tunneling affects are negligible.

For our quantum classical treatment the electronic contributions H_e are treated quantum mechanically using DFT. Nuclear contributions H_{ph} are described within the classical path approximation (CPA) where nuclear wavefunctions are approximated as delta functions

$\phi_v(R_I) = \delta(R_I - \langle R_I \rangle)$ with $\langle R_I \rangle = \langle \phi_v | R_I | \phi_v \rangle$ being the expectation value of nuclear position where $|\phi_v\rangle$ are nuclear wavefunctions. Thus, phonon part of the Hamiltonian is represented in terms of positions and momenta of nuclei for potential and kinetic energies. The response of nuclear potential energy to changes in electronic configuration and electronic transitions facilitated by nuclear motion, as is standard in self-consistent DFT calculations.

To describe the equations of motion for the excited-state dynamics matrix elements $\gamma_{nn'}$ of the dynamic electron-phonon interaction $H_{e-ph}^{dynamic}$ are needed. These are obtained by computing NACs V_{ij}^{NAC} which describe the probability of transitions between two potential energy surfaces. Two common approaches are used to compute NACs[45]: (1) along normal mode (ζ_I) coordinates [39, 46] $V_{ij}^{NAC} = \left\langle \varphi_i^{KSO}(\vec{r}; R(t)) \middle| \frac{d}{d\zeta_I} \middle| \varphi_j^{KSO}(\vec{r}; R(t)) \right\rangle \frac{d\zeta_I}{dt}$ and (2) in an 'on-the-fly'[45] fashion as $V_{ij}^{NAC} = \left\langle \varphi_i^{KSO}(\vec{r}; R(t)) \middle| \frac{d}{dt} \middle| \varphi_j^{KSO}(\vec{r};\ R(t)) \right\rangle$. $R(t) = \{\vec{R}_I(t)\}$ represents displacement of ions *I* due to thermal motion with $\varphi_j^{KSO}(\vec{r};\ R(t))$ being an adiabatic state that depends parametrically on $R(t)$. For this thesis I opt to compute NACs 'on-the-fly'.

To compute NACs 'on-the-fly' we implement *ab Initio* molecular dynamics (AIMD) [47]. The total kinetic energy of the system is set equal to a thermostat, equation (2.22), as an initial condition. Once the system has equilibrized to a thermal temperature the positions of atomic nuclei are propagated by using Newton's equations of motion, equation (2.23). At each timestep the Kohn-Sham electronic density ρ is computed which provides the forces acting on the nuclei $\vec{F}_I(\hat{\rho})$. The eigen-energies of KSOs are recorded at each timestep to observe fluctuations in time, equation (2.24).

$$\sum_{I=1}^{N^{ion}} \frac{M_I}{2} \left(\frac{d\vec{R}_I}{dt}\Big|_{t=0}\right)^2 = \frac{3}{2} N^{ion} k_B T \tag{2.22}$$

$$\frac{d^2}{dt^2}\vec{R}_I = \vec{F}_I(\hat{\rho})/M_I \tag{2.23}$$

$$\varepsilon_{i,\sigma}(t) = \varepsilon_{i,\sigma}\left(\overrightarrow{R_I}(t)\right) \tag{2.24}$$

At each subsequent timestep the inner product of $\varphi_i^{KSO}\left(\vec{r},\{\vec{R}_I(t)\}\right)$ with $\varphi_j^{KSO}\left(\vec{r},\{\vec{R}_I(t+\Delta t)\}\right)$ is taken to compute the NAC[48-49]

$$\hat{V}_{ij}^{\mathrm{NAC}}(t) = -i\hbar\left\langle\varphi_i^{KSO}\left(\vec{r},\{\vec{R}_I(t)\}\right)\middle|\frac{\partial}{\partial t}\middle|\varphi_j^{KSO}\left(\vec{r},\{\vec{R}_I(t)\}\right)\right\rangle =$$

$$-\frac{i\hbar}{2\Delta t}\int d\vec{r}\left\{\varphi_i^{KSO}\left(\vec{r},\{\vec{R}_I(t)\}\right)^{*}\varphi_j^{KSO}\left(\vec{r},\{\vec{R}_I(t+\Delta t)\}\right)\right\}\cdot h.c. \tag{2.25}$$

where $\Delta t = 1\ fs$ represents the timestep in the MD trajectory. The NACs are then used to parameterize the equations of motion for an electronic system weakly coupled to a thermal bath. This is described in the next section.

2.5. Quantum Dynamics of Charge Carriers Coupled to Nuclear Degrees of Freedom

2.5.1. Density Matrix Equations of Motion

Popular mixed quantum-classical methods for modeling excited-state dynamics are mean-field Ehrenfest dynamics where the particles trajectory follow the occupation weighted average PES, surface hopping[50-52] where the particle hops between adiabatic PES in regions of strong NAC, and multiple spawning[53-54] where near regions of strong NAC nuclear states are 'spawned' to represent the splitting of the nuclear wavepacket.

Here the author uses a density matrix approach. Instead of directly propagating the wavefunction

$$i\hbar\frac{d}{dt}\,|\psi\rangle = \hat{H}\,|\psi\rangle \tag{2.26}$$

It is the density matrix which is propagated in time using the Liouville equation

$$\frac{d}{dt}\hat{\rho} = -\frac{i}{\hbar}[\widehat{H},\hat{\rho}] = \mathcal{L}\hat{\rho} \tag{2.27}$$

where $\hat{\rho} = |\psi\rangle\langle\psi|$ and $\mathcal{L}$ is commonly referred to as the Liouville superoperator. The above expressions describe the energy-conserving time evolution of quantum states.

2.5.2. Redfield Equations –Electron-Phonon Coupling

To describe the thermal relaxation of charge carriers requires additional terms for energy dissipation

$$\frac{d}{dt}\hat{\rho} = -\frac{i}{\hbar}[\widehat{H}, \hat{\rho}] + \left(\frac{d\rho}{dt}\right)_{diss} = (\mathcal{L} + \Re)\hat{\rho} \tag{2.28}$$

where $\left(\frac{d\rho}{dt}\right)_{diss} = \Re$ and $\Re$ is referred to as the Redfield superoperator. The rest of the section will describe how these dissipate terms and the observables which can be computed from the dynamics of the density matrix.

Assuming weak-coupling between electronic and nuclear degrees of freedom (ie $\hat{\rho}(\vec{r}, \vec{R}) = \hat{\rho}_{elec}(\vec{r}) * \hat{\rho}_{nuc}(\vec{R})$) the density matrix can be expanding using perturbation theory. The first non-vanishing term is to 2nd order perturbation with respect to the time-dependent interaction potential $V(t)$

$$\frac{d}{dt}\hat{\rho}(t) = \hat{\rho}^{(0)}(t \to \infty) - \frac{1}{\hbar^2}\int_0^t dt' \left[V(t), \left[V(t'), \hat{\rho}^{(0)}(t)\right]\right] \tag{2.29}$$

where $\hat{\rho}^{(0)}$ represents the 0th order density matrix. To obtain the above expression the Markoff approximation is used, which assumes that the evolution of the density matrix only depends on its current value $\hat{\rho}^{(0)}(t)$ and is uncorrelated with previous interactions with the bath during earlier interactions $\hat{\rho}^{(0)}(t')$. Rigorously, this implies that correlation functions of the potentials are described as $\langle V(t)\, V(t')\rangle = \delta(t - t')$. For practical calculations, it is assumed that the correlation function decays with a characteristic time τ_c such that $\langle V(t)\, V(t')\rangle = e^{-\frac{t}{t_c}}$. This approximation is valid when τ_c is much smaller than the timescale of the observables that are of

interest. In the context of this work, electronic dephasing occurs much faster (~1-10 fs) than hot-carrier cooling (~1-10 ps) and non-radiative recombination (1-10ns). As a final note about the above expression, in comparison to wavefunction time-dependent perturbation theory it is equivalent to 1st order time-dependent perturbation ie. Fermi's Golden Rule.

There are two approaches for propagating electronic degrees of freedom: explicitly solve for all electronic and nuclear degrees of freedom or trace over the density matrix with respect to the bath degrees of freedom. Tracing over the bath degrees of freedom turn the dependence of the bath into time-correlation functions of the electron-phonon interaction and the density matrix into a reduced-density matrix operator. In this approach the commutators in eq 2.29 turn into two-point correlation functions of the NACs.

The Fourier transform of the autocorrelation function, equation (2.30a-c), provides components of the Redfield tensor, equation (2.30d).

$$M_{ijkl}(\tau) = \frac{1}{T}\int_0^T V_{ij}^{NAC}(t+\tau)V_{kl}^{NAC}(t)dt \tag{2.30a}$$

$$\Gamma_{ijkl}^{+} = \frac{1}{T}\int_0^T M_{ijkl}(\tau)e^{-i\omega_{kl}\tau}d\tau \tag{2.30b}$$

$$\Gamma_{ijkl}^{-} = \frac{1}{T}\int_0^T M_{ijkl}(\tau)e^{-i\omega_{ij}\tau}d\tau \tag{2.30c}$$

$$R_{ijkl} = \Gamma_{ijkl}^{+} + \Gamma_{ijkl}^{-} + \delta_{lj}\sum_m \Gamma_{ijkl}^{+} - \delta_{ik}\sum_m \Gamma_{ijkl}^{-}, \tag{2.30d}$$

where Γ_{ijkl}^{+} and Γ_{ijkl}^{-} correspond to thermal excitations and relaxations, respectively. The Redfield tensor, eq 30d, controls dissipative dynamics of the density matrix.

$$\left(\frac{d\rho_{ij}}{dt}\right)_{diss} = \sum_{lm} R_{ijlm}\rho_{lm} \tag{2.31}$$

Equation 2.31 describes the dissipative dynamics within the secular approximation where the tensor can be decomposed into two main components: population relaxation and coherence relaxation. Population relaxation is represented by the diagonal elements of the tensor where

$R_{ii,jj}$ describes relaxation of occupations from state i to state j. Coherence relaxation is represented by off-diagonal elements where $R_{ij,ij}$ represents the dephasing between state i to state j.

For dynamics simulations done in this thesis two approximations are made. First, electronic coherences are neglected. This is valid as dephasing occurs on the ~10fs timescale and provides small contributions towards the ps and ns charge-carrier dynamics. Thus we only consider $R_{ii,jj}$ relaxation terms. Second, we employ an independent particle approximation where the full dynamics of the charge-carriers $\rho = \begin{pmatrix}\rho_v \\ \rho_c\end{pmatrix}$ for electron occupations in the conduction band ρ_c and hole occupations in the valence band ρ_v

$$\frac{\partial}{\partial t}\begin{pmatrix}\rho_v \\ \rho_c\end{pmatrix} = \begin{pmatrix}R_{vv} & R_{vc} \\ R_{cv} & R_{cc}\end{pmatrix}\begin{pmatrix}\rho_v \\ \rho_c\end{pmatrix} \tag{2.32}$$

are decoupled such that intraband valence-to-valence non-radiative transitions R_{vv} and conduction-to-conduction R_{cc} are computed while interband valence-to-conduction R_{vc} and conduction-to-valence R_{vc} transitions are neglected.

$$\frac{\partial}{\partial t}\begin{pmatrix}\rho_v \\ \rho_c\end{pmatrix} = \begin{pmatrix}R_{vv} & 0 \\ 0 & R_{cc}\end{pmatrix}\begin{pmatrix}\rho_v \\ \rho_c\end{pmatrix} \tag{2.33}$$

This approximation is based on the large timescale differences between carrier-cooling (ps) and non-radiative recombination (ns) relaxation events. In a later chapter there will be methodology development towards incorporating non-radiative relaxation interband relaxation into the dynamics through a dampening factor.

2.5.3. Excited-State Trajectory Observables

The final portion of this section will be describing time-resolved non-radiative and radiative observables along the excited-state trajectory. The population density in the energy domain is described as

$$n(\varepsilon, t) = \sum_i \rho_{ii}(t)\delta(\varepsilon - \varepsilon_i) \tag{2.34a}$$

where ε_i are eigen-energies of the KSO equation. In the excited-state the non-equilibrium density is

$$\Delta n(\varepsilon, t) = n(\varepsilon, t) - n^{eq}(\varepsilon, t) \tag{2.34b}$$

where $n^{eq}(\varepsilon, t)$ is the ground-state equilibrium density. $\Delta n(\varepsilon, t) > 0$ represents an increase in electron density, $\Delta n(\varepsilon, t) < 0$ indicates an increase in hole density, and $\Delta n(\varepsilon, t) = 0$ represents an unchanged population. The electron, equation 2.35a, and hole, equation 2.35b, energy expectation value along the trajectory is described as

$$\langle \Delta\varepsilon_e \rangle(t) = \sum_{i \geq LU} \rho_{ii}(t)\varepsilon_i(t) \tag{2.35a}$$

$$\langle \Delta\varepsilon_h \rangle(t) = \sum_{i \leq HO} \rho_{ii}(t)\varepsilon_i(t) \tag{2.35b}$$

where the electron state is summed over the occupations in the conduction band and the hole state is summed over the valence band. The charge-carriers energy expectation value is normalized to a dimensionless energy

$$\langle E_{e/h} \rangle(t) = \frac{\langle \Delta\varepsilon_{e/h} \rangle(t) - \langle \Delta\varepsilon_{e/h} \rangle(\infty)}{\langle \Delta\varepsilon_{e/h} \rangle(0) - \langle \Delta\varepsilon_{e/h} \rangle(\infty)} \tag{2.36a}$$

Assuming a single exponential decay, the rate of relaxation for a ‘hot’ electron to the conduction band edge LUMO state is

$$k_{e/h} = \left\{\tau^{e/h}\right\}^{-1} = \left\{\int_0^\infty \langle E_{e/h} \rangle(t) dt\right\}^{-1} \tag{2.36b}$$

Equations 2.30(a)-(d) and 2.31 describe the non-radiative decay of charge-carriers along the excited-state trajectory by emitting a phonon. A competing relaxation pathway for charge-carriers is to emit a photon. The time-resolved emission along the excited-state trajectory is described as

$$E(\hbar\omega, t) = \sum_{j>i} f_{ij}\delta\left(\hbar\omega - \hbar\omega_{ij}\right)\left\{\rho_{jj}(t) - \rho_{ii}(t)\right\} \tag{2.37a}$$

where f_{ij} is the oscillator strength between state i and j, $\delta(\hbar\omega - \hbar\omega_{ij})$ gives the energy of transition, and the $\{\rho_{jj}(t) - \rho_{ii}(t)\}$ terms describes population inversion needed for photoluminescence to occur. This term is at a maximum when the excited-state occupation of state j in the conduction band is fully occupied $\rho_{jj}(t) = 1$ and the state in the valence band is fully occupied by a hole $\rho_{ii}(t) = 0$. To generate a PL spectrum the time-resolved emission, eq 37a, is summed over the length of the trajectory

$$E^{tot}(\hbar\omega) = \frac{1}{T}\int_0^T E(\hbar\omega, t)dt \tag{2.37b}$$

where T is the duration of the trajectory. Typically the value of T is chosen to be equal to the non radiative recombination lifetime $\tau_{nr} = \frac{1}{k_{nr}}$.

To compute a PLQY from the excited-state dynamics we approximate the non-radiative and radiative relaxation rates as the matrix elements of the and the Redfield tensor, eq 38(a), and Einstein coefficient for spontaneous recombination, eq 38(b) which corresponds to the lowest energy transitions across the bandgap

$$k_{nr} \approx R_{HOMO-LUMO} \tag{2.38a}$$

$$\mathrm{k_r} \approx \mathrm{A_{HOMO-LUMO}} \tag{2.38b}$$

PLQY is defined as the ratio of the radiative recombination rate to the sum of radiate and non-radiative recombination, eq 2.38c. This neglects other relaxation pathways, such as energy transfer events which we do not typically consider for the systems investigated.

$$PLQY = \frac{k_r}{k_r + k_{nr}} \tag{2.38c}$$

3. LEAD HALIDE PEROVSKITE NANOCRYSTALS: SURFACE CHEMISTRY, PARTICLE-IN-A-BOX PHOTOPHYSICS, AND NON-RADIATIVE DYNAMICS

3.1. Introduction

The main material of interest for this dissertation is the lead halide perovskite nanocrystal. This chapter is intended to provide two aspects of background information on this material: the materials chemistry, in particular the surface chemistry of the nanocrystal, and their photo-physics in terms of simple particle-in-a box picture. The background information on the materials and surface chemistry will be used to rationalize the construction of the atomistic models used in the this dissertation. The photo-physics background will be used to compare the particle-in-a-box models to atomistic DFT calculations, such as electronic density of states and absorption spectra. The final section will describe the non-radiative dynamics of a two-level systems in Redfield formalism. This chapter will serve as a precursor to the rest of the dissertation which will discuss the coupling of electronic and nuclear degrees of freedom to describe the kinetics of photo-induced processes.

3.2. Chemistry of Lead Halide Perovskites

Perovskites are a general form of crystal structure ABX_3 where A and B species are cations and X species are anions. The perovskite crystal structures are generally cubic, or pseudocubic/octahedral, with the $B-X$ species forming a chemically bonding network in octahedral coordination and the A cation fills the space created by the $B-X$ bonding network. The crystal stability of a specific perovskite structure is generally characterized by the Goldschmidt tolerance factor[55] t

$$t = \frac{r_A + r_X}{\sqrt{2}(r_B + r_X)} \tag{3.1}$$

where r_i is the ionic radius of the cation species. The tolerance factor describes how efficiently the A cation fits in the the $B-X$ cubic bonding network. For $t > 1$ it means the A cation is too large, or the B cation is too small, and for $t < 1$ the A cation is smaller than the space created by the $B-X$ bonding network. The greater the deviation from $t = 1$ the greater the lattice distortion will be and more likely to have a phase transition to occur.

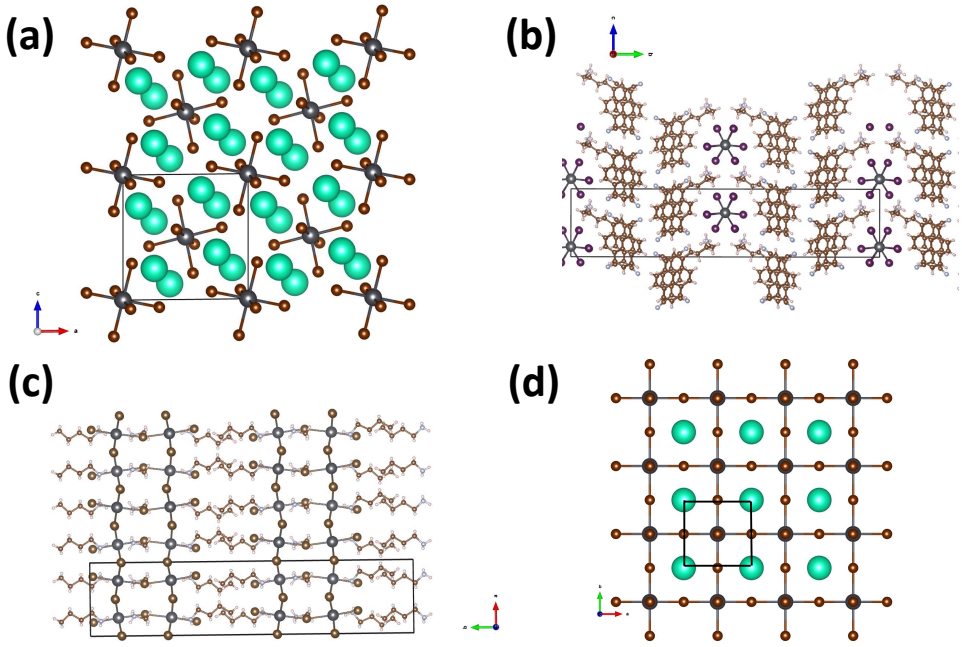

Figure 3.1: The **(a)** 0D, **(b)** 1D, **(c)** 2D, and **(d)** 3D polymorphs of lead halide perovskites which differ based on the connectivity of the $PbBr_6$ octahedra. In **(a)** the $PbBr_6$ octahedra are separated by a spherical layer of Cs^+ and do not share any connections. In **(b)** the octahedra share corners in the direction in/out of the page with the other two directions spaced by an organic molecule. In **(c)** the octahedra share two corners forming 2D sheets which are spaced by organic molecules. In **(d)** all octahedral share corners forming a continuous 3D crystalline network.

Lead halide perovskites are combinations where $B = Pb^{2+}$ and $X = \{Cl^-, Br^-, I^-\}$. Typical A cations are $A = \{Cs^+, CH_3NH_3\}$. Aside from chemical compositions, lead halide perovskites have a wide variety of physical compositions in the form of polymorphs, which are 0-D, 1-D, 2-D, 3-D connectivity's of the bulk lattice[56] shown in **Figure 3.1**, and nanostructured phases, such as nanocrystals[29], nanowires[57], and Ruddlesden-Popper [26] films. Just considering

the chemical compositions listed above that gives a 96 possible structures to investigate. For this dissertation the chemical structure of interest will be 3-D polymorphs of fully-inorganic $Cs^+Pb^{2+}X_3^-$ nanocrystals where $X^- = (Cl^-, Br^-, I^-)$.

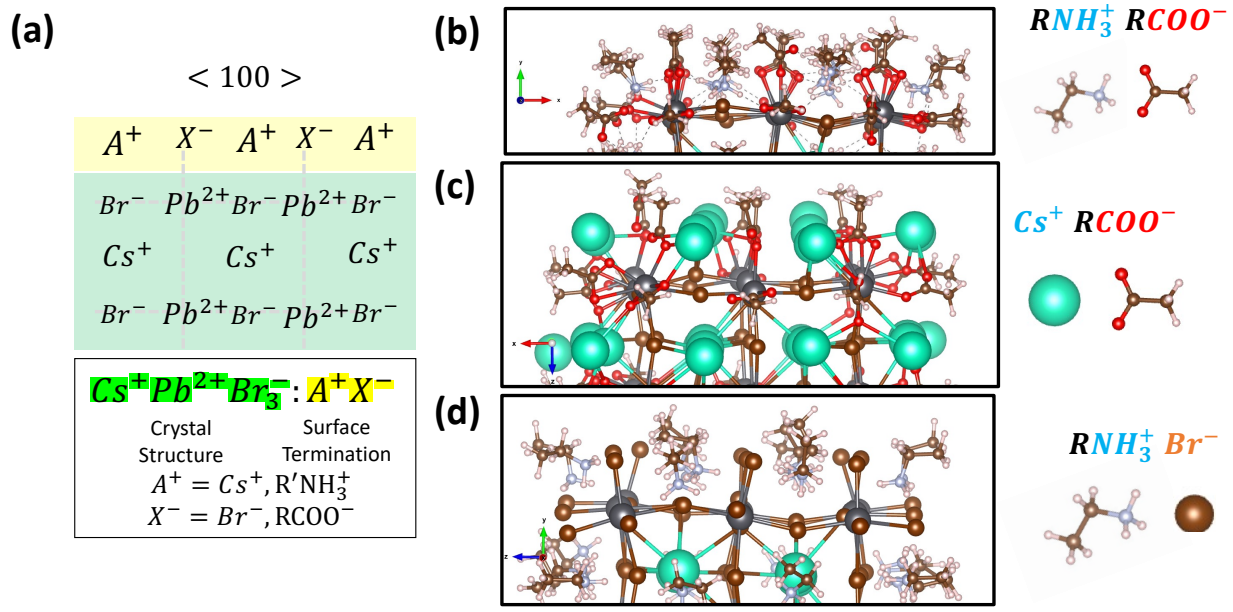

Figure 3.2: Illustration of the surface chemistry used to passivate a Pb-Br terminated surface. **(a)** Scheme of the <100> surface with a Pb-Br terminated surface exposed. Due to the tertiary chemical nature of the bulk lead halide perovskites leads to a binary surface termination. The most likely combinations are cation/anion pairs to preserve charge neutrality. Three likely surface terminations are **(b)** alkylammonium-alkylcarboxylate, **(c)** cesium alkylcarboxylate, and **(d)** alkylammonium bromide.

Experimentally, LHP NCs are generally synthesized as colloidal suspensions using thermal hot-injection methods where Pb-halide precursor is dissolved in a mixture of oleic acid (carboxylic acid functional groups) and oleylamine[29]. For the oleic acid and oleylamine to dissolve the PbX_2 precursor it is highly likely that the acid deprotonates with the oleylamine converting into oleylammonium to form Pb(oleyloleate)$_2$ and oleylammonium-bromide. Once the Pb-halide precursor is fully-dissolved Cs-oleate is injected at a specific temperature into the reaction vessel and $Cs^+Pb^{2+}X_3^-$ nanocrystals form within seconds. For the NCs to remain as a colloidal suspension (in organic solvents) requires that the $Cs^+Pb^{2+}X_3^-$ NC core is passivated by either Cs-oleate, oleylammonium bromide, or oleylammonium oleate, as illustrated in **Figure 2**.

In the next section I will discuss building an atomistic model based on using oleylammonium-oleate as surface passivation ligands.

3.3. Atomistic Model Construction

From the bulk $CsPbBr_3$ crystal structure a 2x2x2 unit cells carved out giving a Pb/Br terminated surfaces providing a composition of $Cs_8Pb_{27}Br_{54}$. Thus the surface is composed of Pb-Br terminated surface. To passivate terminal Pb^{2+} atoms we use methylcarboxylate and ethylammonium cations or coordinate to surface Br . Overall, this gives a structure of $Cs_8Pb_{27}Br_{54}$ passivated with 54 (48) carboxylate/ethylammoniuym anions, as illustrated in **Figure 3.3**. Overall this structure gives an NC with edge length of 2nm. This is typically smaller than the sizes observed in experiment (3-15nm), but serves as a. good approximation. Including passivation ligands for a larger NC core would push the practical computational limits.

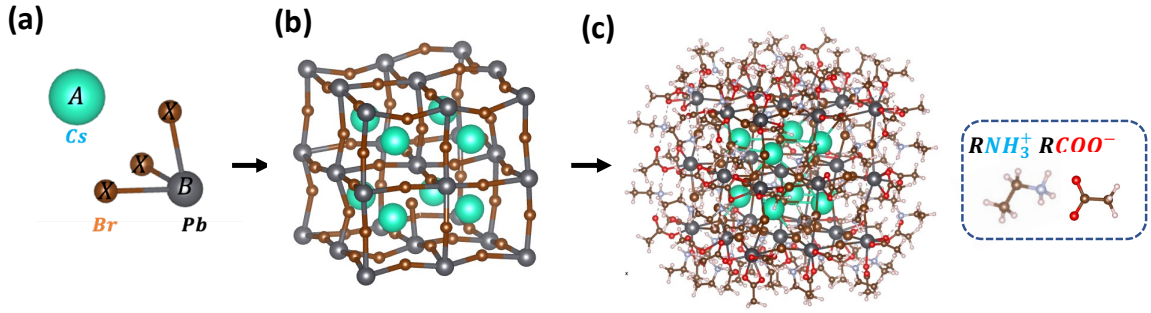

Figure 3.3: (a) Unit cell of $CsPbBr_3$, **(b)** 2x2x2 composition of $CsPbBr_3$ with Pb-Br terminated surfaces, **(c)** 2x2x2 composition with the Pb-Br terminated surface passivated by alkyl-carboxylate $RCOO^-$ and alkylammonium RNH_3^+.

3.4. Particle-In-A-Box

Here I will review some simple physical models to anticipate what to expect from the *ab Initio* based electronic structures calculation for the perovskite nanocrystal. One of the classic introductory problems for quantum mechanics is the 'particle-in-a-box' where by applying infinite potential barriers $V(x, y, z)$ creating confinement

$$H(x,y,z) = \frac{\hat{p}_x^2+\hat{p}_y^2+\hat{p}_z^2}{2m} + V(x,y,z) \tag{3.2}$$

$$V(x,y,z) = \begin{cases} \infty;\ x,y,z < 0 \\ 0;\ 0 < x,y,z < L \\ \infty;\ x,y,z > L \end{cases} \tag{3.3}$$

the solutions are standing waves along the independent x,y, and z spatial coordination which have discrete, quantized modes. Consequently the energy spectrum is quantized

$$\phi_i^{e/h}(x,y,z) = \frac{\pi}{8L_xL_yL_z}\sin\left(\frac{n_x\pi}{L_x}x\right)\sin\left(\frac{n_y\pi}{L_y}y\right)\sin\left(\frac{n_z\pi}{L_z}z\right), n_i = 1,2,3,\ldots \tag{3.4}$$

$$E_{e/h}(n_x,n_y,n_z) = \frac{\pi^2\hbar^2}{2m_{e/h}^* V^2}(n_x^2+n_y^2+n_z^2) \tag{3.5}$$

where L_i are the length dimensions of the box, n_i are the quantum numbers, $m_{e/h}^*$ is the effective mass of the electron or hole, and V is the volume of the box.

Figure 3.4 illustrates the electronic DOS

$$n(E) = \sum_i \delta\,(E - E_i(n_x,n_y,n_z)) \tag{3.6}$$

where E_i represents the eigen-energies for the particle-in-a-box for states in the VB (red,solid) and CB (unfilled). The narrow peaks represent the individual bands and the overall distribution is found by approximating the δ function as a gaussian with broadening parameter 10 meV.The insets display the envelope function of the wavefunction inside the barrier corresponding the quantum numbers $n_x, n_y,$ and n_z. The lowest energy state $E_{e/h}(1,1,1)$ corresponds to a distribution of charge density that is spherically symmetric. In the literature these states can be described as $'s'$ bands. The next lowest set of energy states correspond to envelope functions which show a single nodal feature giving the charge-distribution a dumb-bell shape. For $L_x = L_y = L_z$ these three states are exactly degenerate in energy, but for visualization in **Figure 3.4** the confinement along each three spatial dimensions are slightly different to show each peak initially. In the literature these bands can be described as $'p'$ bands. Also note that the conduction

band has lower density of states than the valence band. This is due to the electron having a larger effective mass than the hole.

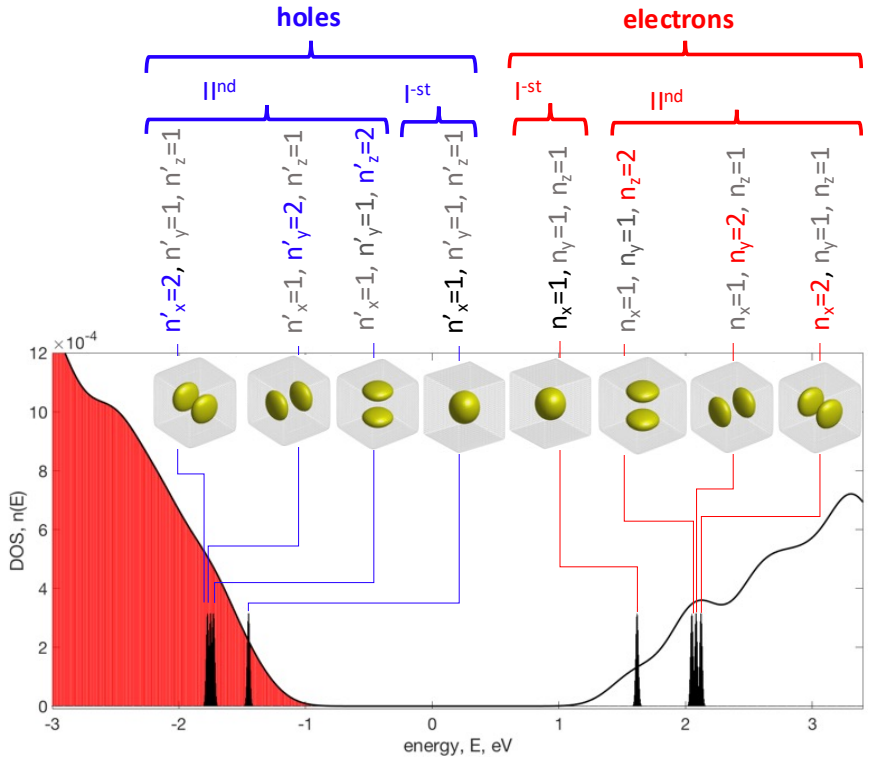

Figure 3.4: Density of states for the particle in a box model. The insets show the envelope function for selected states in the conduction and valence band. The spherically distributed functions can be described as 's' bands and the functions which show nodal features can be described as 'p' bands.

From the 'particle-in-a-box' electronic structure it is possible to gain insight into what the optical absorption spectra should look like. In **Figure 3.5** is illustrated the transition energy DOS (EDOS)

$$n(\Delta E) = \sum_{n_z,n_y,n_z} \delta(E_{gap} - E_h(n_x, n_y, n_z) - E_e(n_x, n_y, n_z)) = \sum_{n_z,n_y,n_z} \delta(E_{gap} - \Delta E) \quad (3.7)$$

where ΔE represents the energy difference between the electron $E_e(n_x, n_y, n_z)$ and hole state $E_h(n_x, n_y, n_z)$ and n_i represent the quantum numbers for the particle. This is equivalent to treating each possible optical transitions with equal statistical weight instead of weighting each transition by how likely it is to occur (ie oscillator strength).

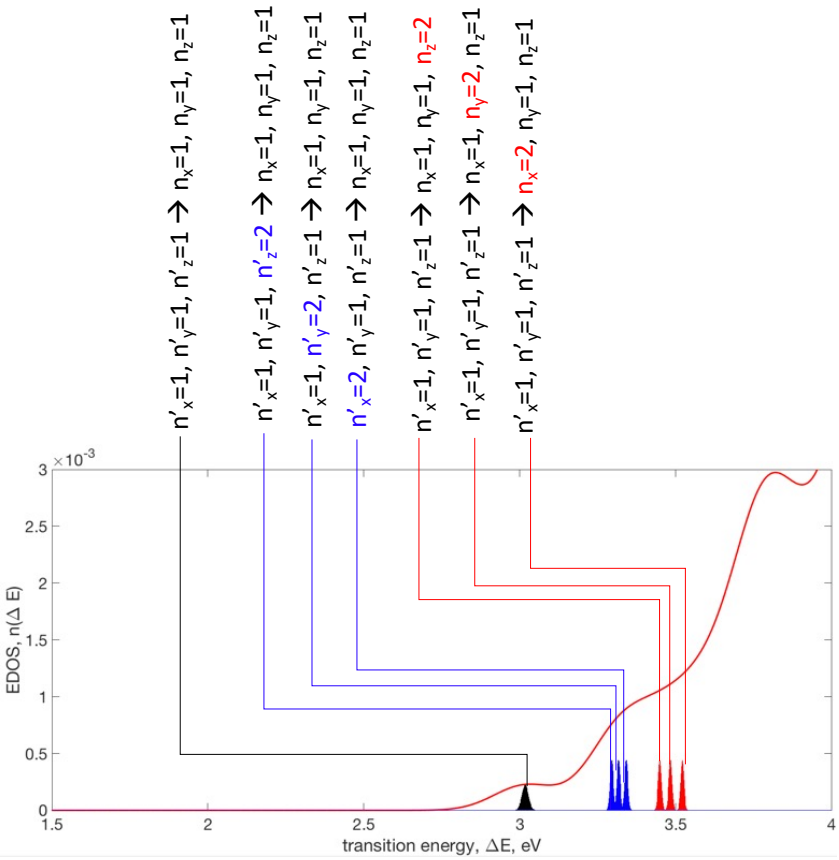

Figure 3.5: EDOS corresponding to the DOS in Figure 3.4.

In **Figure 3.5** the seven lowest transition energies, approximating optical excitation, are shown. The lowest energy transition corresponds to an $s_h \rightarrow s_e$ (black) type of transition. The next six highest energy transitions are of $p_h \rightarrow s_e$ (blue) and $s_h \rightarrow p_e$(red) type transitions. The reason for the asymmetry in the energetic spacing for $p_h \rightarrow s_e$ and $s_h \rightarrow p_e$ is due to the differences in effective mass for the electron and hole $m^*_{e/h}$. If $m^*_e = m^*_h$ the transitions would be

degenerate. Note that $p_h \rightarrow s_e$ and $s_h \rightarrow p_e$ transitions are typically expected to be optically dark while $s_h \rightarrow s_e$ transitions are expected to be bright due to symmetry arguments.

Here I will note that in real spatially confined systems, such as a nanocrystal, a photo-excited electron and hole will experience Coulombic attraction to one another creating an exciton. The strength of that interaction will depend on the degree of spatial confinement[58]: weak where $r_{NC} > r_{bohr}$, intermediate where $r_{NC} \approx r_{bohr}$, and strong where $r_{NC} < r_{bohr}$. The prototypical model for describing the Coulombic interaction is the effective mass approximation (EMA) which deals with the strong regime of confinement. EMA provides an additional term to the uncorrelated particle energies

$$E_{exciton} = E_g + \left(E_e(n_x, n_y, n_z) - E_h(n_x, n_y, n_z)\right) - \frac{1.8e^2}{\epsilon L} \tag{3.8}$$

where e is the fundamental charge, ϵ is the materials dielectric constant, and L is the spatial confinement distance. The prefix is found from perturbative calculations[59]. The main consequence of including the Coulomb interaction is due to attractive forces the energy of excitation decreases relative to the uncorrelated electron and hole.

The particle-in-a-box model provides good intuition for understanding confinement effects in nanocrystals, but for doing practical modeling requires including the role of atomic potentials from lattice sites within the nanocrystal. This provides wavefunctions which are composed of slowly varying envelope functions along with quickly varying atomic potentials. This will be expanded upon in the next section.

3.5. *ab Initio* Ground-State Electronic Structure and Optical Spectra

The particle-in-a-box formulation gives a good overview of how to understand part of the solution for the electronic structure of a nanocrystal. For a real nanocrystal the potential energy

will also contain contributions from the atom centered potentials along with the potential energy from the boundaries.

For the case of an infinite bulk crystal the general solution will be of the Bloch functions

$$|\varphi_{i\,\vec{k}}(\vec{r})\rangle = e^{i\vec{k}\cdot\vec{r}}\,|u_i(\vec{r})\rangle \tag{3.9}$$

$$|u_i(\vec{r})\rangle = \left|u_i\left(\vec{r} + n\cdot\vec{R}\right)\right\rangle \tag{3.10}$$

where $\vec{k}$ is crystal momentum, i is the band index, n is an integer, $\vec{R}$ is a lattice vector, and $|u_i(\vec{r})\rangle$ is the periodic lattice potential contributed by atom centered sites. $|u_i(\vec{r})\rangle$ obeys periodicity of the lattice and accumulates phase $e^{i\vec{k}\cdot\vec{r}}$ due to translation.

For the case of a nanocrystal the infinite periodicity of the lattice is replaced with boundary conditions. Once consequence of this is that the plane wave $e^{i\vec{k}\cdot\vec{r}}$ will transform into standing waves which represent the trigonometric envelope functions

$$|\varphi_i\ (\vec{r})\rangle = |\phi_{j'n'}(r)\,\rangle\,|u_{j'}(r)\rangle \tag{3.11}$$

where $|\phi_{j'n'}(r)\,\rangle$ is the slowly varying envelope function and $|u_{j'}(r)\rangle$ are the atom-centered sites with j' representing band indices and n'representing the quantum number of the envelop function. These envelope functions are analogous to the particle-in-a-box wavefunctions described in the previous section.

In **Figure 3.6(a)-(c)** we show **(a)** DOS and **(b)** absorption spectra compared to the EDOS computed from DFT for the geometry optimized perovskite nanocrystal model, shown in **Figure 3.3(c).** For DFT calculations we use a spin-restricted basis in the DFT formalism described in Chapter 2 section 2.2. For **(a)** the DOS we can see that the valence band has resolvable peaks for states near the band edge while for the conduction band the states are less defined. In **(b)** the DFT computed optical absorption spectrum is compared to the EDOS spectrum. It is observed

that the lower energy optical transitions, designated with the **a** and **b** labels, have higher 0.5-1 order of magnitude larger intensity compared to the EDOS spectrum. This indicates that these transitions have a higher statistical weight (ie oscillator strength) than the optical transitions at higher transition energies, labeled with **c**. Note that feature **a** is the $s_h \rightarrow s_e$ optical transition.

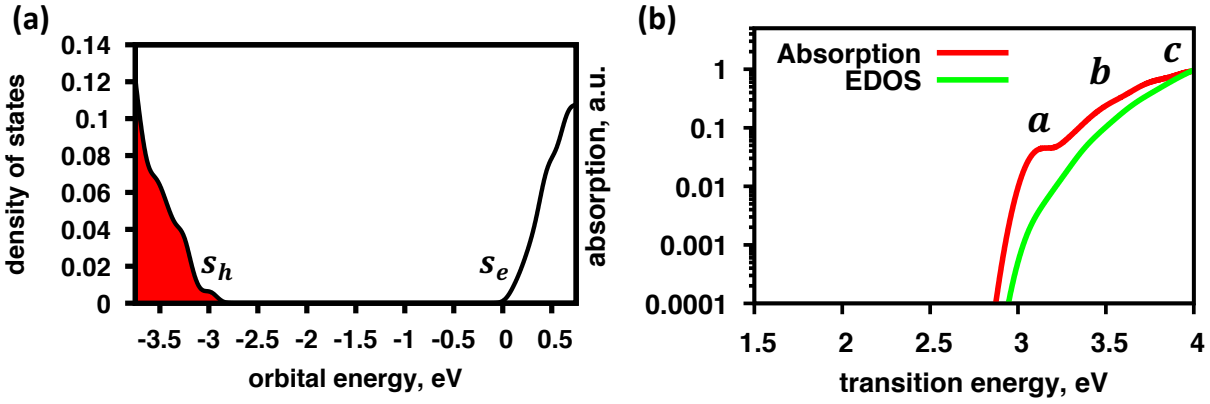

Figure 3.6: (a) Density of states and (b) optical absorption spectrum (red, solid) computed from DFT compared to the energy density of states (EDOS) for the CsPbBr3 nanocrystal atomistic model shown in **Figure 3.3(c).**

In **Figure 3.7(a)-(b)** we show the **(a)** $\boldsymbol{s_h}$ (HOMO) and **(b)** $\boldsymbol{s_e}$ (LUMO) KSOs for the perovskite nanocrystal model. The plots represent the charge density projected onto the x-axis as

$$\rho_{s_x}(z) = \int dy \int dx \, \rho_{s_x}(x, y, z) \tag{3.12}$$

where ρ_{s_x} represents the charge density of either the $\boldsymbol{s_h}$ or $\boldsymbol{s_e}$ band. For **(b)** we can see that the distribution of $\boldsymbol{s_h}$ charge density within the nanocrystal is very symmetric with maximum density in the middle of the crystal and decays to zero at the boundary. For **(c)** we can see that $\boldsymbol{s_e}$ charge distribution is slightly skewed to one direction, but overall is fairly symmetric. Deviations from perfect symmetry is attributed to the fact that the surfaces produce distortions which break ideal crystal symmetry. From this analysis it can be seen why the lowest energy $s_h \rightarrow s_e$ optical

transition has such a large oscillator strength, feature **a** in **Figure 6(b)**, since these bands have large spatial overlap within the nanocrystal.

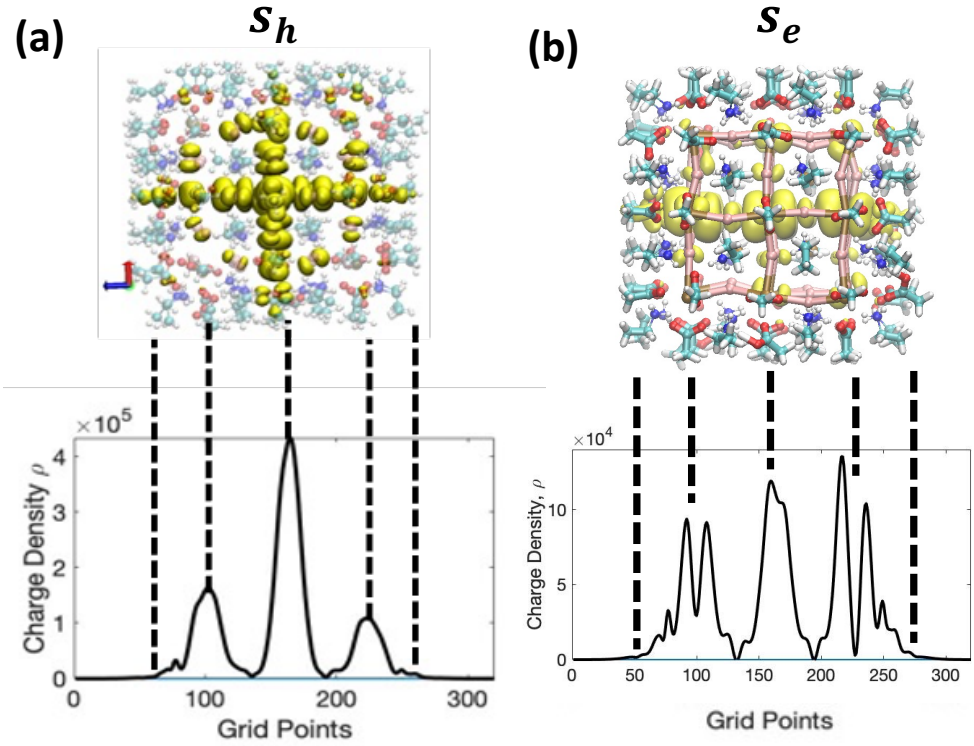

Figure 3.7: Illustration of (a) s_h charge density and (b) s_e charge density projected onto the z-axis.

3.6. Non-Radiative Carrier Dynamics for a 2-Level System – Redfield Dynamics

There are two primary non-radiative relaxation pathways that charge-carriers follow after photo-excitation: carrier-cooling (intraband) and recombination (interband). Carrier-cooling is facilitated by coupling of low energy phonon modes to the charge-carriers until they reach their lowest excited-state. From the lowest energy excited-state the charge-carrier will recombine to the ground-state. In typical situations, carrier-cooling occurs on the ~ps timescale while recombination occurs on the ~ns timescale. Here I will show the non-radiative dynamics for a two-level system coupled to a weak (perturbative) thermal bath. Parameters will be chosen to reflect two scenarios: Carrier-cooling for the intraband $p_{e/h} \rightarrow s_{e/h}$ transition and interband $s_e \rightarrow s_h$ non-radiative recombination**.**

The density matrix for electronic degrees of freedom have two components: diagonal matrix elements ρ_{00} and ρ_{11} which represent occupations and off-diagonal elements ρ_{01} and ρ_{10}which represent coherences. In Liouville space, the density matrix is described as a vector

$$\rho(t) = \begin{pmatrix} \rho_{00} \\ \rho_{01} \\ \rho_{10} \\ \rho_{11} \end{pmatrix} \tag{3.13}$$

The time evolution of the density matrix are determined by two terms: the Liouville and Redfield superoperators $\mathcal{L}$ and $\mathfrak{R}$.

$$\frac{d}{dt}\rho(t) = (\mathcal{L} + \mathfrak{R})\rho(t) \tag{3.14}$$

The Liouville operator describes coherent time evolution and the Redfield operator describes relaxation and dissipation. For the Liouville operator

$$\mathcal{L} = \frac{\mathrm{i}}{\hbar}\begin{pmatrix} 0 & 0 & 0 & 0 \\ 0 & (\epsilon_1 - \epsilon_0) + \Gamma & 0 & 0 \\ 0 & 0 & -(\epsilon_1 - \epsilon_0) + \Gamma & 0 \\ 0 & 0 & 0 & 0 \end{pmatrix} \tag{3.15}$$

the diagonal elements are stationary and the propagation of off-diagonal elements are determined by two factors: the energy difference between the electronic eigenstates $\epsilon_1 - \epsilon_0$ and the dephasing rate Γ . The dephasing rate describes the loss of coherence between the electronic eigenstates.

For the Redfield operator the time evolution of the density matrix is determined by the coupling of the bath degrees of freedom to the electronic states. The bath can be approximated as an ensemble of harmonic oscillators. For simplicity, I will consider coupling to only a single harmonic oscillator mode

$$\mathfrak{R} = \begin{pmatrix} -\mathrm{V}n & 0 & 0 & \mathrm{V}(n+1) \\ 0 & \mathrm{V}(2\mathrm{n}+1) & 0 & 0 \\ 0 & 0 & \mathrm{V}(2\mathrm{n}+1) & 0 \\ \mathrm{V}n & 0 & 0 & -\mathrm{V}(n+1) \end{pmatrix} \tag{3.16}$$

where $n = (e^{\frac{\hbar\omega}{kT}} - 1)^{-1}$ is the expectation value of normal mode occupation with ω being the normal mode frequency and V being the non-adiabatic coupling strength between the electronic and nuclear degrees of freedom. Note that the terms describing the thermal dynamics of occupations obey detailed balance

$$\frac{\Re_{00\to 11}}{\Re_{11\to 00}} = \frac{n}{n+1} = e^{\frac{-\Delta E}{kT}} \tag{3.17}$$

where $\Delta E = \epsilon_1 - \epsilon_0$. This means that the process of thermal relaxation is a Boltzmann factor more probable to occur than a thermal excitation.

First consider the dynamics of relaxation for the carrier-cooling $\boldsymbol{p_{e/h}} \to \boldsymbol{s_{e/h}}$ transition. The $\boldsymbol{p_{e/h}}$ band will represent the excited-state ρ_{11} and $\boldsymbol{s_{e/h}}$ will represent the ground-state ρ_{00}. The energetic spacing between these states can range from room-temperature $kT \approx 25\ meV$ to hundreds of meV. To compare the difference in carrier-cooling relaxation dynamics I will test when there is a resonance $\frac{\Delta E}{kT} = 1$ and when the electronic gap is an order of magnitude larger than thermal energy $\frac{\Delta E}{kT} = 10$. For the non-adiabatic coupling term I will use the fact that

$$\mathrm{V} = \frac{\left\langle \psi_i \left| \frac{\partial H}{\partial R} \right| \psi_j \right\rangle}{\epsilon_i - \epsilon_j} \tag{3.18}$$

where ψ_i and ψ_j are eigenstates, ϵ_i and ϵ_j being eigen-energies, and $\frac{\partial H}{\partial R}$ represents the change in energy with change in nuclear coordinates. For these numerical examples I will assume that $\left\langle \psi_i \left| \frac{\partial H}{\partial R} \right| \psi_j \right\rangle \approx kT$ so that $\mathrm{V} = \frac{\mathrm{kT}}{\Delta E}$.

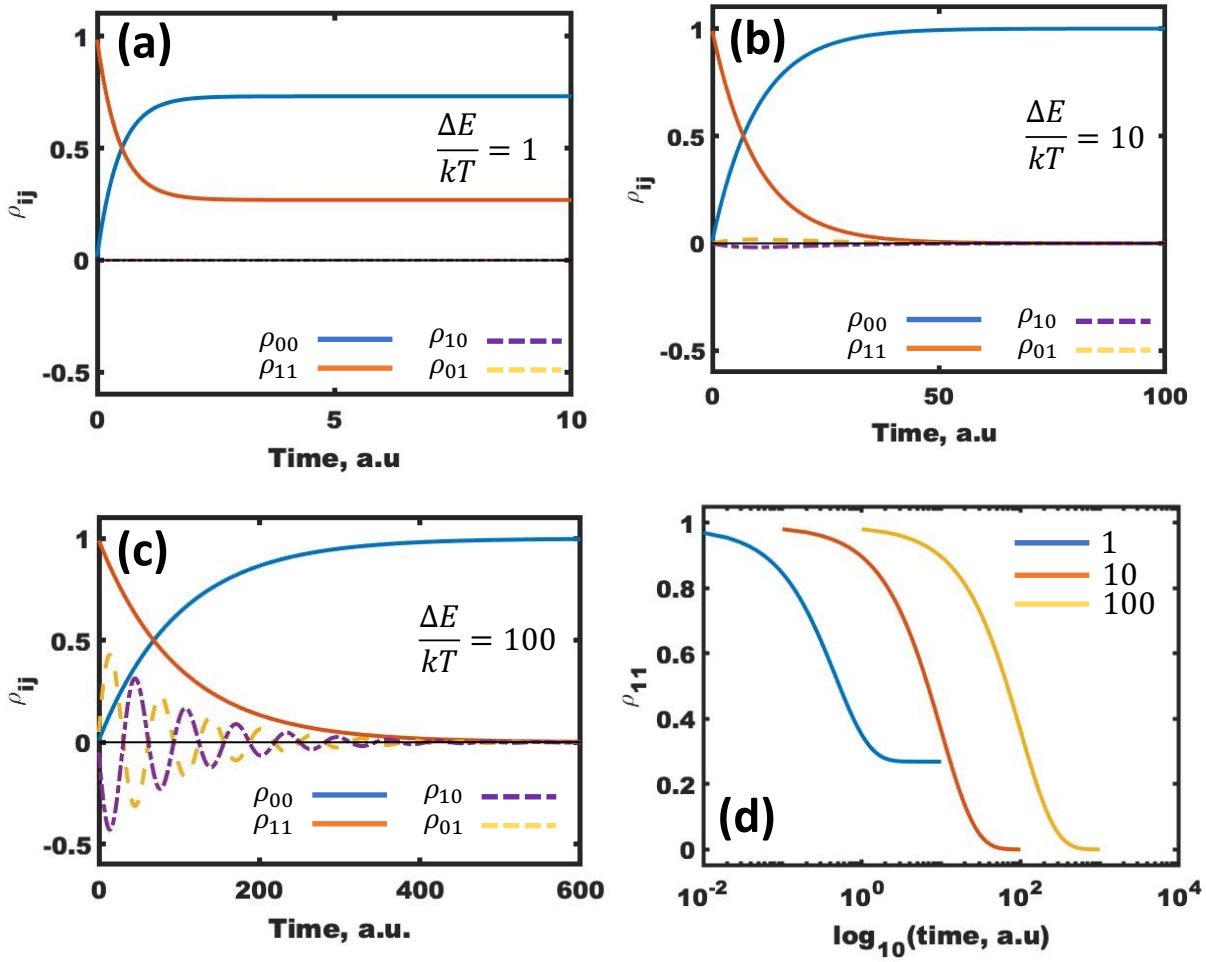

Figure 3.8: Comparison of non-radiative relaxation for (a)-(b) intraband $\boldsymbol{p_{e/h} \rightarrow s_{e/h}}$ carrier cooling transitions and (c) interband $\boldsymbol{s_e \rightarrow s_h}$ recombination (d) Comparing the relaxation lifetimes for (a)-(c) in log scale as a function of the ratio of energy gap ΔE between eigenstates and thermal energy kT.

Figure 3.8(a)-(b) compares the hot-carrier cooling relaxation when **(a)** there is a resonance $\frac{\Delta E}{kT} = 1$ and **(b)** when the electronic gap is an order of magnitude larger than thermal

energy $\frac{\Delta E}{kT} = 10$. There are two points of comparison. First, in **(a)** the excited-state occupation $\boldsymbol{p_{e/h}}$ does not fully decay to the ground-state $\boldsymbol{s_{e/h}}$ while in **(b)** the excited-state occupations fully decay. This is due to the energy differences between states in **(a)** being comparable to thermal energy so that thermal excitations are non-negligible giving a detailed balance between the two electronic states. Secondly, the lifetime for **(b)** is much longer than **(a)** due to the reduced non-adiabatic coupling when electronic states have large energy differences.

Next consider the dynamics of relaxation for non-radiative recombination $\boldsymbol{s_e} \rightarrow \boldsymbol{s_h}$ transition. The $\boldsymbol{s_e}$ band will represent the excited-state ρ_{11} and $\boldsymbol{s_h}$ will represent the ground-state ρ_{00}. The energetic spacing between these bands is approximately the bandgap energy which for semiconductors range from 1-3 eV which is 25-100 times larger than thermal energy at room temperature. For this situation $\frac{\Delta E}{kT} = 100$ is plotted in **Figure 3.8(c)**. Again it is observed that with an increased energy spacing between the two electronic states the non-radiative lifetime dramatically increases. Another interesting observation is that the coherences, off-diagonal elements of the density matrix, have much longer lifetimes as well compared to the carrier-cooling transitions in **Figure 3.8(a)-(b)**. **Figure 3.8(d)** compares the non-radiative decay of occupations in the excited-state from **Figure 3.8(a)-(c)** where it is observed that with order of magnitude increases in energy spacing there is an order of magnitude increase in the non-radiative lifetime.

3.7. Conclusions

Overall, this chapter serves three purposes: (1) introduction to the chemical composition and physical structure of lead halide perovskites with an emphasis on the NC nanostructure and its surface chemistry, (2) using the 'particle-in-a-box' model to rationalize the DFT based calculations of the NC atomistic model, and **(3)** exploring non-radiative relaxation for a two-

level system using Redfield theory. The main observations from this exploration are that the following: (i) that the lowest optical transition energy is very bright, relative to the other possible transitions, due to the confinement of electron and hole charge densities within the perovskite NC and (ii) the non-radiative hot-carrier cooling rates can become extended due to the large energy spacing between $\boldsymbol{s_{e/h}}$ and $\boldsymbol{p_{e/h}}$ electronic states.

The rest of this dissertation contains published research exploring photo-induced dynamics in the pristine NC explored here, a transition metal Mn^{2+} doped NC which introduces new d-d radiative relaxation channels, the role of polaronic effects on the radiative and non-radiative relaxation of charge-carriers, and the influence of various surface chemistries and surface-vacancy defects on exited-state dynamics.

4. PHONON-BOTTLENECK IN A LEAD-HALIDE PEROVSKITE NANOCRYSTAL

4.1. Introduction

$APbX_3$ (A=Cs,methylammonium(MA), formadamidinium (FA): X=I, Br, Cl) lead halide perovskite nanocrystals[29] (NCs) have become popular materials for a variety of technology applications due to their facile wet-chemical synthesis, tunable chemical composition, and size-dependent photo-physical properties. The 'phase space' of possible chemical compositions – regimes of electronic confinement, surface termination, and doping – allow for engineering and optimizing electronic excited-state processes for device applications. In semiconducting nanocrystals, the primary excited-state processes of interest for devices are: hot carrier cooling, charge carrier recombination, and carrier multiplication which is also known as multi-exciton generation (MEG). For photovoltaics, slow hot carrier cooling, long charge carrier lifetimes, and MEG are needed to maximize power conversion efficiency[60]. For light-emitting applications, such as lasing and LEDs, fast hot carrier cooling with fast radiative recombination and slow non-radiative recombination is needed to maximize external quantum efficiencies.

Experimental and computational studies have shown correlations between rates of excited state processes and the chemical composition/physical structure of $APbX_3$ perovskites. Halide anion composition has been shown to have significant effects on non-radiative recombination rates, with iodides providing slower rates than bromine based perovskites[61]. Cation composition has been shown to have an impact on hot carrier cooling and non-radiative recombination rates, with organic cations providing faster rates than inorganic Cs^+ ions [62-63]. It is also expected that organic cations promote polaron formation which would screen phonons, reducing cooling and nonradiative recombination[64-66]. The role of confinement on hot carrier cooling indicates that at low excitation densities ($\sim 10^{17}$ cm^{-1}) strong confinement slows down carrier cooling in $MAPbBr_3$

and $FAPbI_3$ NCs[67,11], while at high excitation densities (~10^{19} cm^{-1}) the trend reverses and rates slow down with increased confinement. Efficient MEG has been observed in confined $FAPbI_3$ NCs[11] which has been supported by computer simulations [36]. Theory predicts that radiative recombination rates show a strong dependence on quantization, with weak/intermediately confined NCs showing faster rates compared to strongly confined NCs because of bright triplet excitons[68].

A common feature that all of the above mentioned $APbX_3$ materials have is that their valence band is composed of hybridized *X-np* (n=principle quantum number) and *Pb-6s* orbitals while the conduction band is comprised of hybridized *Pb-6p* orbitals which experience a large spin-orbit coupling (SOC). Theory and calculations have shown that this type of electronic structure is beneficial for high defect tolerance[69-70], but its role on excited state dynamics has been relatively unexplored. On one hand, it would be expected that SOC would increase rates of carrier cooling due to the relaxation of spin selection rules for non-adiabatic coupling (NAC). On the other hand, the SOC interaction results in the J=1/2 angular momentum state being spilt from the J=3/2 state and reduces the bandgap by ~0.70 eV[71-72]. One expectation is that such a large energy splitting would make the density of states (DOS) near the conduction band edge sparse. Combined with the quantization of bands that occurs in strongly confined NCs, it would seem possible that subgaps appear near the band edges of $APbX_3$ NCs and cause a 'phonon bottleneck'. In bulk $MAPbI_3$ it has been reported that SOC accelerates carrier cooling due to enhanced electronic coupling[73], but the role of confinement on carrier cooling has not been investigated to date.

Here we use computational methods to investigate photo-induced excited-state dynamics in a fully-passivated $CsPbBr_3$ NC in the strong confinement regime. Our excited-state dynamics

couple electronic and nuclear degrees of freedom through NACs allowing hot carriers to dissipate energy as phonons which compete with radiative energy dissipation. We find that the large spin-orbit coupling of lead 6-p states introduces are large subgap and slows down hot-carrier cooling kinetics.

4.2. Methodology

4.2.1. Spinor Kohn-Sham Orbitals and Spin-Orbit Coupling

Computing non-adiabatic couplings with spinor orbitals.

$$\sum_{\sigma,\sigma'=\alpha,\beta} (-\delta_{\sigma\sigma'}\nabla^2 + v_{\sigma\sigma'}^{eff}(\vec{r}))\varphi_{i\sigma}(\vec{r}) = \varepsilon_{i,\sigma\sigma'}\,\varphi_{i\sigma'}(\vec{r}) \tag{4.1}$$

$$v_{\sigma\sigma'}^{eff}(\vec{r}) = \begin{pmatrix} v_{\alpha\alpha}^{eff}(\vec{r}) & v_{\alpha\beta}^{eff}(\vec{r}) \\ v_{\beta\alpha}^{eff}(\vec{r}) & v_{\beta\beta}^{eff}(\vec{r}) \end{pmatrix} \tag{4.2}$$

For equations (4.1)-(4.2), $\delta_{\sigma\sigma'}$ is the Kroenicker-delta function, σ and σ′define spin projections α or β, $v_{\sigma\sigma'}^{\mathrm{eff}}(\vec{r})$ is the spin-dependent external potential, and $\varphi_{i\sigma}(\vec{r})$ is a spin-dependent KSO. For NCS DFT, equations (4.1)-(4.2) are not constrained by spin-orthogonality allowing for non-zero off-diagonal effective potentials. These off-diagonal elements produce a set of equations that couple the spin states α and β. The solution to the set of NCS DFT equations is represented as a superposition of spin- α and spin- β states $|\alpha\rangle = \begin{bmatrix}1\\0\end{bmatrix}$ and $|\beta\rangle = \begin{bmatrix}0\\1\end{bmatrix}$ with spatially dependent coefficents $\varphi_{i\alpha}(\vec{r})$ and $\varphi_{i\beta}(\vec{r})$. These solutions are commonly referred to as spinor KSOs (SKSOs) shown in equation (4.3).

$$\varphi_i^{SKSO}(\vec{r}) = \begin{Bmatrix} \varphi_{i\alpha}(\vec{r}) \\ \varphi_{i\beta}(\vec{r}) \end{Bmatrix} \tag{4.3}$$

SKSOs obey the normalization, equation (4.4), and orthogonality, equation (4.5)

$$\int d\vec{r}\{\varphi_{i\alpha}^* \quad \varphi_{i\beta}^*\}\begin{Bmatrix}\varphi_{i\alpha}\\ \varphi_{i\beta}\end{Bmatrix} = \int d\vec{r}\left(\varphi_{i\alpha}^*(\vec{r})\,\varphi_{i\alpha}(\vec{r}) + \varphi_{i\beta}^*(\vec{r})\,\varphi_{i\beta}(\vec{r})\right) = 1 \tag{4.4}$$

$$\int d\vec{r}\left(\varphi_{i\alpha}^{*}(\vec{r})\,\varphi_{j\alpha}(\vec{r}) + \varphi_{i\beta}^{*}(\vec{r})\,\varphi_{j\beta}(\vec{r})\right) = \delta_{ij} \tag{4.5}$$

Within the NCS DFT framework, relativistic effects can be incorporated using 2nd order scalar relativistic corrections.

$$H^{\text{relativistic}} = H^{SR} + H^{SOC} \tag{4.6}$$

The relativistic Hamiltonian from equation (4.6) is composed of two terms: H^{SR} is the scalar relativistic term and H^{SOC} is the SOC term which can be represented as

$$H^{SOC} = \frac{\hbar}{4m^2c^2}\frac{1}{r}\frac{\partial v_{\text{sphere}}^{KS}}{\partial r}\vec{L}\cdot\vec{S} \tag{4.7}$$

where $\vec{L}$ is the angular momentum operator and $\vec{S}$ is composed of Pauli spin matrices ($\hat{\sigma}_x$, $\hat{\sigma}_y$, $\hat{\sigma}_z$).

4.2.2. Observables Computed with Spinor Kohn-Sham Orbitals

Optical transitions between SKSO *i* and *j* can be found through transition dipole matrix elements

$$\langle\vec{D}_{ij}\rangle = e\int d\vec{r}\{\varphi_{i\alpha}^{*} \quad \varphi_{i\beta}^{*}\}\vec{r}\begin{Bmatrix}\varphi_{j\alpha}\\ \varphi_{j\beta}\end{Bmatrix} = e\int d\vec{r}\left(\varphi_{i\alpha}^{*}(\vec{r})\vec{r}\varphi_{j\alpha}(\vec{r}) + \varphi_{i\beta}^{*}(\vec{r})\vec{r}\,\varphi_{j\beta}(\vec{r})\right) \tag{4.8}$$

and NACs computed with the SKSO basis is

$$\hat{V}_{ij}^{NAC}(t) = -\frac{i\hbar}{2\Delta t}\int d\vec{r}\left\{\varphi_{i\alpha}^{*}(\vec{r},\{\vec{R}_I(t)\}) \quad \varphi_{i\beta}^{*}(\vec{r},\{\vec{R}_I(t)\})\right\}\cdot\begin{Bmatrix}\varphi_{i\alpha}\left(\vec{r},\{\vec{R}_I(t+\Delta t)\}\right)\\ \varphi_{i\beta}\left(\vec{r},\{\vec{R}_I(t+\Delta t)\}\right)\end{Bmatrix} + h.c. \tag{4.9}$$

$R(t)$ represents ionic displacements due to thermal motion with $\varphi_j^{SKSO}(\vec{r};\ R(t))$ being an adiabatic state that depends parametrically on $R(t)$. The inner product is computed at adjacent timesteps t and $t+\Delta t$. Computing excited-state observables

4.2.3. Computational Details

The ground-state electronic structure of our atomistic model was found using DFT with the generalized gradient approximation (GGA) Perdew-Burke-Ernzerhof (PBE) functional[74] in a

plane-wave basis set along with projector augmented-wave (PAW) pseudopotentials[75-76] in VASP[77] software. From the ground-state nuclear configuration computed with the GGA functional, single point calculations where done using noncollinear spin DFT including the SOC interaction which where used to compute observables of the system. All calculations were performed at the Γ point. A simulation cell size of 31x31x31 Å with 7 Å of vacuum in each direction.

4.3. Results

4.3.1. Ground-State Electronic Structure and Optical Absorption Compared to Experiment

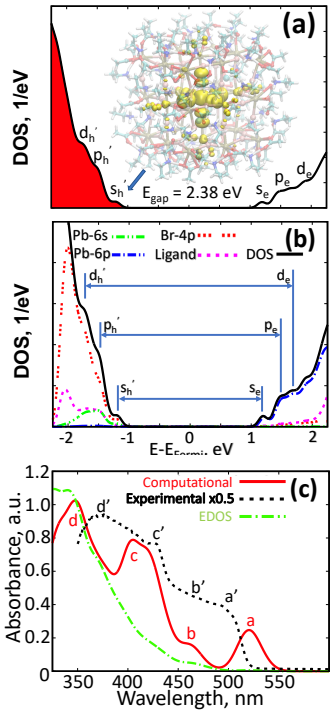

Figure 4.1: (a) DOS of the NC computed in SKSO basis giving a bandgap of 2.38 eV. There are no states inside the bandgap indicating the NC is properly passivated. The inset shows the isosurface of the HOMO state with the electron density residing inside the $CsPbBr_3$ NC. **(b)** pDOS corresponding to DOS from **(a). (c)** Computed absorption (red, solid), experimental spectra (black, dotted), and EDOS (green, line-dot). EDOS represents the density of possible optical transitions while computed absorption spectra weights each transition with the associated oscillator strength. Relevant features are alphabetically labeled (primes corresponding to experiment data) and described in the main text.

SKSO DOS for the geometry optimized NC is shown in **Figure 4.1(a)** and is computed as $g_{SKSO} = \sum_i \delta\left(\varepsilon - \varepsilon_i^{SKSO}\right)$ with the delta function being approximated as a Gaussian distribution. Shaded regions represent occupied states. There are four relevant observations about the DOS. First, there is a 'clean' bandgap indicating the NC is properly passivated with no trap states[78] . Second, the band gap has a value of 2.38 eV (521 nm). Third, each eigenenergy is twice degenerate which follows experiment[79] and theory[68]. Lastly, the DOS peaks near the band edges show a trend analogous to particle in a box envelope functions which we label with symmetry indices s_x, p_x, and d_x (x=e,h), respectively.

pDOS calculations, see **Figure 4.1(b)**, show the atomic orbital composition of the conduction and valence band. In the valence band, it is seen that the s_h', p_h', and d_h' states have the same atomic orbital composition of Br-4p (red, dotted-space-dotted), Pb-6s (green, dot dash), and O-2p (pink, dashed), but in different proportions. States deeper in the valence band have a greater proportion of Br-4p contribution to the DOS. For the bottom of the conduction band, the s_e, p_e, and d_e states have essentially the same proportion of Pb-6p (blue, dot-dash-dash-dot) states and experience little hybridization with ligand states. An interesting note is that within 1.5 eV of the conduction and valence band edge, there was no hybridization of the ammonium ligands with the NC and only the O-2p states of the deprotonated carboxylate contribute electron density for chemical bonding.

From the ground state electronic structure we compute optical spectra, **Figure 4.1(c),** of the NC from under IOA. Within **Figure 4.1(c)** we plot computed absorption spectrum (red, solid), EDOS (green, dash dot), and experimental spectra of $CsPbBr_3$ NCs with mean size ~10nm (black, dashed). Alphabetical labels, ascending order in energy/descending in

wavelength, correspond to characteristic peaks in the computed and experimental spectrum which will be discussed throughout the text.

Physically, EDOS represents the degeneracy of optical transitions for a given energy $EDOS^{SKSO}(\varepsilon) = \sum_{ij} \delta(\varepsilon - \Delta\varepsilon_{ij})$ where $\Delta\varepsilon_{ij}$ is the transition energy. This allows to compare how spectral features are enhanced, or suppressed, by physical constraints of the system. In our case the physical constraint of the system is quantization of electronic states due to boundary conditions. Comparing EDOS to the computed absorption spectrum it is seen that the lowest energy transitions, which have low degeneracy, are weighted much larger than high energy transitions. This can be seen more explicitly using a log scale were the lowest energy transition feature 'a' is almost 2 orders of magnitude higher than EDOS. The 'b' and 'c' features of the computed spectra differ from EDOS by ~0.5 orders of magnitude. The experimental spectrum also shows the same trend, but with the 'b' feature being more intense. This can be interpreted as the s_h' → s_e transitions having much larger oscillator strengths than other direct type transitions (such as p_h' → p_e and d_h' → d_e) or other symmetry indirect transitions.

In comparing the computed and experimental spectra we see that, even though the atomistic model and experimental NCs differ in edge length by roughly an order of magnitude, similar characteristic peaks appear. The peaks **a/a'**, **c/c'**, and **d/d'** can be attributed to symmetric transitions s_h' → s_e , p_h' → p_e , and d_h' → d_e , respectively. The major difference between the two spectra is in the 450nm to 500nm region labeled **b** and **b'**. In this region, where dipole forbidden transitions s_h→p_e and s_e→e_h are expected, absorption is more intense in the experimental spectra than in the computed spectra. This can be attributed to the fact that experimental samples have a distribution of NC sizes which will absorb with a range from approximately 450nm (large confinement regime)[29,80,81] to 510nm (intermediate confinement regime).

4.3.2. Excited-State Dynamics – Slowed Hot-Electron Cooling

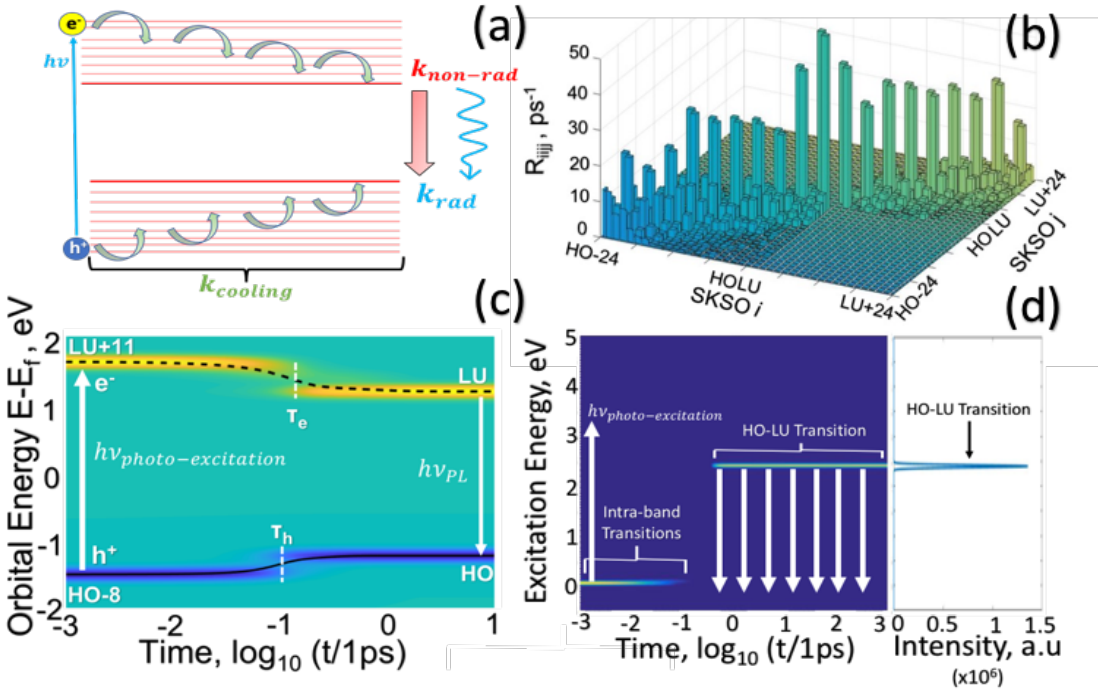

Figure 4.2: (a) Schematic of photo-induced excited-state dynamics investigated in this work. A photo-excitation generates photo-excited electron in the conduction band and photo-induced hole in valence band. On a picosecond timescale, hot carriers cool to LU/HO states by dissipating heat though NAC with phonon modes of the NC with rate $k_{cooling}$. On a nanosecond timescale, free carriers recombine through radiative/non-radiative channels with rates $k_{non\text{-}rad}$ and k_{rad} **(b)** SKSO computed Redfield tensor which represents hot carrier cooling. Tensor elements, in units of 1/ps, describe state-to-state transitions of populations due to NAC. (**c)** Hot carrier cooling for the specific optical transition HO-8 to LU+11 which is an intense $p_h \rightarrow p_e$ type transition. Green represents background reference, yellow represents average occupation of charge in conduction band, and blue represents average occupation of charge in valence band. Horizontal dotted/solid lines represent energy expectation values of charge carriers and vertical dashed lines represent hot carrier cooling $\tau_{cooling}$ fit to a single exponential decay. **(d)** Time resolved and time integrated PL along the excited state trajectory corresponding to **Figure 2(c).** Before cooling to HO/LU states, hot carriers can emit low energy IR photons to dissipate energy which competes with non-radiative transitions. Once carriers relax to HO/LU states, the NC emits PL in the visible spectrum.

The philosophy of our excited-state dynamics calculations is illustrated in **Figure 4.2(a)**. We assume steady-state absorption between discrete states HO-x and LU+y with energy $h\nu$ creating photo-induced holes and photo-excited electrons. At t=0 the excitation source is removed and fully populated LU+y and HO-x states thermalize to the band-edge states LU and

HO with a rates $k_{cooling}$. Once both charge carriers relax to respective HO/LU states, they can recombine though radiative or non-radiative relaxation channels with rates k_{rad} and $k_{non-rad}$. The rate constants k_{rad} and $k_{non-rad}$ determine the PLQY as $\frac{k_{rad}}{k_{rad}+k_{non}-rad}$.

For our excited state dynamics, we chose initial conditions based on high probability photo-excitations. For this letter we will use the HO-8 to LU+11 transitions as an example. This transition represents a p_h'→p_e type of transitions from DOS, see **Figure 4.1(b)**, and corresponds to the 'c' type peak in the absorption spectra, see **Figure 4.1(c)**. Carrier cooling after the HO-8 to LU+11 transition with energy $hv_{photo-excitation}$ is illustrated in **Figure 4.2(c).** The green color represents ground-state charge density, yellow represents gain in charge density, $\Delta n>0 = e^-$, and blue represents loss of charge density, $\Delta n<0 = h^+$. Dashed and solid curves represent average electron energy $\langle \Delta\varepsilon_e \rangle(t)$ and hole energy $\langle \Delta\varepsilon_h \rangle(t)$ during relaxation, respectively. The x-axis is a normalized log scale where 0 represents 1 ps. τ_e and τ_h represent times of relaxation from *LU+y* to *LU* and *HO-x* to *HO.* We assume single exponential energy decay curves with relaxation rate $[\tau_e]^{-1} = k_e$ and $[\tau_h]^{-1} = k_h$. Once the carriers relax to the LU/HO states there is the possibility of radiative recombination and the emission of a photon of energy hv_{PL}. We note two observations about **Figure 2(c):** (1) Both carriers show fast sub-picosecond carrier cooling on the order of 10^2 fs, which agrees with reported carrier cooling studies on $CsPbBr_3$ NCs [79,82,83]; (2) The photo-excited electron shows a long decay of hot carriers near the LU state (faint yellow smear above LU state). This feature is explored further in later sections. Along the excited-state trajectory, radiative relaxation mechanisms, such as carrier cooling through IR emission and radiative charge recombination, can compete with non-radiative relaxation. **Figure 4.2(d)** illustrates radiative relaxation along the excited state trajectory. The left part of the figure shows time resolved emission along the trajectory in $\log_{10}$ time scale and the right part shows the time-

integrated emission. The initial condition is the same as that for **Figure 4.2(c)** with an initial photo-excitation of energy $h\nu_{photo-excitation}$ and radiative relaxation thereafter. It is seen that there are low energy IR photons emitted on the 1-100 fs timescale and after both charge carriers relax to respective HO/LU states there is bright PL.

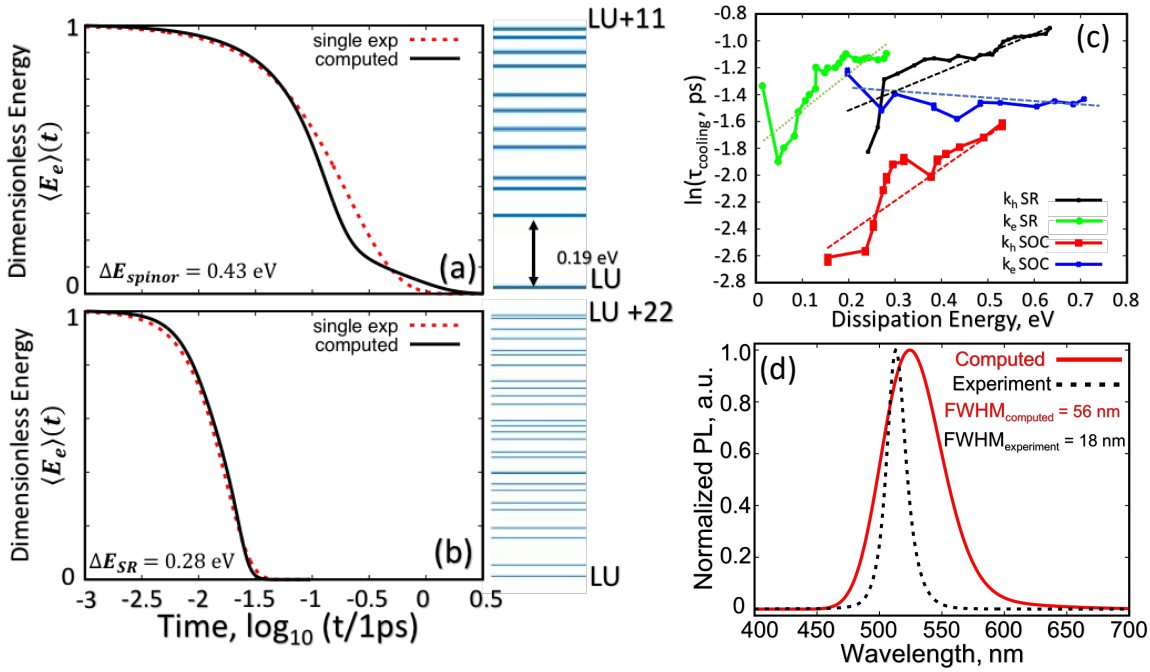

Figure 4.3: (a)-(b) Comparison of hot-electron carrier cooling using **(a)** spinor and **(b)** spin-restricted electronic basis. The numerically solved relaxation (black,solid) is compared to a single exponential fit (red, dotted). The spinor basis shows a 'bottle-neck' effect which is attributed to the large 0.19 eV electronic subgap. **(c)** Carrier-cooling times as a function of dissipation energy. **(d)** Comparison of computed photoluminescence linewidth (red, solid) to experimental samples (black, dotted).

To highlight the changes in hot electron cooling with different basis we plot the normalized energy relaxation $\langle \boldsymbol{E_e} \rangle(\boldsymbol{t})$ along side relative alignment of energy bands for SKSO and SR in **Figure 4.3(a)-(b)**. The two curves plotted are of the computed energy relaxation (black, solid) and the single exponential fit (red, dotted). It is seen for the SR computed relaxation, **Figure 4.3(b)** that the relaxation occurs very quickly and closely follows a single exponential decay associated with gap law. For SOC computed relaxation, **Figure 4.3(a)** the early dynamics follow a single exponential decay while near the LU state the dynamics slows

down dramatically. This can be attributed to the large 0.19 eV subgap between LU+3/LU+2 and LU+1/LU energy states. This feature is explored more in the discussion section.

Generally, hot carrier cooling rate is a function of excitation energy. If carrier cooling follows a 'gap law' type of trend then the quantity $\ln(\tau_{cooling}) \propto \Delta E_{dissipation}$ where $\Delta E_{dissipation} = \langle \Delta\varepsilon_{e/h} \rangle(t) - \langle \Delta\varepsilon_{e/h} \rangle(\infty)$. In **Figure 4.3(c)** we plot $\ln(\tau_{cooling})$ as a function of $\Delta E_{dissiption}$ for hot a electron/hole using the SKSO basis (blue, cross/red, square) and a spin-restricted (SR) basis with no SOC interaction (green, big circle/black, small circle). Lowest dissipation energy represents the LU+3/LU+2 to LU+1/LU or HO-3/HO-2 to HO-1/HO transition for SOC calculations and LU+1 to LU or HO-1 to HO transitions for SR calculations. The interesting quantities to compare are the cooling rates as a function of electronic basis (SKSO vs. SR). For hot hole cooling, it is seen that both the SR and SOC computed rates share similar trends and have a similar average slope for the linear fit and weakly obey gap law trends. For hot electron cooling, two different trends are observed between the SR and SOC calculations. The SR shows a trend similar to gap law while the SOC calculation shows that carrier cooling rates is slightly independent of excitation energy and is slowest for the lowest transition energy. This indicates that for hot-hole cooling, SOC has negligible effects while for hot electrons SOC significantly alters excited state dynamics.

The PL linewidth from the excited-state trajectory in **Figure 4.2(d)** is artificially narrow due to an approximation that the average PL emission will come from minima of the potential energy surfaces. To compute PL linewidth in our atomistic model, we implement a previously reported molecular dynamics photoluminescence (MDPL) protocol[84] to account for perturbations of HO-LU oscillator strength along MD trajectory. **Figure 4.3(d)**compares the normalized PL curves of our model (red, solid) and of the experimental sample (black, dotted). The full-width

half-max (FWHM) for our computational model is 56 nm and our experimental sample shows a FWHM of 18 nm. The experimental sample is consistent with other reported values of linewidths for $CsPbBr_3$ samples with mean edge length ~10nm [29,85]. We attribute the broader linewidth of the computational model to the enhanced coupling of charge carriers to surface states in our small atomistic model. Increasing PL linewidth with decreasing NC size has been observed experimentally in PbS NCs[17].

To compute the PLQY, we consider a two state model where radiative and non-radiative transition rates are determined from the Einstein coefficient for spontaneous emission, A_{ij}, and the Redfield tensor elements R_{iijj}, respectively. For the Einstein coefficient we use oscillator strengths f_{ij} that are time averaged over the MD trajectory; $< f_{ij} > = \frac{1}{T}\sum f_{ij}\big(R(t)\big)$ where T is the total interval of the trajectory and $R(t)$ represents ionic coordinates as function of time. Since the energy eigenvalues for the conduction and valence band edge are both twice degenerate, there are four possible transitions: LU→HO, LU+1→HO, LU→HO-1, and LU+1→HO-1. This means the terms k_{rad} and $k_{non-rad}$ will be the sum of the respective recombination rates, $\frac{\sum k_{rad}}{\sum k_{rad}+\sum k_{non-rad}}$. Values of k_{rad} and $k_{non-rad}$ for each transition are shown in **Table 4.1**. These rates give a resultant PLQY of 53%.

Table 4.1: Table showing the four possible radiative and non-radiative transitions in our two state (twice degenerate) model. $< f_{ij} >$ represents the time averaged oscillator strength between state HO-x and LU+y and is used to compute k_{rad} through the Einstein coefficient for spontaneous emission. $k_{non-rad}$ is found from Redfield tensor elements, where k_{rad} and $k_{non-rad}$ determine PLQY.

HO-x	LU+y	$< f_{ij} >$	k_{rad} [1/ns]	$k_{non-rad}$ [1/ns]	PLQY
HO	LU	0.32	1.01	0.85	53%
HO	LU+1	0.30	0.95	0.73	
HO-1	LU	0.30	0.94	1.01	
HO-1	LU+1	0.29	0.92	0.76	

4.4. Discussion

When placing the computed results of our atomistic model in context with reported experimental results in the literature, it is important to keep a few points in mind. First, we note that our fully passivated $CsPbBr_3$ atomistic model is roughly an order of magnitude smaller than what is generally seen in experiment and is ~3x smaller than the smallest NCs reported in literature. This implies that surface effects should be more pronounced than in experiment. Second, the $RCHOO^-/RNH_3^+$ organic ligands used for surface passivation are one of 3 typical configurations reported in the literature for oleic acid and oleylamine based synthesis, with the others being Cs(oleate) / RNH_2 and RNH_3^+ / Br^-. The length of the hydrocarbon chains on the acetate/ethylammonium ligands is significantly smaller than oleic acid and olylammonium ligands in experiment as well. Lastly, our excited-state dynamics methodology treats photo-induced charge carriers as independent particles coupled to phonon modes, neglecting Coulombic interactions. This implies that our excited-state calculations should be comparable to experiments with low carrier densities $\langle N \rangle < 1$.

It is generally known that electronic structure calculations based on DFT applied to $APbX_3$ perovskites using the GGA functional without including SOC bandgaps roughly corresponds experimentally determined bandgaps because of a cancelation of errors. For our $Cs_8Pb_{27}Br_{54}$ model, when only a GGA functional is used, a bandgap of 3.12 eV is found. With the inclusion of SOC the gap reduces to 2.38 eV, a difference of 0.74 eV, which is in good agreement to what has been reported previously[71, 86] . This gives a bandgap which resembles $CsPbBr_3$ NCs in the intermediate confinement regime with an edge length of ~10 nm. Although it is accidental that the computed bandgap with GGA+SOC is very similar to experiment, it is a

convenient accident for excited-state dynamics calculations, since rates of recombination across the bandgap depend inversely on the bandgap energy.

Generally, for dipole-induced transitions, selection rules forbid transitions to envelope functions that have opposite parity, such as $s_h \rightarrow p_e$. These restrictions are relaxed when symmetries, such as rotational or inversion, are broken. In the case of $APbX_3$ NCs it is generally known that inversion symmetry of the crystal lattice is distorted due to the observation of Rashba effects[87-88]. This also indicates that selection rules may be relaxed in $APbX_3$ NCs due to symmetry breaking of the crystal lattice. From the computed spectra shown in **Figure 4.1(c)** it is observed that in the 'b' region where asymmetric $s_h \rightarrow p_e$ or $p_h \rightarrow s_e$ are expected, a spectral feature appears, which we attribute to symmetry breaking.

From our two state model of radiative and non-radiative recombination we found that the fully passivated $Cs_8Pb_{27}Br_{54}$ NC with time-averaged k_{rad} and $k_{non-rad}$ showed a PLQY of 53%. Generally, non-unitary PLQY in NCs and QDs is attributed to undercoordinated surface atoms which create trap states that significantly decrease k_{rad}. But here we have a NC with all surface atoms coordinated to $RCOO^-$ and RNH_3^+ ligands along the MD trajectory which do not desorb from the surface. We raise a few possibilities which could impact k_{rad} and $k_{non-rad}$. First, during the MD trajectory, oscillator strengths will vary due to bond elongation/contraction. Elongation of Pb-O bonds at the surface can produce momentary trap states that quench the oscillator strength. Second, non-radiative energy dissipation is dependent on phonon frequencies coupled to electronic states. It has been shown that passivating ligands can contribute to the spectral density and enhance carrier cooling in NCs and QDs[89]. Other atomistic models[61, 90] have indicated that surface passivation has an impact on non-radiative recombination rates as well, with inorganic passivation ligands significantly reducing $k_{non-rad}$. Thus we suspect that a Br^-

/RNH_3^+ passivation would provide a PLQY closer to 100% due to the slower ionic motion of Br^- compared to the $RCHOO^-$ ligand. Another possibility is that the surface electron-phonon coupling is a function of the hydrocarbon chain length of the organic passivating ligand. Long chain hydrocarbons would have less degrees of freedom for vibrational motion due to interacting with neighboring ligands, while short chain ligands are less impacted by steric interactions.

During the excited state dynamics trajectory, after a steady state p_h' $\rightarrow p_e$ optical transition, it was observed that hot electron cooling is slowed down near the band edge and displayed 2nd order kinetics due to the large sub-gap between LU/LU+1 and higher energy states. For larger NCs the sub-gap would likely become smaller due to the DOS becoming denser near the band edge, with single decay kinetics. In a recent transient absorption experiment, carrier cooling was explored in the low carrier density regime ($\langle N \rangle = 0.1$) for various sizes (5nm, 9nm, and 12nm) of CH_3NH_3PbBr3 NCs with an excitation energy of 3.1 eV [11]. This transition energy is comparable to the 3.01 eV p_h'$\rightarrow p_e$ transition explored here. The experimental data suggests that with decreasing size, carrier cooling slows down near the band edge. This seems to support our claim that the combination of giant SOC and a sparse DOS near the band edge slows down carrier cooling in $APbX_3$ NCs.

4.5. Conclusion

In conclusion, we use spinor Kohn-Sham orbitals (SKSOs) as a basis to compute excited-state dissipative dynamics in a fully-passivated $CsPbBr_3$ NC using Redfield theory in density matrix formalism to describe electron-phonon interactions. From the rates k_{rad} and $k_{non-rad}$ we computed a PLQY of 53%, which is lower than what would be expected for a fully surface passivated NC without surface trap states. This indicates that surface termination and NC size plays an important role in determining PLQY. We attribute the lower than expected PLQY value

to enhancement of $k_{non-rad}$ through additional degrees of freedom and the normal modes of short-chain passivation ligand used for the atomistic model. Computed PL linewidths of the atomistic model are ~3x larger than our ensemble measurements on NCs approximately 10nm in edge length. This is also attributed to enhanced coupling to surface phonons. Computed hot carrier cooling rates compared favorably to reports in the literature of fast sub-picosecond cooling on the scale of ~300 fs under low excitation densities. With the inclusion of SOC in excited-state dissipative dynamics, it was observed that electronic coupling was enhanced, which has been reported in calculations of bulk $MAPbI_3$, but hot electron cooling was slowed down, which we attribute to a large (~0.20 eV) nonresonant subgap above the conduction band edge and a subsequent "phonon bottleneck".

5. POLARONIC CHARGE CARRIERS IN LEAD-HALIDE PEROVSKITE NANOCRYSTAL: SPECTRAL SIGNATURES, HOT-CARRIER COOLING, AND INFRARED PHOTOLUMINESCENCE

5.1. Introduction

The performance of solid-state opto-electronic devices, such as photovoltaic cells, light-emitting diodes (LEDs), lasers, and quantum computers, depends on factors such as the ground-state electronic structure of a material, the radiative and non-radiative dynamics of charge-carriers in the excited-state, light-matter interactions, and the interaction between interfaces of layers of materials in a device. Engineering the performance of these devices requires knowledge on how to tune features of electronic structures (i.e. band-gap engineering) which are favorable for a desired purpose, such as maximizing the absorbance power density in photovoltaics, and alter the rates of excited-state processes, such as using confinement to enhance radiative recombination kinetics of charge-carriers for LEDs.

In the context of using solid-state materials as light emission sources, there are three primary regimes of interest: ultraviolet, visible, and infrared (IR). Here we will focus on infrared emission sources. Utilizing IR electronic transitions within solid-state materials, as compared to thermal IR emission from vibrational modes, are beneficial since they have resonances which provide narrow-band emission while vibrational transitions provide broad-band emission. Within the IR spectrum there are four distinct regions: 700nm-1.5μm near IR (NIR), 1.5μm – 3μm small wave IR (SWIR), 3μm – 8μm medium wave IR (MWIR) and 8μm-15μm long wave IR (LWIR). Within the NIR and SWIR region the most common application for IR emission is for low loss telecommunications. For MWIR and LWIR the most common use is for thermal imaging and tracking.

To obtain efficient IR photoluminescence (PL) three criteria are needed: (i) transition energies within the range of 0.1 eV to 1.8 eV (ii) fast radiative recombination (iii) slow non-radiative recombination. Traditionally, transition energies tuned for IR PL have been obtained by utilizing the intrinsic bandgap of a material, using electronic confinement to tune the bandgap[91], using heterostructures to tune the transition energy[92], and doping to tune the bandgap[93]. Recently, creating surface defect states has shown the ability to controllably tune the transition energy [94]. Increasing the rates of radiative recombination can be achieved by increasing the exciton binding energy through electronic confinement[95] or dielectric confinement[96]. Slowing down non-radiative recombination rates can be accomplished by reducing the interaction of an excited-electronic state with its external environment, such as reducing temperature or using nanostructures to suppress phonon modes[97].

$APbX_3$ (A=Cs, methylammonium(MA), formadamidinium (FA): X=I, Br, Cl) lead halide perovskites belong to a class of materials that have shown promise for high efficiency LEDs. This is due to a combination of facile wet-chemical synthesis coupled with high defect tolerance, physical tuneability in the form of nanostructures, such as nanocrystals[29] (NCs), nanowires[98], thin-films[99], and layered materials[26], and exotic excited-state properties[68]. In particular, thin-films of $MAPbI_3$ have shown unusual charge-carrier transport properties, such as long non-radiative recombination rates in polycrystalline samples with high-defect densities. Recent work has suggested that the extended non-radiative lifetimes could potentially be attributed to photo-induced large polaron formation due to the cooperative motion of A site cations within the perovskite which trap the charge carriers into separate positive (hole) and negative (electron) polaronic states[28,65,100,66].

Polarons, quasi-particles formed due to the static coupling of electronic and nuclear degrees of freedom described by the Fröhlich Hamiltonian[43], are typically observed in polar crystals and have a range of sizes which are based on the strength of the electron-phonon coupling. The coupling parameter is generally referred to as α. Large α produces small polarons, which trap the charge carriers to a single site within the lattice, and smaller α produces large polarons, which trap the charge carrier across multiple unit cell lengths. Similar to other quasi-particles, polarons have an electronic structure with the lowest polaron energy state being the polaron ground-state (PGS) and the next highest energy state being the relaxed excited-state (RES)[101].

Polarons are also expected to be optically active and display two contrasting absorption mechanisms: dipole-allowed within the polaron potential well which requires conservation of angular momentum $\Delta l = \pm 1$ and photoionization of the bound polaron into the conduction/valence band continuum with a transition energy threshold $\omega = 3E_p$, where E_p is the polaron binding energy[102]. Optical transitions within the polaron potential are defined by discrete, atomic like resonant transitions which scale with the binding energy E_p. This means that small polarons (large E_p) display higher energy transitions than large polarons (smaller E_p). Signatures of polaron photoionization is an absorption maximum near the threshold energy $\omega = 3E_p$ with an asymmetric tail towards the higher energy transitions. Recent transient absorption experiments have explored the optical response of excited-states in films of $MAPbI_3$ and observed IR absorption characteristics which were attributed to photo-ionization of large polarons into the continuum band states[103,104].

Large polarons in $APbX_3$ perovskites have the necessary energy spectrum to be IR photoluminescence (PL) sources. Considering that absorption and emission are inverse processes

(i.e. the transition dipole operator is Hermitian), it seems conceivable to obtain IR PL from large polarons. The efficiency of IR PL would be determined by the kinetics of radiative and non-radiative recombination. Interestingly, polarons are known for screening phonons which slows down non-radiative transitions. Also, in a previous computational modeling work we reported slow hot-carrier cooling in the conduction band of a $CsPbBr_3$ NC atomistic model due to large spin-orbit coupling interaction and strong electronic confinement[105]. With the combination of a low conduction band DOS, large sub-gaps, and phonon-screening due to polaron formation it seems possible that radiative recombination can be competitive with non-radiative recombination within the polaron potential well. Continuing from previous work, here we use Density Functional Theory (DFT) based computational methodology[106,107] to model the excited-state dynamics of hot-polarons in an atomistic $CsPbBr_3$ NC to test if polarons can be a potential IR PL source.

5.2. Methodology

5.2.1. Polaronic Electronic States in DFT Formalism

Non-collinear spin DFT[108-109] is used as the electronic basis and we include the spin-orbit coupling (SOC) interaction due to the large angular momentum of conduction band Pb^{2+} *6p* orbitals. A self-consistent non-collinear spin DFT uses four densities $\rho_{\sigma\sigma'}(\vec{r})$ and rests on the KS equation

$$\sum_{i,\sigma'=\alpha,\beta}\left(-\delta_{\sigma\sigma'}\nabla^2 + v_{\sigma\sigma'}^{eff}\left[\rho_{\sigma\sigma'}(\vec{r})\right]\right)\varphi_{i\sigma}(\vec{r}) = \varepsilon_i\,\varphi_{i\sigma'}(\vec{r}) \tag{5.1}$$

In eq. 5.1, α and β are orthogonal spin indices, $v_{\sigma\sigma'}^{eff}[\rho_{\sigma\sigma'}(\vec{r})]$ is the 2x2 matrix operator ofeffective potential. In accordance with the self-consistent Kohn-Sham theorem, the 2x2 effective potential is a functional of the electronic density for a N electron system $v_{\sigma\sigma'}^{eff} =$

$\frac{\delta E^{TOT}[\rho^N_{\sigma\sigma\prime}]}{\delta \rho^N_{\sigma\sigma\prime}}$. The spin-dependent electronic density $\rho_{\sigma\sigma\prime}$ is dependent on the total number of electrons N. The total energy of the system $E^{TOT}[\rho^N_{\sigma\sigma\prime}]$ consequently depends on the number of electrons and determines the equilibrium ground state geometry when $\frac{\partial E^{TOT}[\rho^N_{\sigma\sigma\prime}]}{\partial R} = 0$ with R representing nuclear degrees of freedom. For the N electron system the equilibrium bond distances will have distance $R^N_{equilib}$. Changing the total number of electrons, through the process of charge injection, $N \pm \Delta N$ changes the forces acting on nuclei $\frac{\partial E^{TOT}[\rho^{N\pm\Delta N}_{\sigma\sigma\prime}]}{\partial R}$ due to having a new electronic density $\rho^{N\pm\Delta N}_{\sigma\sigma'}$. For polaronic models with added/removed charge the equilibrium bond distances will be altered to give an updated equilibrium geometry $R^{N\pm\Delta N}_{equilib}$.

As a starting point, we determine the optimized geometry of the charge neutral model, in the absence of polarons, within the self-consistent DFT with N number of electrons. This corresponds to transforming the Fröhlich Hamiltonian terms to our mixed quantum-classical methodology.

$$H^N_e(r) + H_{ph}(R) + H^{static}_{e-ph}(r,R) = H^N_{SKSO}(r;R) \tag{5.2}$$

$H^N_{SKSO}(r;R)$ describes the electronic and nuclear degrees of freedom where the total energy depends parametrically on the nuclear coordinates R. This defines finding the minima of the potential energy surface (PES) with nuclear coordinates $R^N_{equilib}$ for the N electron system. We use this as a reference state to compare N electron system observables, such as equilibrium bond distances $R^N_{equilib}$, to the polaronic models.

To describe polaronic states we first add/remove charge ΔN from the N electron system to give a total of $N \pm \Delta N$ electrons. Then we do not allow the ions to reorganize around the new charge density $\rho^{N\pm\Delta N}_{\sigma\sigma'}$ keeping the nuclear coordinates fixed from the N electron system

$$H_e^{N\pm\Delta N}(r) + H_{ph}(R) + H_{e-ph}^{static}(r,R) = H_{SKSO}^{N\pm\Delta N}(r;R) \quad (5.3)$$

which is analogous to a Frank-Condon transition from the ground-state PES to the lowest-excited state PES.

Next, we allow the nuclei to reorganize around the charge density $\rho_{\sigma\sigma'}^{N\pm\Delta N}$ with change in nuclear coordinates δR

$$H_e^{N\pm\Delta N}(r) + H_{ph}(R) + H_{e-ph}^{static}(r,R) = H_{SKSO}^{N\pm\Delta N}(r;R+\delta R) \quad (5.4)$$

This term describes finding the minima of the lowest-excited state PES with nuclear coordinates $R_{equilib}^{N} + \delta R = R_{equilib}^{N\pm\Delta N}$. To approximate the electron-phonon interaction from the Fröhlich Hamiltonian, eq. 5.5, we subtract eq. 5.4 from eq. 5.3

$$H_{e-ph}^{N\pm\Delta N}(r,R) = H_{SKSO}^{N\pm\Delta N}(r;R+\delta R) - H_{SKSO}^{N\pm\Delta N}(r;R) \quad (5.5)$$

which describes the reorganization energy from the Frank-Condon states on the excited-state PES to the minima of the excited-state PES.

5.2.2. Computational Details

The ground-state electronic structure of our atomistic model was found using DFT with the generalized gradient approximation (GGA) Perdew-Burke-Ernzerhof (PBE) functional[74] in a plane-wave basis set along with projector augmented-wave (PAW) pseudopotentials[75-76] in VASP[77] software. From the ground-state nuclear configuration computed with the GGA functional, single point calculations where done using noncollinear spin DFT including the SOC interaction which where used to compute observables of the system. All calculations were performed at the Γ point. A simulation cell size of 31x31x31 Å with 7 Å of vacuum in each direction. The charge neutral ground-state structure is optimized using the N electron system. To model polaron formation we add/remove ΔN electrons from the system and reoptimize the structure.

5.3. Results

5.3.1. Polaron Ground-State Electronic Structure and Structural Characterization

In **Figure 5.1(a)-(e)** we show the density of states (DOS) of each spin multiplicity and their IR absorption spectra for the positive polaron model. **Figure 5.1(a)** shows the DOS of the ground-state model (black) singlet (green, dashed), doublet (red, dashed), and triplet (blue, dot-dashed) with the Fermi energy being aligned with the neutral ground-state model. The boxed region of the valence band corresponds to the location of the positive polarons in the DOS. Filled in regions of the curve corresponds to occupations and for clarity we only show ground-state occupations for **Figure 5.1(a). Figure 5.1(b)** shows the IR absorption spectra for singlet (green, solid), doublet (red, dashed), and triplet (blue, dot-dashed) polaron models. It is observed that the singlet and the triplet lowest energy transition are of high intensity compared to the doublet. **Figure 5.1(c)-(e)** shows the positive polaron DOS for the **(c)** singlet, **(d)** doublet, and **(e)** triplet model with the energy axis being aligned to the polaron Fermi level for each respective model. Filled in regions of **Figure 5.1(c)-(e)** correspond of occupied states and white regions being unoccupied hole states which we refer to as positive polaron. The s_h, p_h, d_h labels indicate interpretation of symmetry of the envelope function for those respective bands. A comment on rigorous definition of these labels is provided in SI. For the singlet and triplet polarons **Figure 5.1(c),(e)** it is observed that the Fermi energies align in-between the s_h and p_h bands while for the doublet **Figure 5.1(d)** it is aligned with the s_h band. This is due to each band being twice degenerate[68, 79] for $APbX_3$ perovskites. This also means that the lowest energy optical transition

for **(c)** and **(e)** are $s_h \rightarrow p_h$ types of transitions while **(d)** is of $s_h \rightarrow s_h$ type. In **Figure 5.1(b)** the inset arrows indicate $s_h \rightarrow p_h$ IR optical transitions for each model.

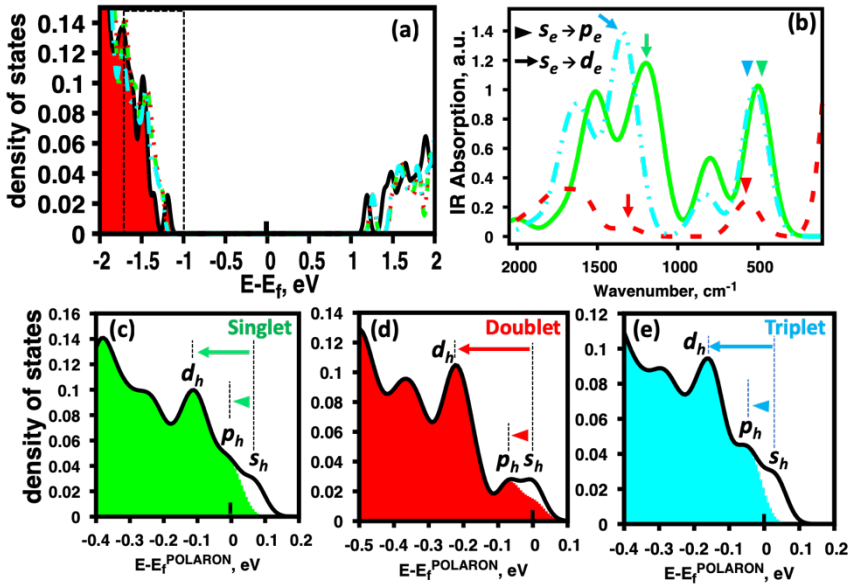

Figure 5.1: DOS and IR polaron absorption spectra for the positive polaron models. **(a)** DOS, aligned with the Fermi level of the neutral model, of four respective models: neutral perovskite NC (black, solid), positive polaron in singlet configuration (green, dashed), in doublet configuration (red, dash-dot), and triplet configuration (blue, dot-dash-dot dot). The boxed region is to highlight that we focus on the valence band DOS to observe positive polaron formation. **(b)** IR absorption spectra spectra for the positive polaron plotted in units of wavenumbers for singlet (green, solid), doublet (red, dashed), and triplet (blue, dot-dot-dash) spin configurations. The inset triangles/arrows indicate $s_h \rightarrow p_h$ and $s_h \rightarrow d_h$ optical transitions which are illustrated in **(c)-(e)**. DOS for the **(c)** singlet, **(d)** doublet, and **(e)** triplet polaron model. The energy axis is aligned to the Fermi level of the polaron. Shaded regions correspond to occupied states while white regions correspond to unoccupied states which we call the positive polaron. The s_h, p_h, d_h labels indicate symmetry of the envelope function for those respective bands. For **(c)** and **(e)** the lowest energy optical transition is of $s_h \rightarrow p_h$ type while **(d)** is $s_h \rightarrow s_h$ type due to each band being two-fold degenerate.

In **Figure 5.2(a)-(e)** we show the DOS and IR absorption spectra for negative polaron models which has the same format as **Figure 5.1(a)-(e)**. **Figure 5.2(a)** shows the DOS of the ground-state model (black) singlet (green, dashed), doublet (red, dashed), and triplet (blue, dot-dashed) negative polarons with the Fermi energy being aligned with the neutral ground-state model. The boxed region of the valence band corresponds to the location of the negative

polarons in the DOS. **Figure 5.2(b)** shows the IR absorption spectra for singlet (green, solid), doublet (red, dashed), and triplet (blue, dot-dashed) polaron models. It is observed that the singlet and the triplet lowest energy transition are of high intensity compared to the doublet. It is also observed that **Figure 5.2(b)** the negative polaron spectra is of higher intensity than **Figure 5.1(b)** the positive polaron spectra. **Figure 5.2(c)-(e)** shows the negative polaron DOS for the **(c)** singlet, **(d)** doublet, and **(e)** triplet model with the energy axis being aligned to the polaron Fermi level for each respective model. Filled in regions of **Figure 5.2(c)-(e)** correspond of occupied states, which we refer to as the negative polaron, and white regions being unoccupied hole states. The s_e, p_e, d_e labels indicate symmetry of the envelope function for those respective bands. The alignment of polaron Fermi levels in **Figures 5.2(c)-(e)** follows the same trends as **Figure 5.1(c)-(e)**. This again means that the lowest energy optical transition for **Figures 5.2(c)** and **(e)** are $s_h \rightarrow p_h$ types of transitions while **(d)** is of $s_h \rightarrow s_h$ type. In **Figure 5.2(b)** the inset arrows indicate $s_h \rightarrow p_h$ IR optical transitions for each model.

The PGS optimized geometry is expected to be different than the neutral QD ground state geometry due to static coupling of electronic and nuclear degrees of freedom. In **Figure 5.3(a)-(f)** we quantify the difference between geometries by plotting RDFs,. RDFs compare pair-wise distances between ions and serves as a measure of changes in geometry due to polaron formation. **Figure 5.3(a),(c),(e)** show RDFs for positive polarons and **(b),(d),(f)** for negative polarons with **(a)-(b)** comparing Pb-Br and Br-Br distances labeled with peaks **A/A'** and **B/B'** **(c)-(d)** comparing Cs-Br distances labeled with peaks **C/C'** and **(e)-(f)** comparing Cs-Pb pair-wise distances labeled with peaks **D/D'** and **E/E'**. For each plot in **Figure 5.3(a)-(f)** the RDF is plotted for the optimized, neutral ground state (black, solid), singlet (green, dash-dash), doublet (red, dot-dot), and triplet (blue, dot-dash) spin configuration for the optimized polaron

geometries. Increases(decreases) in peaks of the RDF between the neutral ground state and PGS can be associated with increases(decreases) in coordination number of ions[110] due to polaron formation. Shifts in RDF peaks along the x-axis would correspond to average bond/coordination elongation or contraction. Numerical values of the peaks labeled in **Figures 5.3(a)-(f)** are shown in **Table 5.1**.

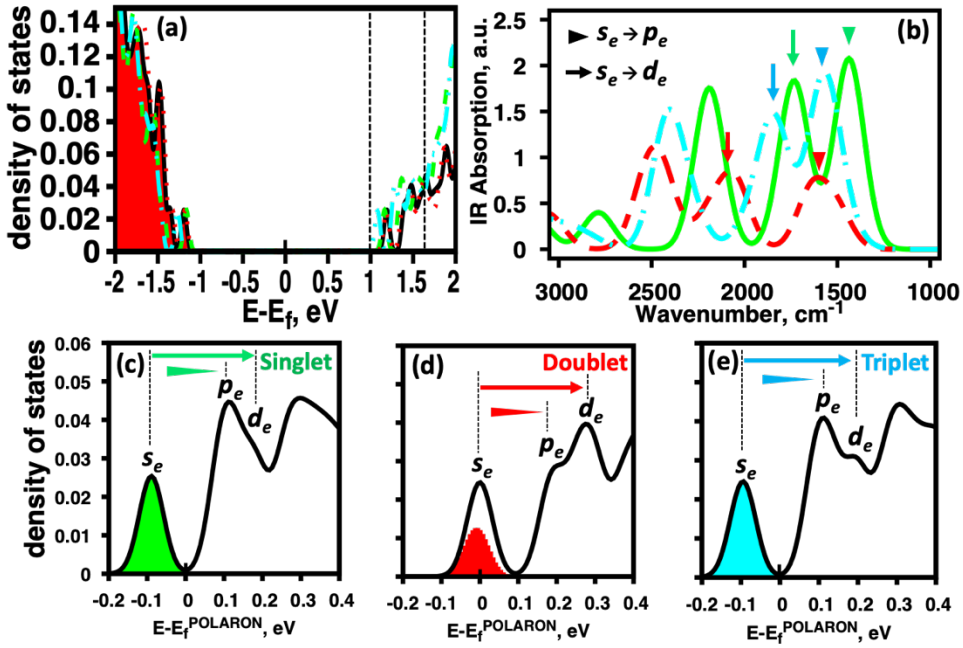

Figure 5.2: DOS and IR polaron absorption spectra for the negative polaron models. **(a)** DOS, aligned with the Fermi level of the neural model, for the four respective models: neutral perovskite NC (black, solid), positive polaron in singlet configuration (green, dashed), in doublet configuration (red, dash-dot), and triplet configuration (blue, dot-dash-dot dot). The boxed region is to highlight that we focus on the conduction band DOS to observe negative polaron formation. **(b)** IR absorption spectra, spectra for the negative polaron, in units of wavenumbers, for singlet (green, solid), doublet (red, dashed), and triplet (blue, dot-dot-dash) spin configurations. The inset triangles/arrows indicate $s_e \rightarrow p_e$ and $s_e \rightarrow d_e$ optical transitions which are illustrated in **(c)-(e)**. DOS for the **(c)** singlet, **(d)** doublet, and **(e)** triplet polaron model. The energy axis is aligned to the Fermi level of the polaron. Shaded regions correspond to occupied states while white regions correspond to unoccupied states. The occupied states are what we refer to as the negative polaron. The s_e, p_e, d_e labels indicate symmetry of the envelope function for those respective bands. For **(c)** and **(e)** the lowest energy optical transition is a $s_e \rightarrow p_e$ type while **(d)** is $s_e \rightarrow s_e$ type due to each band being two-fold degenerate.

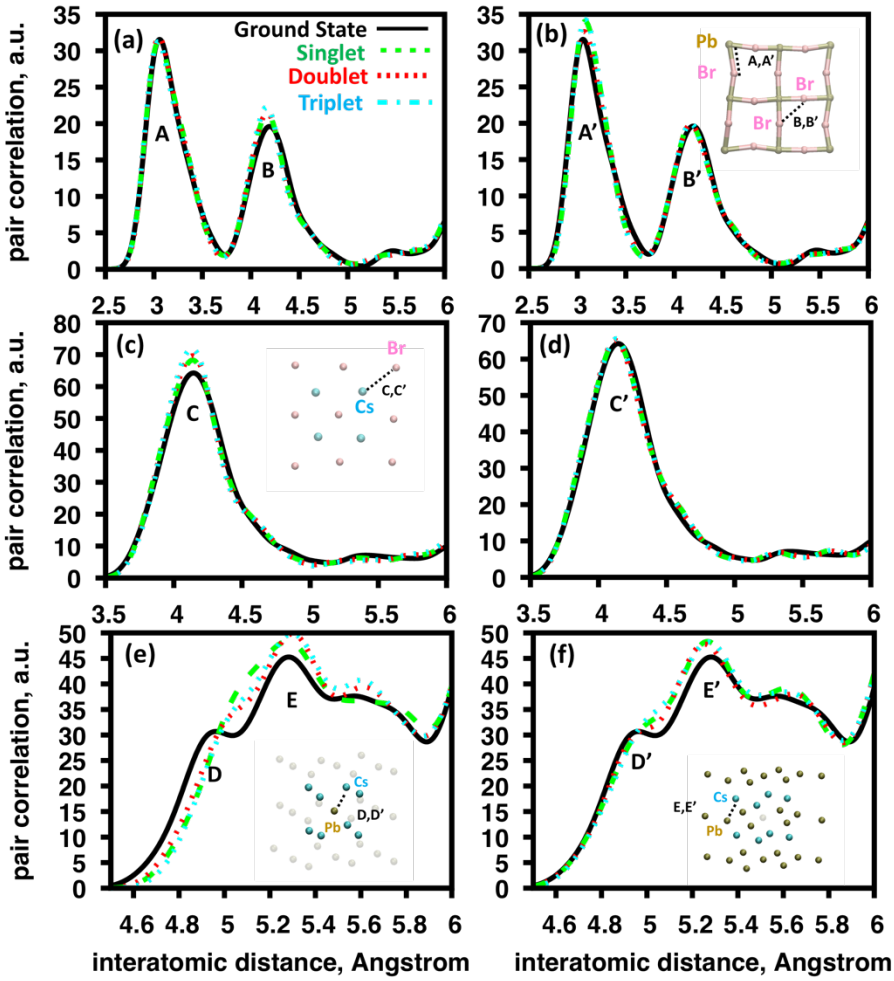

Figure 5.3: Distributions of pair-wise distances between (a)-(b) Pb-Br signified with the A/A' peak and Br-Br distance represented with B/B', (c)-(d) Cs-Br represented with peak labels C/C', and (e)-(f) Cs-Pb ions represented with peak labels D/D' and E/E'. (a), (c),(e) are RDFs for positive polarons and (b),(d),(f) for negative polarons. For all plots, RDF is plotted for the optimized, neutral ground state (black, solid), singlet (green, long-dash), doublet (red, short-dash), and triplet (blue, dot-dash-dot-dot) spin configuration for the optimized polaron geometries. Insets for (b), (c), (e), (f) illustrate the bond distances that are being computed for the labeled peaks. We note that peaks D/D' indicate distances between the interior Pb2+ ion and Cs+ ions while the E/E' peaks are between surface Pb^{2+} ions and Cs+ ions.

Comparing Pb-Br and Br-Br bond distances in **Figure 5.3(a)** positive polaron and **(b)** negative polaron RDF to the NGS it is observed that **(a)** shows an increase in the feature B along with bond contraction while **(b)** shows an increase in feature A' with a bond elongation. This indicates that the positive polaron increases coordination between Br ions while the negative polaron increases coordination between Pb-Br ions. When considering that the conduction

(valence) band edges are composed of Pb^{2+} *6p* (Br^{-} *4p*) states the addition (removal) of charge is reducing (oxidizing) the system. For the negative polaron model this would imply that the oxidation state will fractionally change to $Pb^{(2-\delta)+}$ which will decrease the electrostatic attraction between Pb and Br ions resulting in an elongated bond length (feature A' in **Figure 5.3(b)**). We note the same trend in Pb-Br bond elongation has been observed elsewhere for $CsPbBr_3$ atomistic models[66 111]. For the positive polaron, an electron is being removed from the valence band edge which fractionally decreases the electronegativity $Br^{(1-\delta)-}$. This would decrease the electrostatic repulsion between nearest neighbor Br ions and decrease the coordination distance between them (feature B in **Figure 5.3(a)**). Decreased Br-Br coordination also suggests that under oxidation the octahedral Pb-Br lattice undergoes greater tilting and reduces the connectivity between adjacent octahedra.

Cs-Br bond distances only show significant changes for the **Figure 5.3(c)** positive polaron formation while **(d)** negative polaron formation shows negligible change in RDF. **Figure 5.3(c)** peak **C** shows an increase in coordination between Cs and Br ions and elongation of pair-wise distances. Again due to positive polaron formation the Br ions will have a decreased electronegativity $Br^{(1-\delta)-}$ and have a decreased Coulombic attraction to positive Cs^{+} ions. This would account for the decrease in pair-wise distances.

Coordination between Cs-Pb ions shown in **Figure 5.3(e)-(f)** show two peaks. The **D/D'** peaks are attributed to coordination of Cs^{+} to the interior Pb^{2+} ion (center of the 2x2x2 unit cell structure) and the **E/E'** peaks are attributed to coordination of Cs^{+} to exterior surface Pb^{2+} ions. Comparing the neutral ground state and polaron RDF for the **D/D'** peaks it is observed that the peak broadens and no longer have a well-defined maximum while the **E/E'** peaks increase. This implies that the Cs^{+} ions expand away from the center of the core towards the surface Pb^{2+} ions.

5.3.2. Hot-Polaron Cooling and IR Photoluminescence

The rates of these state-to-state transitions are illustrated in **Figure 5.4(a)-(b)** in the form of Redfield tensors R_{iijj} for the positive polaron in **(a)** and the negative polaron in **(b)**. The 'Orbital i' and 'Orbital j' axis represent states in the **(a)** conduction band and **(b)** valence and are labeled with the symmetry of their envelope function. The R_{iijj} axis represents the nonradiative state-to-state transition rate in units of ps^{-1}. These rates are used to compute dynamic non-radiative cooling rates $k_{cooling}$ and non-radiative recombination rates k_{nr}. Note that only off diagonal tensor elements are non-zero while all diagonal elements are zero. For **Figure 5.4(a)-(b)** it is observed that there are alternating high intensity transitions near the main diagonal and numerous low intensity transitions away from the main diagonal. The altering high intensity transitions $R_{ii,i-1,i-1}(i) \approx R_0\,(\delta_{i+1,j} + \delta_{i,j+1})\frac{1+(-1)^i}{2}$ are between near-degenerate states whose average band energies only deviate by a few meV while the low intensity transitions are between bands whose average energy is within thermal energy kT. It is also observed that for **Figure 5.4(b)** the negative polaron transitions rates are very low near the conduction band edge within the orbital range [LU,LU+12].

The initial condition for the dynamics simulation are interpreted as the following: the timescale of nuclear reorganization (i.e. polaron formation) $\tau_{reorganziation}$ is much faster than the timescale of the charge-carrier dissipating it's excess energy to the lattice as phonons $\tau_{dissipation}$. In other words, the excited-state trajectory corresponds to a hot-polaron within the self-trapped Coulomb potential well which dissipates energy to the surrounding heat bath. This results in hot-polaron cooling from the initial condition to the RES. We then compute the rate of hot-polaron cooling from the initial condition to the RES as a function of dissipation energy

$E_{diss} = E_{IC} - E_{RES}$ where E_{IC} is the energy of the initially occupied hot-polaronic state and E_{RES} is the energy of the relaxed-excited state.

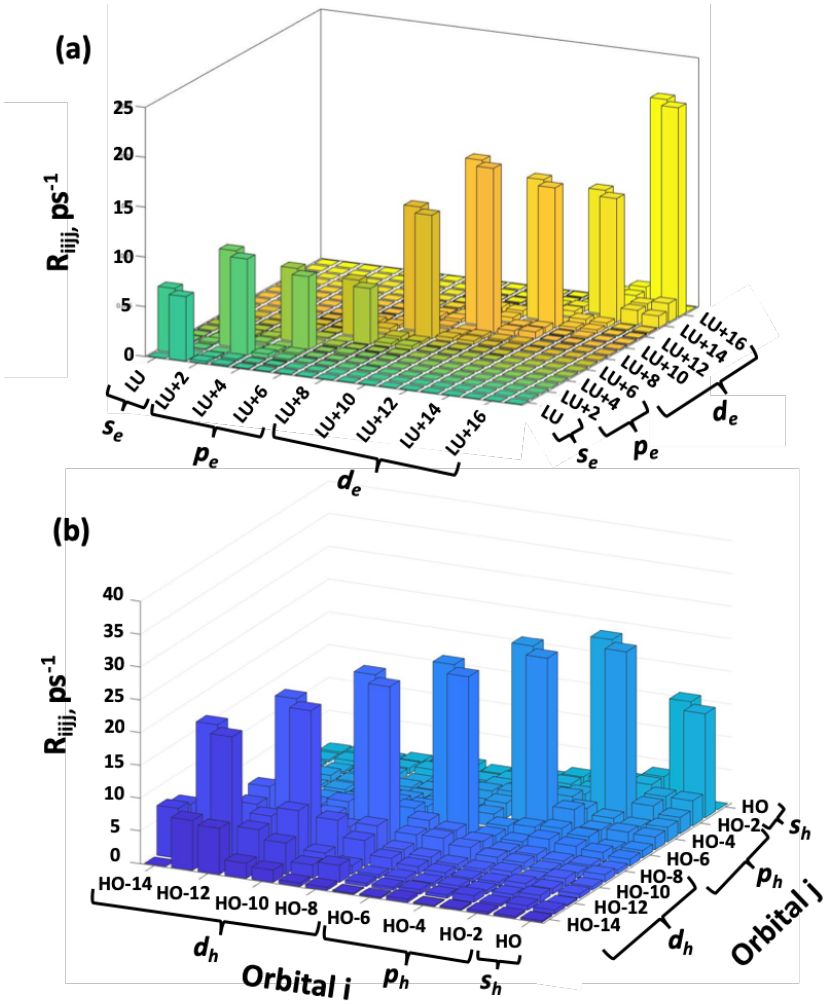

Figure 5.4: Redfield tensor (a) negative singlet polaron and (b) positive singlet polaron. The 'Orbital i' and 'Orbital j' axis represent states in the (a) conduction band containing symmetry states s_e $[LU, LU+1]$, p_e $[LU+2, LU+7]$ and d_e $[LU+8, LU+17]$ (b) valence band with envelope symmetry states s_h $[HO, HO-1]$, p_h $[HO-2, LU-7]$, d_h $[LU-8, LU-14]$. The R_{iijj} axis represents the nonradiative state-to-state transition rate in units of ps^{-1}. These rates are used to compute hot-carrier non-radiative cooling rates based on initial population conditions. It is observed that there are alternating high intensity transitions near the main diagonal and numerous low intensity transitions away from the main diagonal. The high intensity transitions are between near-degenerate states whose average band energies along the MD trajectory only deviate by a few meV, while the low intensity transitions are between bands whose average energy is within thermal energy kT. Note that (b) the positive polaron model has higher intensity off-diagonal elements than (a) the negative polaron model. This indicates that the positive polaron has greater coupling to nuclear vibrionic degrees of freedom.

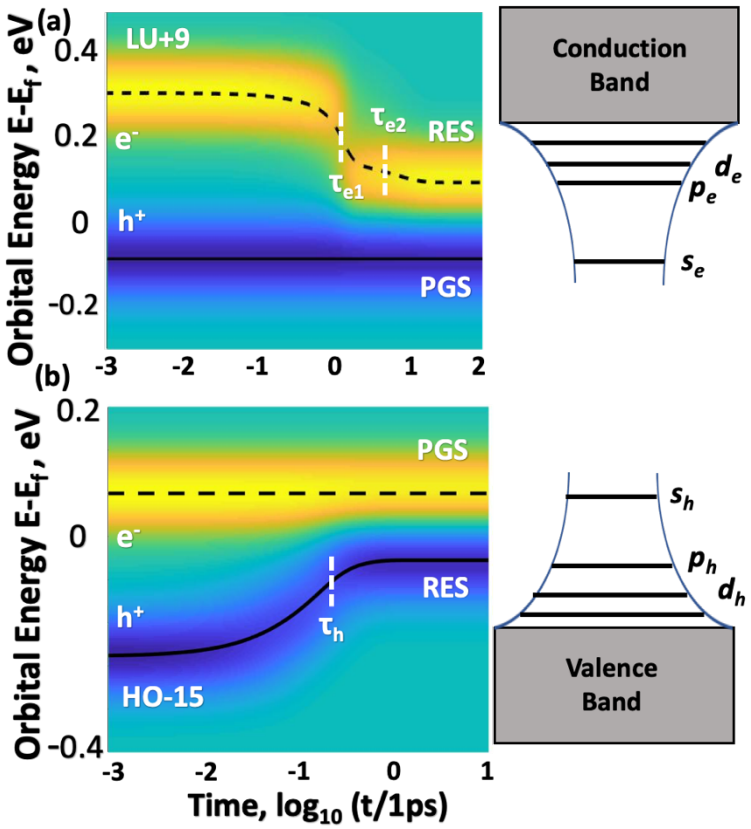

Figure 5.5: Hot-carrier cooling dynamics for (a) negative polaron and (b) positive polaron. The energy axis is in reference to the Fermi level for each polaron with the time axis in log scale normalized to 1ps. Green represents background reference, yellow represents average occupation of charge density in conduction band, and blue represents average occupation of charge density in valence band. Horizontal dotted/solid lines represent energy expectation values of charge carriers, and vertical dashed lines represent hot carrier cooling times $\tau_{cooling}$ fit to a single exponential decay. The initial condition corresponds to a polaron with excess kinetic energy in the polaron potential well then cools to the polaron RES (p_h/p_e). For (a) the carrier decay follows a bi-exponential decay while for (b) it is observed that the cooling follows closely to mono-exponential decay. The bi-exponential decay is attributed to large sub-gaps, low density of states, and polaron screening of phonons which reduces NAC.

Figure 5.5(a)-(b) shows hot-carrier cooling along the excited-state trajectory **(a)** for negative polaron model and **(b)** positive polaron model from a non-equilibrium state to the polaron RES. The energy axis is in reference to the Fermi level of the polaron model with the time axis in log scale normalized to 1ps. Green color code represents background reference charge density, yellow represents average occupation of charge density distribution in conduction band $\Delta n > 0$, and blue represents average occupation of charge density distribution

in valence band $\Delta n < 0$. Horizontal dotted/solid lines represent energy expectation values of charge carriers. For the negative polaron in **Figure 5.5(a)** it is observed that the hot-carrier shows a bi-exponential decay. The 'fast' component has a lifetime around $\tau_{e_1} \approx 1$ ps and the slow component has a lifetime on the order of $\tau_{e_1} \approx 10$ ps. For the positive polaron in **Figure 5.5(b)** it is observed that hot-carrier cooling follows closely to a single exponential decay with sub-picosecond carrier cooling $\tau_h < 1$ps. In **Figure 5.6** we compare the cooling time of positive (red, large circle) and negative (green, small circle) hot-polarons cooling time to positive (black, small dot) and negative (blue, small dot) free-carriers as a function dissipation energy E_{diss}. It is observed that it takes longer for the hot-polarons to dissipate their energy to the surrounding heat bath than if they where free-carriers. This is attributed to the polaronic geometries resulting in screening which reduce non-adiabatic coupling between electronic states.

A competing mechanism for nonradiative electronic energy dissipation through phonons is dissipation in the form of photons. A 'hot' carrier can dissipative energy in the form of IR photons before relaxing to the RES giving IR PL. This is what we plot in **Figure 5.7(a)-(d).** **Figure 5.7(a)-(b)** show the **(a)** time resolved and **(b)** time-integrated emission for the negative polaron along the excited-state trajectory. **Figure 5.7(c)-(d)** shows the same plots but for the positive polaron. In **Figure 5.7 (a)** and **(c)** the time axis is in log scale normalized to 1 ps. The electronic excited-state trajectories where propagated for **(a)-(b)** 5 ps and **(c)-(d)** 500ps in accordance to the non-radiative recombination rates, as seen in **Table 5.2**. The blue background represents the 'dark' reference states with colored regions indicating occupation of optically 'bright' states with a population inversion and PL. Yellow represents the most intense optical transitions along the excited-state trajectory. **Figure 5.7 (b)** and **(d)** show the time integrated PL spectrum.

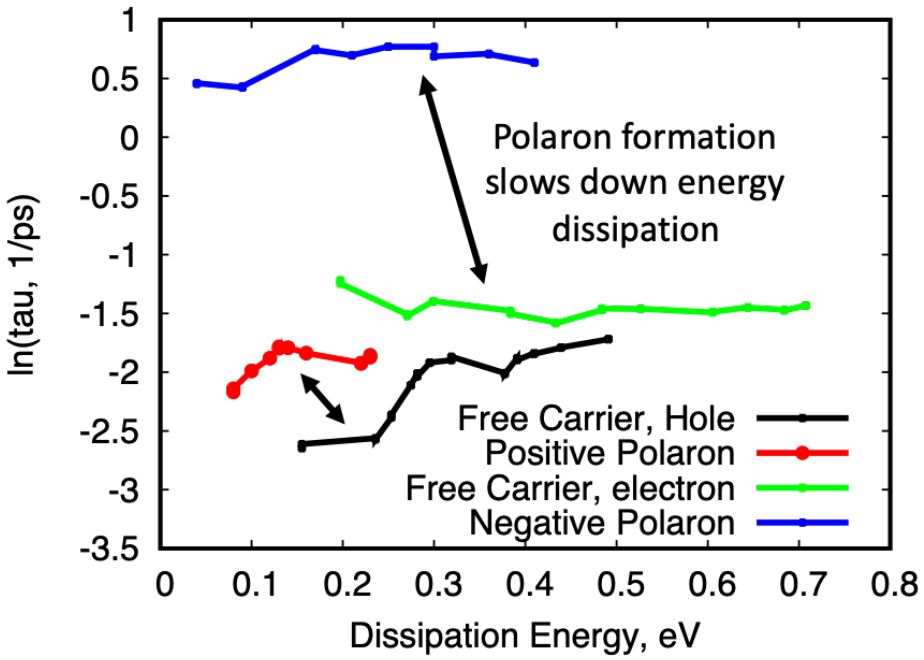

Figure 5.6: Comparison of the natural log of cooling time ln ($\tau_{cooling}$) for positive (red, large circle) and negative (green, small circle) hot-polarons to positive (black, small dot) and negative (blue, small dot) free-carriers as a function dissipation energy E_{diss}. Hot carrier cooling τcooling is found from fitting the hot-carrier energy decay to a single exponential decay. Comparing the hot-polaron cooling to the hot free-carriers it is observed that the negative hot-polaron cooling is significantly longer than the free-carrier cooling while the positive hot-polaron cooling is only slightly longer than the free-carrier cooling.

For both **Figure 5.7 (a)** and **(c)** it is observed that there is a cascade of 'hot' emission events before cooling to the polaron RES. Once the hot-carriers cool to the RES there is polaron PL from the RES to the PES arising from $p_e \rightarrow s_e$ and $p_h \rightarrow s_h$ transitions, respectively. From comparing **(b)** the negative polaron and **(d)** the positive polaron it is observed that that **(b)** has 1.5 order of magnitude larger intensity than **(d).** It is also noted that there is a weak $d_h \rightarrow s_h$ hot PL observed in **(d)**.

To determine the efficiency of IR PL from the positive and negative polaron we compute PLQY from k_r and k_{nr}. k_r is computed from oscillator strengths using the Einstein coefficient for spontaneous emission, and k_{nr} is found from the corresponding Redfield tensor element $R_{RES-PGS}$. **Table 5.2** shows k_r, k_{nr}, and PLQY for models presented here. It is observed that the

negative polaronic models show higher PLQYs than the positive polaron models with the negative singlet showing the highest computed PLQY on the order of 10^{-4}.

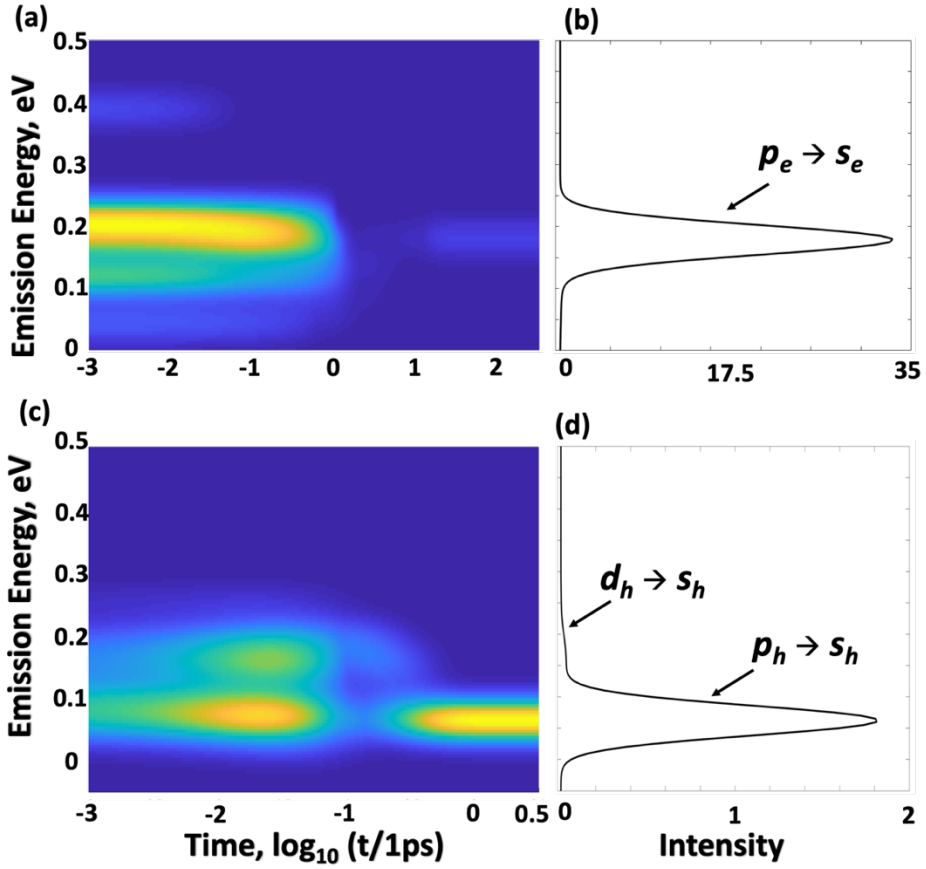

Figure 5.7: Radiative relaxation along the excited-state trajectory with (a),(c) showing time-resolved emission and (b),(d) showing time-integrated radiative emission for the (a)-(b) negative polaron and (c)-(d) positive polaron. The dynamics at this figure corresponds to the same initial conditions as Figure 5.5. Before cooling to the polaron RES hot carriers can emit IR photons to dissipate energy which competes with non-radiative transitions. Once cooled to the RES the polaron emits to the PGS. The trajectories where propagated for (a) 5 ps and (c) 500ps in accordance to the non-radiative recombination rates. In (a) and (c) the blue background represents optically 'dark' states with colored regions indicating occupation of optically 'bright' states with a population inversion. Yellow represents the most intense optical transitions along the excited-state trajectory. (b) and (d) sum the optical transitions along the trajectory, by. For both models it is observed that there is cascading hot carrier emission before decaying to the RES giving polaron PL. Once cooled to the RES both models show $p_x \rightarrow s_x$(x=e,h) transitions giving rise to IR PL which is greater in intensity than the hot carrier emission. It is observed that (b) the negative polaron has 1.5 orders of magnitude greater intensity than (d) the positive polaron. This is attributed to extended non-radiative lifetime of the negative polaron model, see Table 5.1.

Table 5.1: Table is showing oscillator strength f_{ij}, radiative recombination rate k_r non-radiative recombination rate k_{nr}, resultant PLQYs for each model studies, and the logarithm of each PLQY. The negative singlet polaron shows 2 to 4 orders of magnitude greater PLQY than the other models with both the negative polaron models showing higher PLQY than the positive polaron models. This is attributed to the negative polaron models showing an order of magnitude faster k_r and the negative singlet having a 2 orders of magnitude reduced k_{nr}.

Model	f_{ij}	k_r[1/ns]	k_{nr}[1/ns]	PLQY	log (PLQY)
Positive-Singlet	0.14	$2.81\text{x}10^{-4}$	$2.08\text{x}10^{3}$	$1.35\text{x}10^{-7}$	-7
Positive-Doublet	0.07	$1.95\text{x}10^{-4}$	$6.30\text{x}10^{3}$	$3.09\text{x}10^{-8}$	-8
Negative-Singlet	0.29	$5.10\text{x}10^{-3}$	$1.64\text{x}10^{1}$	$3.11\text{x}10^{-4}$	-4
Negative-Triplet	0.30	$5.38\text{x}10^{-3}$	$4.34\text{x}10^{3}$	$1.24\text{x}10^{-6}$	-6

5.4. Discussion

The main observable of interest in this paper is the spectral properties of individual polarons in a $CsPbBr_3$ perovskite NC model. We also investigate the structural reorganization of the lattice due to static electron-phonon interactions and the emissive properties of the positive and negative polarons. Within the discussion section we expand on the following topics: correspondence between atomistic based modeling of polarons and relation of the excited-state dynamics of hot-carrier cooling simulations to experimental findings, the role of surface ligands on the excited-state dynamics, and comments on the assumptions and approximations of our methodology.

In our excited-state dynamics for a $CsPbBr_3$ NC we modeled the hot-carrier cooling of polarons with excess energy within the polaron potential well to the RES. This assumes that upon photo-excitation/charge injection that nuclear reorganization (static electron-phonon

interaction) is much faster than energy dissipation (dynamical electron-phonon interaction), $\tau_{cool} \ll \tau_{reorganziationreorg}$. A recent transient absorption study seems to suggest that some varieties of $APbX_3$ perovskites are capable of forming hot-polaronic states. In a bulk crystal of the fully inorganic $CsPbBr_3$ it was observed that carrier cooling τ_{cool} occurs faster than polaron formation $\tau_{reorganziationreorg}$ while for $MAPbBr_3$ carrier cooling and polaron formation occur on the same timescale[64]. This suggests that cation engineering of the perovskite can possible to prepare a hot-polaronic state before the carrier dissipates all of its excess energy to the lattice. Another parameter which may impact the relative timescales of τ_{cool} and $\tau_{reorganziationreorg}$ is the degree of quantum confinement within a nanostructure. Increasing confinement leads to sparse electronic states with large sub-gaps between states. Heuristically, increased confinement should slow down τ_{cool} and make $\tau_{reorganziationreorg}$ more competitive, allowing for more efficient hot-polaron formation.

The negative polaron models show enhanced (2-4 orders of magnitude) PLQY compared to the positive polaron models. This can be attributed to the combination of the negative polarons model showing slightly faster radiative recombination rates and slower non-radiative recombination rates, observed from **Table 5.1**. The faster radiative recombination rates of negative polarons can be attributed to the larger oscillator strengths and slightly larger transition energies. This explains the 0.5 order of magnitude difference between the negative and positive polarons radiative recombination rates. The difference in non-radiative rates requires more in-depth analysis.

To understand why the negative singlet polaron shows 2 orders of magnitude slower nonradiative recombination rate than the other models we utilize vibrational modes analysis. According to the bi-linear electron-phonon interaction non-radiative relaxation of charge carriers

requires a resonance between frequency of nuclear vibrational modes and energies of electronic transitions $\omega^{vib} \approx \epsilon_i - \epsilon_j$. To approximate the vibrational energy spectrum provided by the passivation ligands we implement normal mode analysis on a 2-D film $Cs_8Pb_{12}Br_{32}$ passivated by the same ligands used for the NC model. The 2-D film was used since normal mode analysis for the full NC model was found to be prohibitively expensive in numerical resources.

Figure 5.8(a)-(c) compares **(a)** the vibrational modes to the IR spectra of the **(b)** negative polaron models and **(c)** positive polaron models. It is seen that for **(c)** the positive polaron model the lowest energy optical transitions fall in resonance with normal modes in the range of [1500, 500cm^{-1}] while for **(b)** the negative polaron model has a 'mismatch' between radiative transitions energies and vibrational transition energies within the range of [2500,1750cm^{-1}]. But curiously the lowest energy optical transitions observed for **(b)** the singlet (green, solid) and triplet (blue, dash-dot-dot) negative polaron show to be in resonance with two peaks in **(a)** between [1750,1450cm^{-1}]. The peak in **(a)** at 1450 cm^{-1} we attribute to N-H bending modes of the ethylammonium cations while the peak around 1600 cm^{-1} we attribute to C=O stretching modes of the acetate anions. From previous work[105] we have shown that for this specific surface chemistry only the acetate anions contribute electronic density to the surface of the NC (chemisorbed) while the ethylammonium cations are bound to the surface due to electrostatic attraction (physisorbed). This implies that the N-H vibrational modes do not contribute significantly to non-radiative recombination rates while the C=O stretching modes will. This is due to non-adiabatic coupling being proportional to the orbital overlap between Pb^{2+} or Br^- ions at the surface and the COO^- or NH_3^+ functional groups of the passivation ligands. We also note that the C=O mode is in resonance with the lowest energy optical transition for the negative triplet model and off-resonance of the negative singlet model. This is likely the source of the 2

orders of magnitude difference between their respective non-radiative recombination rates, as observed in **Table 5.1.**

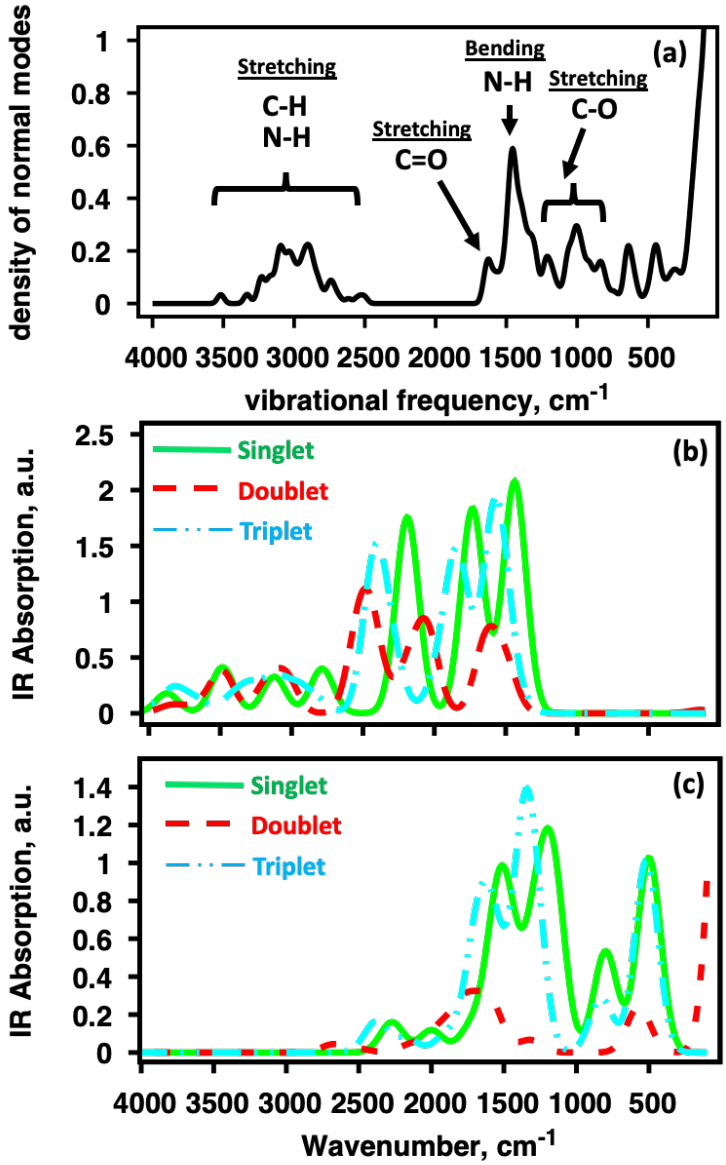

Figure 5.8: Comparing **(a)** the normal modes of vibration of a ligand terminated perovskite surface $Cs_8Pb_{12}Br_{32}$ to the IR absorption spectra of the **(b)** negative polaron models and **(c)** positive polaron models. It is observed that in the range [2000,2500] cm^{-1} there is a mismatch between the vibrational modes provided by **(a)** the surface ligands and **(b)** energy of transitions between polaron states. For **(c)** the positive polaron it is seen that there are vibrational modes in resonance with transitions between polaronic states.

5.5. Conclusion

Lead-halide perovskites have shown to be a promising material for next-generation light emitting devices due to tune-able emission across the visible spectrum. They have also shown efficient application to photovoltaic devices in part due to the extended non-radiative lifetimes of photo-induced charges carriers, which has been attributed to large polaron formation producing simultaneous positive and negative polarons. Large polarons, quasiparticles which form in lead-halide perovskites due to their 'soft' ionic lattice, are expected to show two contrasting absorption mechanisms: dipole-allowed transitions within the bound polaron potential well and photoionization of the bound polaron into the conduction/valence band. Photo-excitations within the polaron potential well produces an excited 'hot-polaron' which can dissipate energy by using radiative or non-radiative relaxation mechanisms. We hypothesize that hot-polarons in perovskites have the ability to emit electromagnetic radiation in the IR range due to (i) inverse occupation within the potential well (ii) bright electronic transitions within the polaron potential well. To test this, we implement mixed quantum-classical methodologies to model photo-physical features of individual positive and negative polarons, with various spin multiplicities, in an atomistic $CsPbBr_3$ nanocrystal model fully-passivated with organic ligands.

For the impact of polaron formation on the lead halide perovskite lattice, we found that positive and negative polarons show contrasting patterns for the Pb-Br and Br-Br ion pairs. Specifically, the positive polaron increases coordination number and decreases distances between Br-Br atoms while the negative polaron increased coordination number and decreased bond distances between Pb-Br. This is rationalized in terms of oxidation (reduction) and reduced (increased) electronegativity due to positive (negative) polaron formation.

For spectral features, we implement two approach's: absorption spectra of individual polarons in the IOA and PL properties of individual polarons by implementing excited-state dynamics in density matrix formalism which couple electronic and nuclear degrees of freedom. Interestingly, polaronic states involve frontier orbitals which exhibit certain spatial symmetry and patterns of electronic energy spacing compared to hydrogenic models. Thus we use analyze electronic transitions in terms of spatial symmetry $s_{h/e}$, $p_{h/e}$, and $d_{h/e}$, where h refers positive polarons (holes) and e refers to negative polarons (electrons). It has been found that the spin multiplicity of the polaronic state drastically effect the observed optoelectronic properties. Specifically, the singlet and triplet multiplicities for both the positive and negative polaron models show bright lowest energy absorption transitions and PL which we ascribe to $s_{h/e} \rightarrow p_{h/e}$ types of transitions. The doublet configuration shows 4x-5x reduced absorption intensities compared to the respective singlet or triplet multiplicity and vanishing PL due to its lowest energy transition being of $s_{h/e} \rightarrow s_{h/e}$ character.

The polaron models show low PLQY (10^{-4} – 10^{-8}) due to the large difference in timescales of radiative recombination (1-10us) and non-radiative recombination (10ns-1ps). To explain the wide range of non-radiative recombination rates we implement normal mode analysis where vibrations are provided from the inorganic $CsPbBr_3$ lattice and from organic-inorganic interaction at the NC surface. We find that the system with the slowest non-radiative recombination rate (negative, singlet) there are a lack of *active* normal modes in resonance with the lowest energy transition from the polaron RES to the PGS. While in contrast, the models which displayed fast non-radiative recombination had active normal modes in resonance with their lowest energy optical transition. Specifically, the acetate anions contribute electronic density to the surface of the NC (chemisorbed) while the ethylammonium cations are bound to

the surface due to electrostatic attraction (physisorbed). This implies that the N-H modes are *spectator* modes do not contribute to significantly to the non-radiative recombination rates while the C=O stretching modes are *active*. The hypothesis of large polaron emission is partially supported by the atomistic simulations.

6. ROLE OF SURFACE DEFECTS ON RADIATIVE RELAXATION: BRIGHT POLARON-INDUCED SURFACE TRAP PHOTOLUMINESCENCE

6.1. Introduction

$APbX_3$ (A=Cs,CH_3NH_3: X=I, Br, Cl) lead halide perovskites (LHPs) have become popular materials for a variety of opto-electronic technology applications due to their facile wet-chemical synthesis, tunable chemical composition, and size-dependent photo-physical properties. Their versatile and unique electronic properties are largely attributable to their tolerance of crystallographic and surface defects. Traditional semiconductors, such as silicon, show dramatic drops in quantum yields with the introduction of defects due to the formation of deep trap states where the energy of charge-carriers are transferred to lattice phonons through non-radiative recombination. LHPs show high efficiencies despite considerable defect densities. Initially, this trend was rationalized in terms of the unique chemical bonding of the Pb-X inorganic network which shows resistance towards deep trap state formation[69, 112]. Polarons, quasi-particles that form due to static electron-phonon interactions[100, 113-114], have also been used to explain the unusually long non-radiative lifetime of charge-carriers in bulk films[28, 66] and their photoluminescence characteristics[103-104]. Associated with polarons are low-frequency phonon modes which have also been used to rationalize the defect tolerance of LHPs[115].

LHP NCs[29] also show remarkable defect tolerance for both lattice defects and surface point (vacancy) defects. From *ab Initio* atomistic simulations, this has been attributed to point defects having fairly large defect formation energies and the energies of electronic states associated with the defects having energies aligning within the conduction/valence band or forming shallow defect states inside the bandgap[116]. TD-DFT has been used to investigate role of vacancy defects on the optical absorption properties of a $CsPbBr_3$ NC finding that they are robust

to defects, aside from Br vacancies that introduce trap states which reduce the oscillator strengths and provider lower transition energies compared to the pristine NC[117]. These defect tolerances makes LHP NCs attractive for commercial luminescence applications, such as LEDs [118 119].

Atomistic *ab Initio* simulations have shown to be useful in describing ground-state electronic structure[120-121], polaronic characteristics[111, 122], and non-radiative dynamics of charge-carriers without[73, 105, 123] and in the presence of defects[124] in LHPs. Less attention has been paid to the vacancy defects under photo-excited and thermal (dynamic) conditions. Under practical operating conditions for opto-electronic applications LHP NCs will spend a considerable amount of time in the photo-excited state and explore the excited-state potential energy surface (ES-PES). When vacancy defects are present their energy levels, which remain 'hidden' in the conduction/valence band in the ground-state, may become stabilized and lower their energy due to polaron occupations (ie reorganization energy). Photo-excitation can also potentially catalyze the formation of surface vacancies (ie photo-thermal degradation). This is particularly relevant for LHP NCs where the surfaces are primarily terminated by cation-anion pairs, some of which are conjugate acid-base pairs[125], and photo-excitation can act as a catalyst for surface reactions which result in ligand desorption. These considerations will have a direct impact on the description of the photo-physical properties of LHP NCs, such as photoluminescence quantum yields (PLQYs), as illustrated in **Figure 6.1**. In summary, the role of polaronic occupations in the presence of surface defect sites and the subsequent impact on excited-state dynamics is relatively unexplored. It would be predicted that if polaronic reorganization of energy band alignments resulted in mid-gap trap states that they would be detrimental to photoluminescence efficiencies.

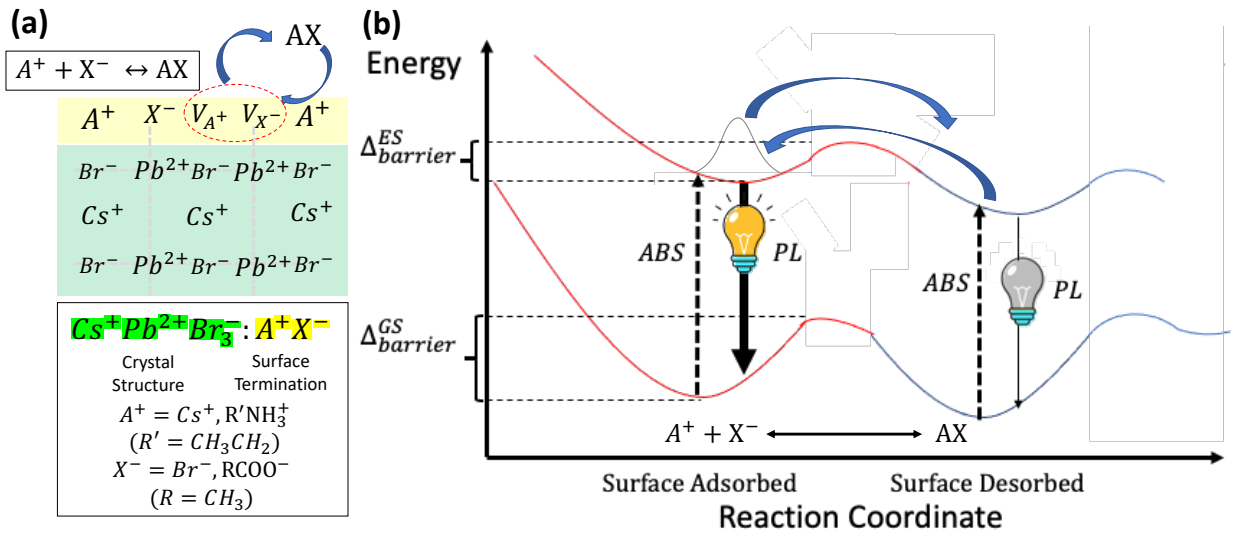

Figure 6.1: Description of the surface chemistry for $CsPbBr_3$ and the equilibrium that exists between atomic/molecular species that are adsorbed/desorbed from the surface. **(a)** Diagram illustrating the (100) surface termination of $CsPbBr_3$ resulting in cation A^+ and anion X^- surface ligands adsorbed to surface $Pb^{2+}$and Br^-. For each pair of $A^+$and X^- there exists an equilibrium between their surface adsorbed state and surface desorbed state: $A^+Br^- + Pb^{2+}\ X^- \leftrightarrow V_{A^+}\ Br^- + Pb^{2+}V_{X^-} + AX$. For opto-electronic applications it is preferable to have the equilibrium biased towards the surface adsorbed configuration to prevent surface trap-state formation. **(b)** For opto-electronic applications, $CsPbBr_3$ nanocrystals are photo-excited and explore the excited-state potential energy surface (PES). A diagram of the PESs are shown in **(b)**. In the adsorbed configuration it is expected that the nanocrystal will have bright photoluminescence while in the desorbed configuration the photoluminescence will become dark.

In this work we use *ab Initio* methodology to study the interplay between electronic configuration (GS and L-ES), surface chemistries, and thermal motion of nuclei in the description of a LHP NC opto-electronic properties. The model consists of a Pb-Br rich $APbX_3$:AX NC surface where we explore three possible $A - X$ surface terminations: alkylammonium – alkylcarboxylate ($R'NH_3^+$ - $RCOO^-$), alkylammonium – bromide ($R'NH_3^+$ - Br^-), and cesium – alkylcarboxylate (Cs^+ - $RCOO^-$). We examine various surface chemistries to see which are combinations are likely to form surface vacancies due to chemically induced ligand desorption from the surface. For each passivation scheme we compute electronic structure in the GS and L-ES for fully-passivated (pristine) and surface vacancy defects which reflect

desorption of surface ligands $A^+ + X^- \rightarrow AX$. We find that in the L-ES electronic configuration, regardless of the surface passivation scheme, electron surface trap states emerge inside the pristine bandgap where electron density is localized around surface Pb while the hole remains unaffected by the surface vacancy. To characterize the impact of surface trap-states on the photoluminescence properties we implement non-adiabatic excited-state dynamics where nonradiative relaxation rates are computed for non-adiabatic couplings and radiative rates are computed from Einstein coefficients. From the excited-state dynamics we find that the surface defect model shows a high PLQY of 75% with the pristine surface model having a 95% PLQY. This provides evidence that polaron-induced surface-defect states can give efficient bright PL.

6.2. Methodology

6.2.1. Ground-State and Lowest Excited-State Observables

As a starting point, we determine the optimized ground-state geometry, in the absence of defects, within the self-consistent DFT with N_{GS} number of electrons. This corresponds to the following mixed quantum-classical expression

$$H_e^{N_{GS}}(r) + H_{ph}(R) + H_{e-ph}^{static}(r,R) = H_{SKSO}^{N_{GS}}(r;R) \tag{6.1}$$

where $H_{SKSO}^{N_{GS}}(r;R)$ describes the electronic and nuclear degrees of freedom where the total energy depends parametrically on the nuclear coordinates R. This defines finding the minima of the potential energy surface (PES) with nuclear coordinates $R_{equilib}^{N_{GS}}$ for the N_{GS} electron system.

To approximate the lowest excited-state (L-ES), simulating the lowest energy photo-excitation, we fix electronic occupations so what would normally be the highest occupied SKSO has a lack of electron density (ie a hole) and the lowest unoccupied SKSO contains electron density. This redistribution of charge density will provide new forces acting on the nuclei which will reorganize around the charge density $\rho_{\sigma\sigma'}^{N_{L-ES}}$ with change in nuclear coordinates δR

$$H_e^{N_{L-ES}}(r) + H_{ph}(R) + H_{e-ph}^{static}(r,R) = H_{SKSO}^{N_{L-ES}}(r; R+\delta R) \quad (6.2)$$

This term describes finding the minima of the L-ES PES with nuclear coordinates $R_{equilib}^{N} + \delta R = R_{equilib}^{N_{L-ES}}$.

We also quantify changes in nearest neighbor bond angles.

$$g(\theta) = \sum_{IJ} \delta\left(\theta - \cos^{-1}\left(\frac{\vec{R}_I \cdot \vec{R}_J}{|\vec{R}_I||\vec{R}_J|}\right)\right) \quad (6.3)$$

where the angle is determined by inverse cosine of the dot product between ions $\vec{R}_I$ and $\vec{R}_J$ normalized by the magnitude of the bond lengths $\vec{R}_I$ and $\vec{R}_J$. The cut-off distance is determined from the distance of the first coordination peak of the pRDF.

Along molecular dynamics trajectories we track coordination numbers through time-resolved pRDFs

$$g(r,t) = \frac{1}{4\pi r^2}\sum_{IJ} \delta\left(r - \left|\vec{R}_I(t) - \vec{R}_J(t)\right|\right) \quad (6.4)$$

and at each timestep integrate up to the first coordination peak r_{bond} to give the average time-dependent coordination number $n_{bond}(t)$

$$n_{bonds}(t) = 4\pi \int_0^{r_{bond}} dr\, r^2 g(r) = \frac{1}{N_I N_J}\sum_{IJ} \int_0^{r_{bond}} dr\, \delta\left(r - \left|\vec{R}_I(t) - \vec{R}_J(t)\right|\right) \quad (6.5)$$

Surface defect formation energies are computed as

$$E_{DFE} = E_{NC} - (E_{NC+defect} + E_{reaction}) \quad (6.6)$$

Where $E_{DFE} > 0$ indicates forming surface defects is thermodynamically favorable and $E_{DFE} < 0$, forming surface defects is thermodynamically unfavorable. $E_{reaction}$ takes into account the chemical potential of the surface desorbed species.

6.2.2. Excited-State Dynamics

The Redfield tensor controls dissipative dynamics of the density matrix. From the Redfield tensor R_{ijkl} we can approximate a non-radiative recombination rate k_{nr} from Redfield matrix elements

$$k_{nr} \approx R_{HO-LU} \tag{6.7}$$

Note we employ an independent particle approximation where the full dynamics of the electron occupations ρ_c and hole occupations ρ_v

$$\frac{\partial}{\partial t}\begin{pmatrix}\rho_v \\ \rho_c\end{pmatrix} = \begin{pmatrix}R_{vv} & R_{vc} \\ R_{cv} & R_{cc}\end{pmatrix}\begin{pmatrix}\rho_v \\ \rho_c\end{pmatrix} \tag{6.8}$$

are decoupled such that intraband valence-to-valence non-radiative transitions R_{vv} and conduction-to-conduction R_{cc} are computed while interband valence-to-conduction R_{vc} and conduction-to-valence R_{vc} transitions are neglected based on the large timescale differences between carrier-cooling (ps) and non-radiative recombination (ns). To introduce the effect of non-radiative recombination we implement a dampening factor $e^{-\gamma t}$ where $\gamma = R_{vc} = R_{cv}$

$$e^{-\gamma t}\frac{\partial}{\partial t}\begin{pmatrix}\tilde{\rho}_v \\ \tilde{\rho}_c\end{pmatrix} = e^{-\gamma t}\begin{pmatrix}R_{vv} & 0 \\ 0 & R_{cc}\end{pmatrix}\begin{pmatrix}\tilde{\rho}_v \\ \tilde{\rho}_c\end{pmatrix} \tag{6.9}$$

where $\tilde{\rho}_v$ and $\tilde{\rho}_c$ represent a basis where the charge-carriers have an infinite lifetime $\lim_{t\to\infty}(\tilde{\rho}_v) = \lim_{t\to\infty}(\tilde{\rho}_c) = 1$ and are related to the basis of finite lifetime $\lim_{t\to\infty}(\rho_v) = \lim_{t\to\infty}(\rho_c) = 0$ as

$$\rho_v = \tilde{\rho}_v * e^{-\gamma t} \tag{6.10a}$$

$$\rho_c = \tilde{\rho}_c * e^{-\gamma t} \tag{6.10b}$$

Using relations shown in 6.10a and 6.10b and inserting into equation 6.8 it can be shown that equation 6.9 is the result. This means that running the full dynamics is equivalent to applying an exponential dampening factor to the uncoupled dynamics.

6.2.3. Computational Details

We preform geometry optimization on the ground-state and lowest-excited state potential energy surfaces, where the lowest-excited state corresponds to the lowest energy photo-excitation. Both optimizations are computed with the GGA functional with subsequent single point calculations where done using noncollinear spin DFT including the SOC interaction which where used to compute observables of the system. All calculations were performed at the Γ point. A simulation cell size of 31x31x31 Å with 7 Å of vacuum in each direction.

For computing average coordination number along the MD trajectory from time-resolved pRDFs we use the following distance cutoffs for integration: $r_{Pb-Br} = 5\ nm,\ r_{N-H} = 1.3\ nm,$ $r_{O-H} = 1.3\ nm$. These represent the distances where the first coordination peak is fully integrated over and but before having contribution from the second coordination peak.

6.3. Results

6.3.1. Ground-State Electronic Structure as Function of Surface Chemistry

In **Figure 6.2(a)-(c)** we investigate the ground-state (GS) and the lowest excited-state (L-ES) electronic structure for three possible surface chemistries to passivate the nanocrystal surface: (a) alkylammonium – alkylcarboxylate ($R'NH_3^+$ - $RCOO^-$), (b) alkylammonium – bromide ($R''NH_3^+$ - Br^-), and (c) cesium – alkylcarboxylate (Cs^+ - $RCOO^-$). The top row shows the GS optimized models, middle row shows the GS DOS, and the bottom row shows the L-ES DOS. Insets for the DOS show the corresponding S_h and S_e spinor Kohn-Sham orbitals (SKSOs) where the labels S_x signify that the envelope function of the SKSO is expected to be delocalized within the interior or the NC and decay at the boundary. For each surface passivation scheme, it is observed that the bandgaps are 'clean' and free from mid-gap/shallow trap states where electronic density is localized near the surface. This is confirmed by analysis of the highest

occupied and lowest unoccupied SKSOs where their charge density is delocalized throughout the interior of the NC core as expected for the S_h and S_e electronic states.

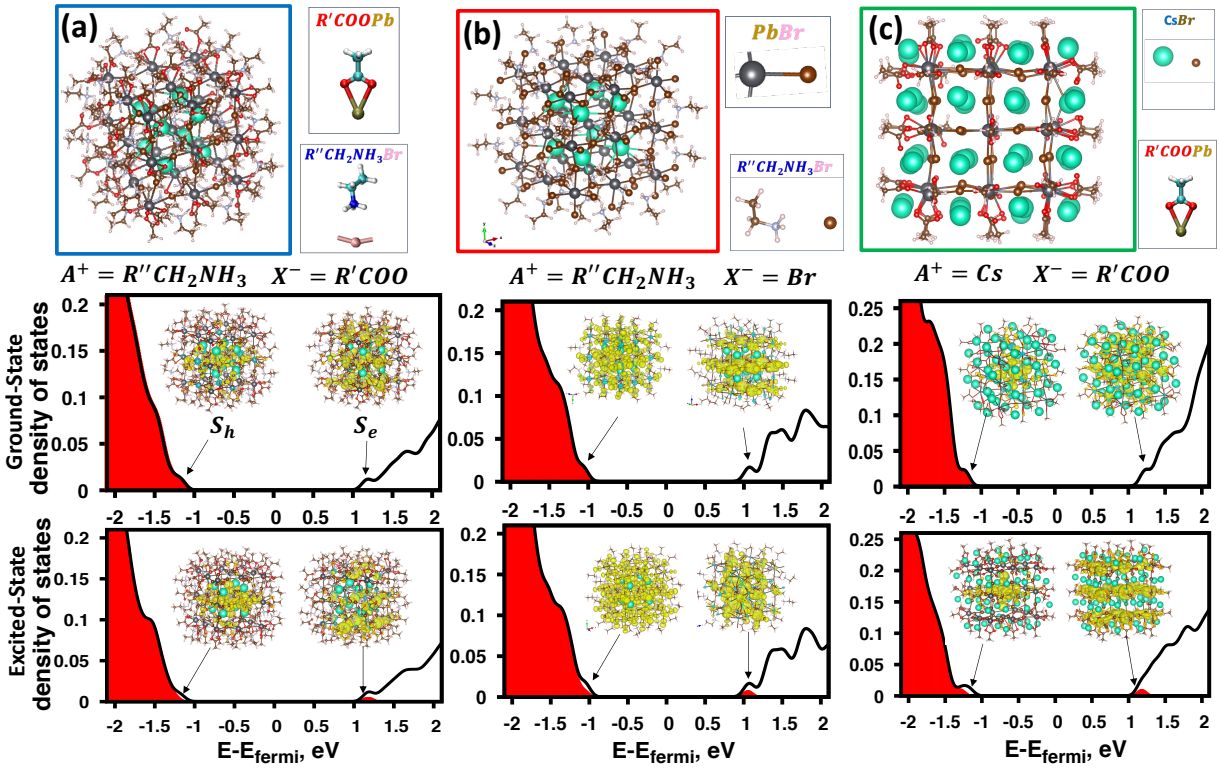

Figure 6.2: Description of three possible surface chemistries used to passivate the surface of $CsPbBr_3$ nanocrystals and their corresponding electronic density of states in the ground-state (middle row) and lowest excited-state (bottom row) electronic configurations. **(a)** Alkylammonium - carboxylate, **(b)** alkylammonium - bromide, and **(c)** cesium-carboxylate surface passivation schemes. Insets for the density of states figures are the corresponding spinor Kohn-Sham orbitals (SKSOs) for the S_h and S_e bands. S_h and S_e refer to the spherical symmetry of the envelope function for the SKSO where the charge density is delocalized throughout the interior of the nanocrystal and decays at the boundary. It is observed that each surface passivation scheme results in an open bandgap with no shallow or mid-gap trap states for the ground-state and excited-state electronic configuration.

In **Figure 6.3(a)-(d)** we identify a structure-property relationship between the electronic bandgap of the NC as a function of the surface passivation. Namely that carboxylates binding to surface Pb introduces lattice distortions that result in breaking of ideal Pb-Br bond distances and angles which increases the bandgap with increasing distortion. **Figure 6.3(a)-(b)** show radial distribution functions of Pb-Br bond distances and angular distribution functions for Pb-Br-Pb

bond angles for $R''NH_3^+$ - $RCOO^-$ (blue), $R''NH_3^+$ - Br^- (red), and Cs^+ - $RCOO^-$(green). In a pristine $CsPbBr_3$ crystal the Pb atoms form octahedral coordination with Br with expected bond angles being 90° and 180° with a uniform distribution of Pb-Br distances. For the geometry optimized atomistic models It is observed that the $R''NH_3^+$ - Br^-terminated surface have a near symmetric distribution of Pb-Br bond distances and a symmetric Pb-Br-Pb bond angles at 90° while the $R''NH_3^+$ - $RCOO^-$ and Cs^+ - $RCOO^-$ surfaces show a skewed distribution of Pb-Br bond distances and Pb-Br-Pb bond angles.

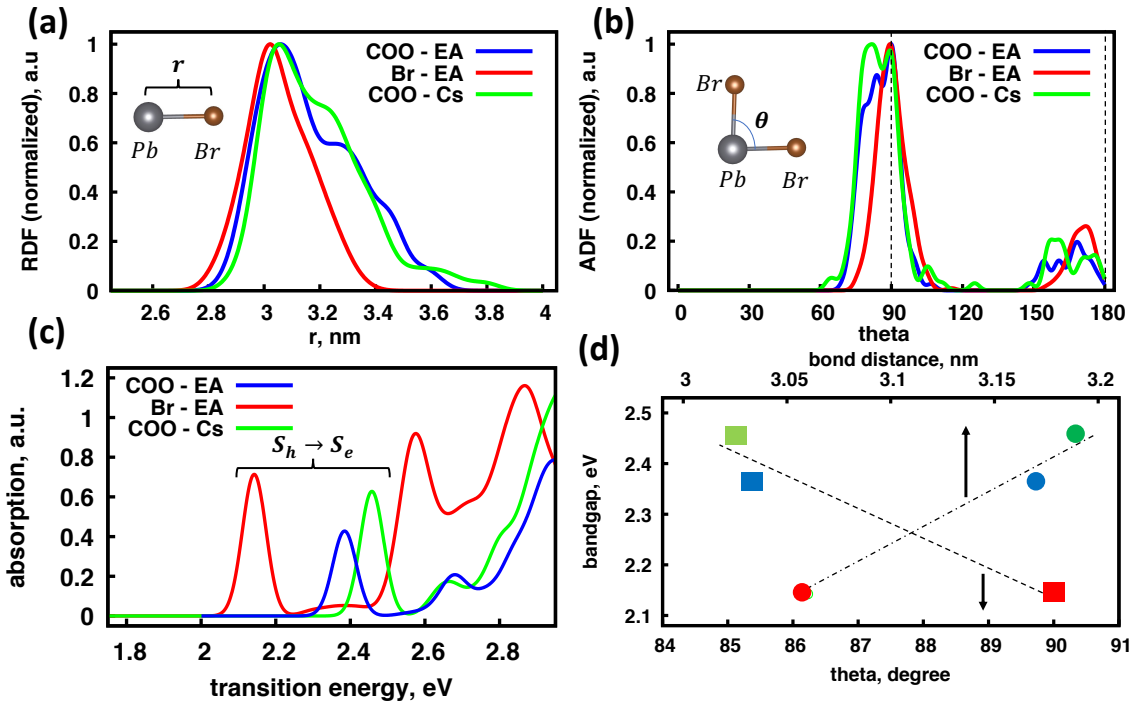

Figure 6.3: Structure-property relation between influence of surface chemistry on the Pb-Br coordination and the bandgap. **(a)** radial distribution of Pb-Br bonds and **(b)** angular distribution of Pb-Br-Pb coordination for alkylammonium-carboxylate (blue), alkylammonium-bromide (red), and cesium-carboxylate (green) surface passivation. It is observed that surfaces containing carboxylates (green, blue) show a broader distribution of radial and angular coordination than those without (red). **(c)** Ground-state absorption spectra for each respective model. It is observed that surfaces containing carboxylates also show a larger bandgap, signified by the $S_h \rightarrow S_e$ inset, than those without. **(d)** Expectation value of the Pb-Br-Pb bond angle (bottom, squares, dashed line) and radial bond distance (top, circles, dash-dot line) verses the bandgap for each model. The color scheme is the same as in **(a)-(c)**. It is observed that the bandgap increases with increasing deviation from ideal octahedral bond angles of 90° and with increasing Pb-Br bond distances. This is attributed to the carboxylates introducing strain on the surface Pb^{2+} resulting in the breaking of ideal octahedral coordination.

Figure 6.3(c) shows the computed absorption spectrum for each model which shows that the absorption onset, characterized as a $S_h \rightarrow S_e$ transition, shows a distribution of bandgap values ranging from 2.12 to 2.46. eV In **Figure 6.3(d),** we plot the expectation value of Pb-Br bond distances (top scale, circles) and Pb-Br-Pb bond angles (bottom scale, squares) versus the bandgap. It is found that there is a consistent correlation between the deviation from ideal octahedral coordination, due to $Pb - RCOO^-$ bonds on the surface, and an increased bandgap.

6.3.2. Polaronic Formation of *Bright* Surface Trap-States

In **Figure 6.4(a)-(b)** we investigate the impact of surface defects on the opto-electronic properties of the NC models. We consider two sites for defect formation: the 'face' position which in on the (100) crystal facet and an 'edge' position which is on the (110) facet. The defects are chosen to reflect the following chemical reactions which are likely to occur on the surface for the (i) $R'NH_3^+$ - $RCOO^-$, (ii) $R'NH_3^+ - Br^-$, and (iii) Cs^+ - $RCOO^-$ terminated surfaces:

$$R'NH_3^+Br^- + Pb^{2+}\ RCOO^- \leftrightarrow V_{A^+}Br^- + Pb^{2+}V_{X^-} + R'NH_2 + RCOOH \quad \text{(i)}$$

$$R'NH_3^+Br^- + Pb^{2+}\ Br^- \leftrightarrow V_{A^+}Br^- + Pb^{2+}V_{X^-} + R'NH_2 + HBr \quad \text{(ii)}$$

$$Cs^+Br^- + Pb^{2+}\ RCOO^- \leftrightarrow V_{A^+}Br^- + Pb^{2+}V_{X^-} + Cs(RCOO) \quad \text{(iii)}$$

where V_{A^+} and V_{X^-} represent vacancy defects at the $A^+$and X^-lattice sites. For each surface defect the geometry is reoptimized in the GS or L-ES configuration. Here we will focus on defect formation on the face of the $R'NH_3^+ - Br^-$ terminated surface. In **Figure 6.4(a)** we show the GS DOS along with the corresponding S_h and S_e SKSOs. We illustrate where the surface vacancy sites V_{A^+} and V_{X^-} are with the red dotted circle where there is an undercoordinated Pb^{2+} surface atom and a vacant A^+ site. We observe that the bandgap remains pristine with no signs of localization of the electronic density near the surface. But when the geometry is optimized in the

L-ES configuration we observe the appearance of an electronic state within the bandgap, shown in **Figure 6.4(b).** This emergent electronic state is revealed to be a shallow surface defect state where electronic density of the SKSO is localized on the undercoordinated surface Pb^{2+}, shown as an inset. The formation surface defect states inside the bandgap in the L-ES configuration is a general trend which is observed for the $R''NH_3^+$ - $RCOO^-$ and Cs^+ - $RCOO^-$ terminated surfaces as well.

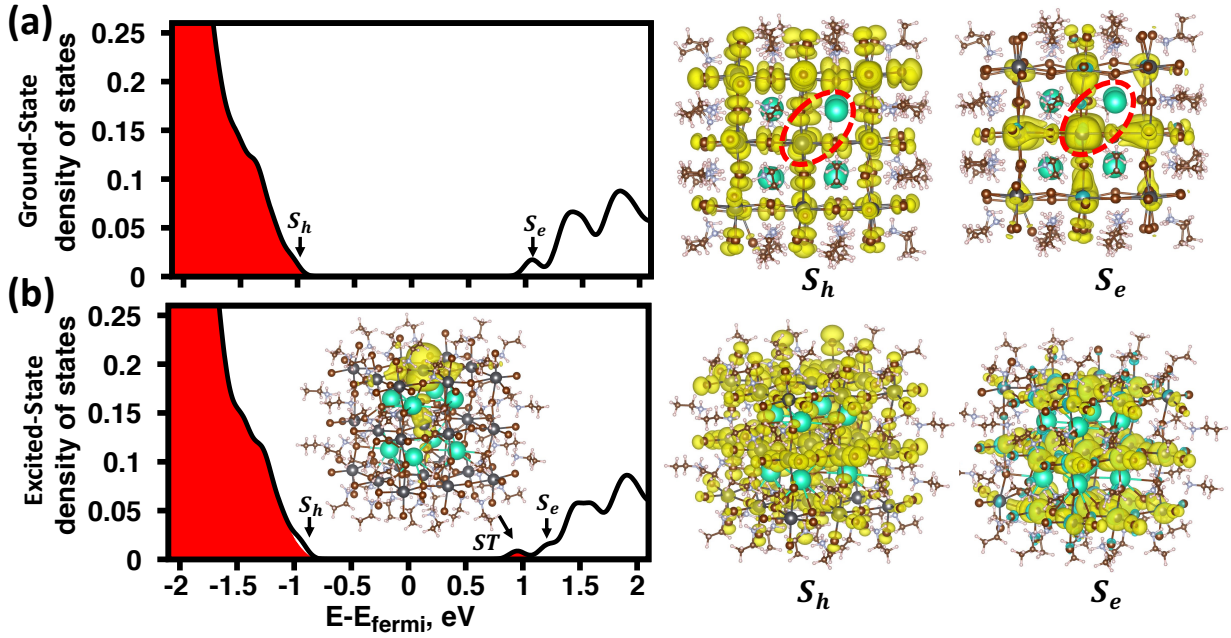

Figure 6.4: Impact of surface defects on the electronic DOS for the alkylammonium-bromide passivated surface. The surface of the $CsPbBr_3$ NC is altered to reflect the following chemical reaction: $R'NH_3^+Br^- + Pb^{2+}\ Br^- \leftrightarrow V_{A^+}Br^- + Pb^{2+}V_{X^-} + R'NH_2 + HBr$ which results in the surface having an undercoordinated Pb^{2+} and Br^-. This is done by manually removing $R'NH_3^+$ and Br^- from the surface and reoptimizing the geometry in either the ground-state or lowest excited-state configuration. **(a)** Density of states for the ground-state and **(b)** excited-state electronic configuration with specific SKSOs shown. In **(a)** the location of surface defects are circled with red-dashed line. The appearance of the shallow-trap states on the excited-state PES is a consistent feature that is observed for the alkylammonium-carboxylate and cesium-carboxylate surface chemistries.

To investigate the impact of shallow trap-state formation on the optical absorption spectra we compute transition dipoles, using the independent orbital approximation, for models optimized the GS and L-ES configuration. In **Figure 6.5(a)-(c)** we plot the absorption spectra

for the pristine (red), GS with a face defect (green), GS with an edge defect (blue), ES with a face defect (magenta), and ES with an edge defect (teal) for **(a)** $R'NH_3^+$ - $RCOO^-$, **(b)** $R'NH_3^+ - Br^-$, and **(c)** Cs^+ - $RCOO^-$ terminated surfaces. The main observation is that for all the models and defects considered the $S_h \rightarrow S_e$ transition remains relatively bright but when considering the surface defected models optimized in the L-ES configuration new optical features emerge lower in energy than the $S_h \rightarrow S_e$ transitions. These emergent low energy transitions are characterized as $S_h \rightarrow ST$. Interestingly, it is observed that these trap-state facilitated absorption features are relatively bright where it is generally assume that surface states will be optically dark.

To assess the thermodynamic stability of each surface chemistry configuration we compute defect formation energies (DFEs) for each model in the GS and L-ES configuration, shown in **Table 6.1**. The DFEs are computed with respect to the chemical potential of product formation for the chemical reactions described in (1)-(3). Negative (positive) DFEs correspond to the surface adsorbed (desorbed) configuration being more energetically favorable. In the GS configuration it is found that $R''NH_3^+$ - Br^- and Cs^+ - $RCOO^-$ surfaces prefer the surface adsorbed configuration while $R''NH_3^+$ - $RCOO^-$ prefers the desorbed configuration.

Table 6.1: Defect formation energies (DFE) computed for the various surface chemistries at various sites on the NC surface. Positive (negative) binding energies indicate that forming surface defects is thermodynamically favorable (unfavorable).

Defect Site	(i) R'NH3 - Br	(ii) R'NH3 -RCOO	(iii) Cs – RCOO
Face	-1.39 eV	1.05 eV	-1.12 eV
Edge	-1.39 eV	1.11 eV	-0.75 eV

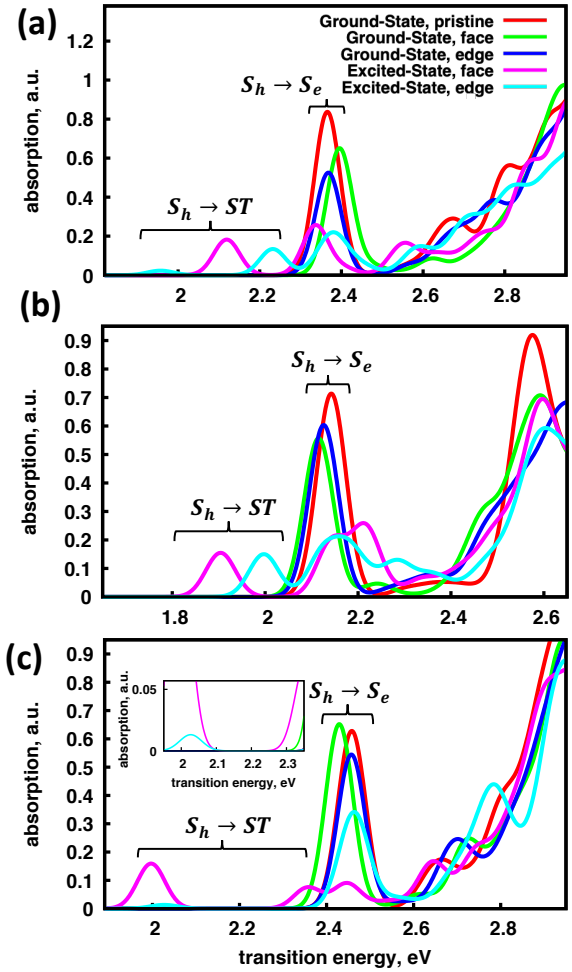

Figure 6.5: Impact of surface defects on the optical properties Comparison of the UV-VIS absorption spectra for the pristine (red), GS with a face defect (green), GS with an edge defect (blue), ES with a face defect (magenta), and ES with an edge defect (teal) for **(a)** alkylammonium-carboxylate, **(b)** alkylammonium-bromide, **(c) and** cesium-carboxylate surface passivation schemes. The main observation that for the pristine and surface defected models optimized on the GS PES (red, green, blue) the lowest energy transition is the $S_h \rightarrow S_e$ while the surface defected models optimized on the ES PES (magenta, teal) the lowest energy transitions are $S_h \rightarrow ST$ due to the emergence of surface trap states. Interestingly, some of the $S_h \rightarrow ST$ states are relatively bright in absorption.

6.3.3. Photo-Thermal Stability of Surface Chemistry

To test the photo-thermal stability of the LHP NC against surface defect formation we implement molecular dynamics on the pristine, fully-passivated NCs in the GS and L-ES electronic configuration at cryogenic (77K) and room (300K) temperatures for the $R''NH_3^+$ - $RCOO^-$ passivated surface. It is expected that the reaction barrier for ligand desorption from the

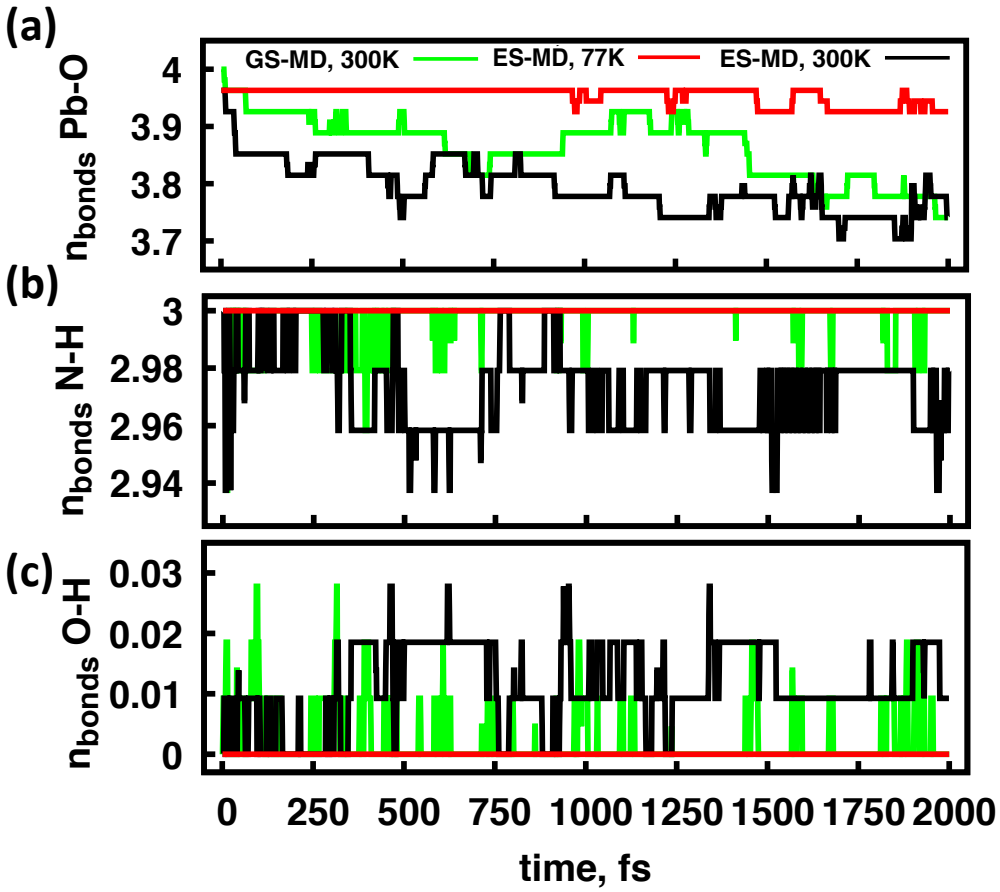

Figure 6.6: Change in (a) Pb-O, (b) N-H, and (c) O-H coordination numbers along GS-MD at 300K (green) and ES-MD trajectories at either 77K (red) or 300K (black) for the $R'NH_3^+ - RCOO^-$ passivated NC model. Coordination numbers are computed from time-resolved radial distribution function $g[r(t)]$ and integrated up to first coordination peak to give $n_{bonds}(t)$. From (a) it is observed that for the ES-MD(77K) there are small changes in Pb-O coordination while for the GS-MD(300K) and ES-MD(300K) trajectories show continuous decrease Pb-O coordination numbers, with small oscillations along the trajectory. For (b)-(c) it is also observed that there are no changes in N-H or O-H coordination. numbers for the ES-MD(77K) trajectory while the GS-MD(300K) and ES-MD(300K) trajectories show changes. Decrease in N-H coordination signifies conversion from ammonium to amine and increases in O-H coordination signifies conversion from carboxylate to carboxylic acid. This indicates chemical reactions, facilitated by proton transfer, are occurring on the surface where carboxylates are converted to carboxylic acid which has much less attraction to surface Pb resulting in photo-thermal surface degradation.

surface should be reduced in the L-ES compared to the GS due to the increased contribution of repulsive anti-bonding Pb-6p atomic orbitals. To characterize the transition from surface adsorbed to desorbed configuration we track Pb-O coordination numbers along the MD

trajectories through the use of RDFs. Integrating the RDF up to the first coordination peak gives the expectation value of Pb-O coordination's at the surface at each timestep. To track changes in surface chemistry, namely conversion of ammoniums to amines and carboxylates to carboxylic acids, we also compute N-H and O-H coordination numbers along the trajectory. There is an equilibrium between the protonated alkylammonium $R''NH_3^+$ and unprotonated alkylamine $R''NH_2$ which is facilitated by interaction with the strong base $R''COO^-$. Increases (decreases) in O-H (N-H) coordination are signatures of proton transfer occurring through the reaction **(ii)**.

In **Figure 6.6** we show the coordination number of **(a)** Pb-O bonds, **(b)** N-H bonds, and **(c)** O-H along a 2 ps trajectory for GS-MD at 300K (green), ES-MD at 77K (red), and ES-MD at 300K (black). The ES-MD(77K) trajectory shows essentially no change in Pb-O coordination and no changes in N-H or O-H coordination. The GS-MD(300K) and ES-MD(300K) trajectories show decreasing Pb-O coordination numbers accompanied by decreasing (increasing) N-H (O-H) coordination. This indicates that proton transfer on the surface helps promote the desorption of carboxylates and ammoniums from the surface consequently leaving surface vacancy sites. This analysis agrees with computed DFE formation energies from **Table 6.1** where the desorbed configuration is thermodynamically favored.

6.3.4. Excited-State Dynamics – Efficient Trap State Photoluminescence

For **Figure 6.7(a),** the non-radiative dynamics for the pristine surface, we see that after photo-excitation the charge carriers non-radiative relax to the S_h and S_e energy levels on the timescale of 10^2 ps and non-radiatively decay across the bandgap on the timescale of 10^4 ps. Changes in the SKSO occupations of holes in the valence band and electrons in the conduction band are shown in. Along the same trajectory there are radiative relaxation events, **Figure 6(b)-(c),** which occur before and after the charge carriers relax to the S_h and S_e energy levels. The

early events are hot-photoluminescence and after 10^2 ps the luminescence is from the $S_h \rightarrow S_e$ transition. From **Figure 6.7(c)** we see that the dominate radiative channel is the $S_h \rightarrow S_e$ transition as it has the longest lifetime.

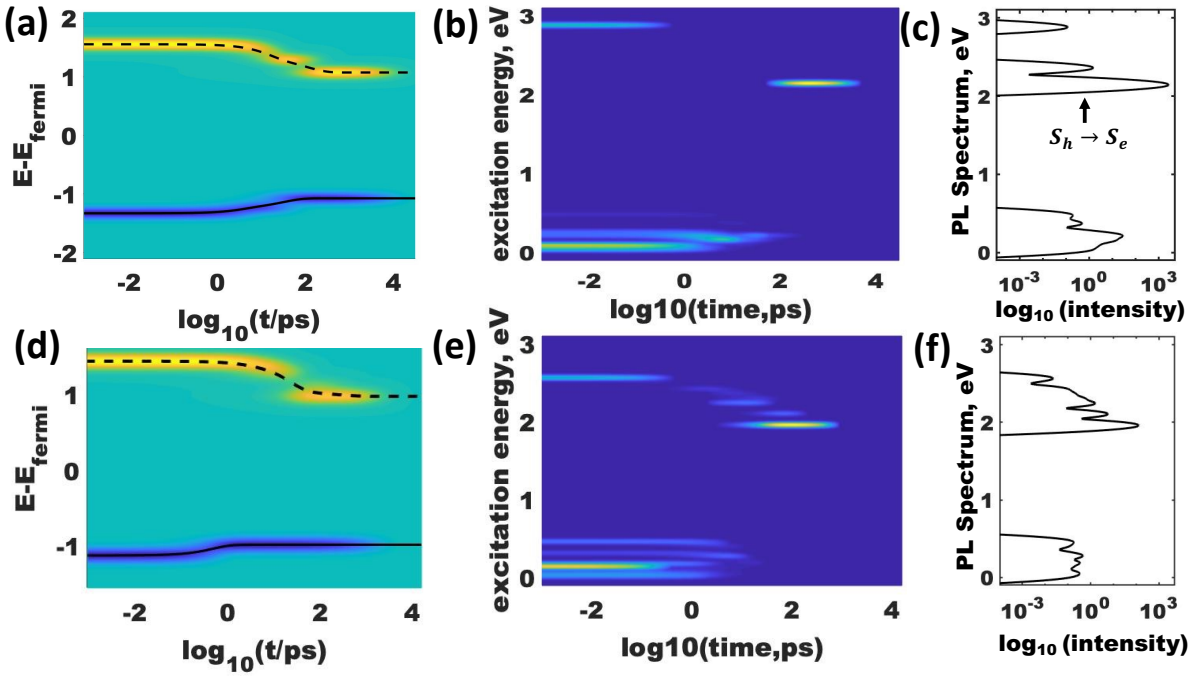

Figure 6.7: Non-adiabatic excited-state dynamics trajectories for **(a)-(c)** the pristine and **(d)-(f)** face-defect $R'NH_3^+ - Br^-$ terminated surface. **(a)** and **(d)** describe the non-radiative relaxation with initial conditions representing a photo-excitation The yellow (blue) lines represent non-equilibrium charge density of the photo-excited electron (hole) and the dotted (solid) line represents average energy of the electron. (hole). **(b)-(c),(e)-(f)** describe radiative relaxation along the trajectory with **(b),(e)** being time-resolved and **(c),(f)** time-integrated photoluminescence. For the pristine model, once the charge-carriers relax to the lowest excited-state energy there is bright photoluminescence from the $S_h \rightarrow S_e$. For the face-defect model, the charge-carriers relax to the lowest excited-state energy, with the photo-excited electron passing through the $S_e$electronic level, there is bright photoluminescence from the $S_h \rightarrow ST$ transition.

The non-radiative dynamics for the face-defect model, **Figure 6.7(d)**, shows similarities and differences to the pristine model, **Figure 6.7(a)**. First we will remark that the average electronic band energies for the surface defect model is similar to the pristine surface model due to the *ST* states oscillating between being 'inside' the bandgap and 'hidden' in the conduction bands. With this methodology we average over the states where the *ST* state is below and above

the S_e band. The similarity between the pristine and surface defect models is that the hot-electron cooling rates k_e are very similar while the hot-hole cooling rate k_h is 2 orders of magnitude faster for the surface defect model compared to the pristine model, as observed in **Table 6.2**. The radiative recombination dynamics, **Figure 6.7(e)-(f),** for the surface defect model is also similar to the pristine surface model. The main difference is that the PL transition energy is $\approx 200\ meV$ below the pristine surface PL and that the PL intensity of the surface defect model is an order of magnitude lower than pristine surface model. This attributed to the surface defect model having a seven times faster non-radiative recombination rate k_{nr}, see **Table 6.2**.

From the radiative and non-radiative recombination rates we compute PLQY, as observed in **Table 6.2**. For the pristine surface, there is a 2-fold degeneracy for the HOMO and LUMO states, giving four possible radiative recombination channels. We average over the recombination channels and find a PLQY = 95%. The surface defect model the degeneracy is broken and there is only one lowest energy recombination channel which has a PLQY = 75%. The reduction of the PLQY for the surface defected model is due to an enhanced non-radiative recombination rate k_h which is seven times faster than the rates for the pristine surface model.

6.4. Discussion

6.4.1. Impact of Surface Chemistry on the Bandgap

It has been observed that bulk and nanostructured $A^+B^{2+}X_3^-$ metal-halide perovskites have a positive deformation potential $\frac{\partial E_{gap}}{\partial \ln(V)} > 0$ [126] [127] [128]. In previous reports the focus is on how changes in chemical composition of the bulk crystal alters the structural distortion due to the Goldschmidt tolerance factor which is a measure of how efficient the A^+cations fill the space created by the $B^{2+} - X^-$ bonding network. Here the interesting observation, as detailed in **Figure 6.3,** is that changes in surface composition alters the bandgap through changes in the Pb-

Br bonding network. This is likely due to the difference in how Br^- and $RCOO^-$ coordinate to surface Pb^{2+}. Surface Br^- will have the same coordination bonding as bulk crystal Br^-but the $RCOO^-$ have a distribution of binding configurations [129], such as mono-dentate and bi-dentate, which will be different than the bulk crystal Br^-. This mis-match likely creates strain and breaks the ideal octahedral symmetry bonding network of Pb-Br. We keep in mind that these atomistic models, about 2nm in edge length, are smaller in size than what is typically observed in experiment, typically 3-15nm. So is likely that these effects are accentuated for smaller NCs due larger surface area to volume ratio. The main consequence would be that the bandgap would not strictly follow the commonly used effective mass approximation and that the surface chemistry can result in the EMA underestimating the bandgap.

Table 6.2: Summary of radiative and non-radiative relaxation dynamics from the excited-state dynamics.

Pristine Surface, 77K					
HO-x	LU+y	OS	k_r [1/ns]	k_{nr} [1/ns]	PLQY
HO	LU	1.22	3.03	0.13	0.96
HO-1	LU	1.07	2.66	0.13	0.95
HO	LU+1	0.85	2.12	0.15	0.93
HO-1	LU+1	0.73	1.81	0.13	0.93
average		0.97	2.41	0.13	0.95
Surface Defect, 77K					
HO	LU	1.06	2.20	0.75	0.75

6.4.2. Role of Proton Transfer on Surface Binding Stability

The surface chemistry of lead halide perovskite nanocrystals, using the original synthesis procedure[29], has shown to be one of the main hinderances towards their long-term colloidal

stability. It was found that there is a dynamic equilibrium between adsorbed and desorbed configurations of ligands on the NC surface[130] which over time leads to colloidal instability and precipitation of solution due to aggregation formation. From the *ab Inito* molecular dynamics trajectories for the $R''NH_3^+$ - $RCOO^-$ passivated surface, **Figure 6.6**, we observe that the coordination of $RCOO^-$ to surface $Pb^{2+}$is reduced through protonation by an adjacent $R''NH_3^+$. This agrees with the reports of how the acid-base equilibria has a strong influence on their colloidal stability [125] [131]. This motivates the use of surface chemistries that are unaffected by the environmental pH, such as zwitterions[85] and aprotic alkyl-ammoniums[121].

6.4.3. Impact of Surface Vacancy Defect on Photoluminescence Properties

In colloidal $CsPbBr_3$ NCs there have been reports of stretched exponential PL decay with decreased NC size[132-133]. Single exponential PL decay is considered to come from two level system whereas a stretched exponential decay is a signature of a distribution of relaxation pathways. These atomistic simulations help provide insight that bright surface trap states can introduce additional radiative pathways which could be the origin of stretched exponential photoluminescence decay.

Another interesting note is that the surface defect model showed a red-shifted PL transition energy compared to the pristine surface. It has been observed that with decreased NC size (increased surface-to-volume ratio) that the Stokes shift increases significantly [80, 134]. From the electronic structure calculations as described as apart of **Figure 6.4**, we find that the trap-states only emerge after polaronic nuclear reorganization due to charge-carriers occupying the trap-state (ie after photo-excitation) and that the surface defected model can show relatively bright emission, see **Figure 6.7**. Thus absorption could occur via the $S_h \rightarrow S_e$ transition across

the pristine bandgap E_{gap} and then photoluminescence via the $S_h \rightarrow ST$ transition with transition energy $E_{gap} - E(ST)$ where $E(ST)$ is the reorganization energy of the surface-trap state.

6.5. Conclusion

Lead halide perovskite nanocrystals are of interest for their opto-electronic properties. In particular as luminescence sources for traditional light-emitting devices and next generation devices such as quantum information manipulation and processing. One of the beneficial properties of LHP NCs is their defect tolerance. To this date, the ground-state energetics of trap state formation and electronic structure has been well characterized using *ab Initio* atomistic methods where it is found that lattice and surface point defects generally result in the energy bands contributed by defect sites to remain 'hidden' in the valence and conduction bands. But in realistic situations these vacancy sites can be occupied by polaronic charge carriers, due to photo-excitation, which can rearrange the alignment of these trap states due to significant nuclear reorganization energies. In this work we investigate the polaronic occupation of model LHP NC with pristine surface passivation or vacancy defects and the impact of the surface vacancies on the excited-state dynamics, such as PLQY and recombination rates. We consider multiple possible surface chemistries (A=Cs^+ ,R'NH_3^+ ; X=Br-, $RCOO^-$) to passivate the surface of the LHP NC model.

From examining the ground-state electronic structure of LHP NCs, having fixed edge length of 2nm, with various surface chemistries we find that the bandgap can be tuned over a range of $\sim 300\ meV$ with each passivation scheme having bright $S_h \rightarrow S_e$ optical transitions. The $R'NH_3^+$ - Br^- terminated surface showing the smallest bandgap and the $R'NH_3^+/Cs^+$ - $RCOO^-$ passivated surfaces showing larger bandgaps. This is attributed to surface binding of $RCOO^-$ to

surface Pb^{2+} providing lattice strain which increases the bandgap due to it's positive deformation potential $\frac{\partial E_{gap}}{\partial \ln(V)} > 0$.

When considering the effect of surface vacancies, represented as ion pairs desorbing from the surface through the chemical reaction $A^+ + X^- \rightarrow AX$, on the electronic structure we find that in the ground-state configuration the bandgap remains pristine. But when considering the lowest-excited-state configuration, approximating a photo-excitation by placing an electron in S_e band and having a hole in the S_h band, surface trap-states ST emerge inside the bandgap $\sim 100 - 400\ meV$ below the S_e band. This is attributed to polaronic reorganization. Interestingly, the surface trap states contribute relatively bright $S_h \rightarrow ST$ optical absorption signatures where it is generally assumed that these features would be dark.

To investigate the influence of surface defect vacancies on the LHP NC photoluminescence properties we implement excited-state dynamics simulations in density-matrix formalism where non-radiative relaxation is treated using Redfield theory and radiative relaxation is treated using Einstein coefficients for spontaneous emission. It was found that the surface defected model shows an enhanced non-radiative recombination rate which reduces the photoluminescence quantum yield (PLQY) from 95% for the pristine surface to 75%. This is accompanied by an order of magnitude reduction in PL intensity and a red-shift of the transition energy.

In total, this study provides more support for the defect tolerance of LHP NCs along with evidence of surface trap states contributing to efficient photoluminescence. The observation of relatively bright surface trap states could provide insight into photo-physical phenomena, such as the size-dependent stretched-exponential photoluminescence decay and Stokes shifts.

7. MANGANESE-DOPED LEAD HALIDE PEROVSKITE NANOCRYSTAL: TOWARDS MODELING SPIN-FLIP TRANSITIONS AND D-D PHOTOLUMINESCENCE

7.1. Introduction

Doping atomic impurities into semiconducting materials has long been a long-standing method for modifying their electronic transport properties and serving as the basis of solid-state electronics. Impurity doping of nanostructured materials has proven to be an effective method to further modulating material properties.[135] Specifically for nanocrystals (NCs), it has been found that incorporation of atomic impurities, such as transition metals and lanthanides, into the NC lattice can provide benefits for the intrinsic fluorescence properties,[136] or introduce additional radiative pathways that can be used for up-conversation,[137-138] down-conversion,[139-140] or dual-photoluminescence.[141]

Efficient Mn^{2+} sensitization has been observed to occur in $CsPb_{1-x}Mn_xCl_3$ and $CsPb_{1-x}Mn_xBr_3$ nanocrystals which display duel photoluminescence.[142] Fast (~1-10ns)[68] narrow-band blue (~ 410nm) or green (~510nm) from the exciton recombination and slow (~1ms) broad-band orange phosphorescence (~ 600nm) from the atomic Mn^{2+} dopants through the spin-forbidden $^4T_{1g} \rightarrow {}^6A_{1g}$ transition at room temperature. The Mn^{2+} luminescence is sensitized by the NC exciton through an energy transfer process.[143] Within the LHP lattice the Mn^{2+} ion is suspected to substitute for Pb^{2+} within the octahedral coordination. The electronic structure for the 3d orbitals the Mn^{2+} ion are very sensitive to their coordination chemistry. For the free ion in vacuum all 3d orbitals are degenerate. In a halide (weak splitting) ligand field the 3d orbitals will split into the t_2 and e symmetry groups. In an octahedral coordination the t_2 will be lower in energy than the e groups and vise versa for tetrahedral coordination. The orbital energy spacing is depicted in **Figure 7.1(a)**.

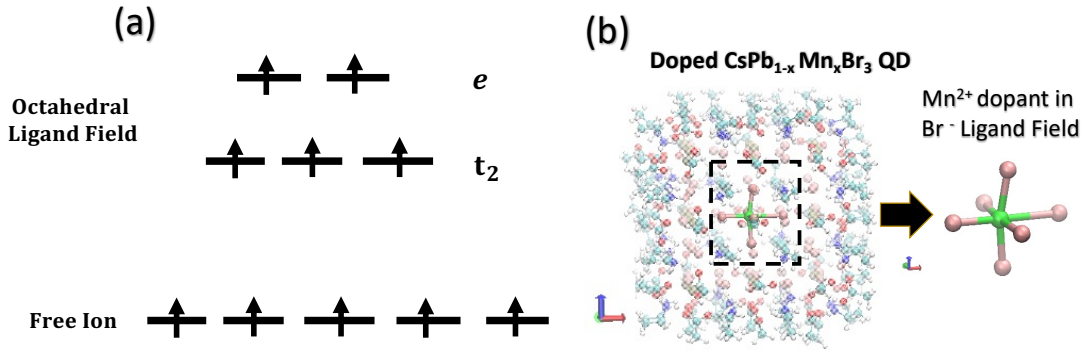

Figure 7.1: The Mn^{2+} doped $CsPb_{1-x}Mn_xBr_3$ QD which has the same morphology as the intrinsic QD, but with the central most Pb^{2+} atom substitutionally replaced with Mn^{2+}.

For the Mn^{2+} transition metal there are four general photo-physical pathways to consider: ligand-to-ligand, metal-to-ligand, ligand-to-metal, and metal-to-metal. Luminescence from Mn^{2+} dopants is generally considered to come from metal-to-metal transitions. In either octahedral or tetragonal coordination the ground-state electronic structure is expected to be sextet $S = 5/2$ with the lowest excited-state is expected to be quintette $S = 3/2$. This requires a change in spin (ie. spin-flip) for luminesce to occur, which is a 'dipole-forbidden' process. Higher order processes, such as spin-orbit coupling (SOC) or vibronic spin-orbit coupling, are required observe metal-to-metal d-d luminescence from Mn^{2+} ions. This is used to rationalize the long $1 - 10\ ms$ luminescence lifetime observed in experiments. There is also the possibility of Mn-Mn interacts at threshold doping concentrations. For a Mn-Mn dimer (connected by a halide bridge) they can take either a high (ferromagnetic) or low (anti-ferromagnetic) spin configuration. Experimentally it is generally found that with increased Mn/Pb doping ratios that there is a red-shift of the dopant PL along with PL lifetimes that become non-single exponential.

Rigorously, the electronic structure of transition metals should be treated with multi-reference methods (going beyond using a single Slater determinate) due to the degeneracies and highly correlated nature of d orbitals. Although DFT is a single reference theory, it has shown to

provide reliable structures and ground-state spin configurations. One of the failings of DFT is to provide quantitively accurate predictions of the relative energies between d orbital energy levels. Methods such as DFT+U have been developed to remedy these situations where the d orbitals are specifically isolated and treated with an improved description of electron-electron interactions giving better agreement with experiment. Overall, DFT and TDDFT methods have been used to rationalize the photo-physics of Mn^{2+} doped nanocrystals [144] [145].

Modeling the dynamics that lead to transition metal Mn^{2+} luminescence is also a challenging task. There are two primary steps: the non-radiative sensitization of the ligated Mn^{2+} ion within the nanocrystal and the d-d luminescence pathway. The sensitization can happen through an energy transfer process, where a Coulombically bound exciton is transferred to the ligated Mn^{2+}, or through charge-transfer processes where the photo-excited electron and photo-induced hole are transferred to the dopant individually. Describing energy transfer processes requires computing the electronic structure of Coulombically bound excitons whereas charge-transfer pathways can be modeled where electrons and holes are independent of one another. To model the luminescence electronic structures which incorporate SOC are needed to describe spin-flip optical transitions.

Here we apply the methodology described in Chapter 4 to model the photo-physics of various Mn-doped LHP structures. Initially we start with the electronic structure of a Mn-doped $CsPbBr_3$ NC, computed with GGA pseudopotentials. It was found that the 3d orbitals are deep in the conduction band giving an energetically unfavorable alignment for Mn^{2+} sensitization. This motivated to investigate the electronic structure and excited-state dynamics of Mn-doped $CsPbCl_3$ NC, bulk $CsPbCl_3$, and RP phased DA_2PbCl_4 LHP due to the wider bandgap of intrinsic $CsPbCl_3$ materials. It is found that the RP phase and the bulk crystal LHP, with LDA

pseudopotentials, give the best qualitative alignment of Mn^{2+} 3d orbitals which can lead to d-d luminescence transitions. From the excited-state dynamics it is found that the non-radiative transfer of photo-induced electrons and holes to the Mn dopant site occurs on at a faster rate than the intrinsic non-radiative cooling for the LHP host material giving rise to efficient sensitization of the ligated Mn^{2+} dopant. Computed PLQY for the d-d PL transitions where found to be less than 1% with sub nanosecond radiative lifetimes. This is attributed to the single-reference character of DFT which is not able to enforce spin-forbidden character of the radiative recombination.

7.2. Methods

7.2.1. Spin-Polarized DFT

Here we introduce the basic equations and quantities of SP DFT calculations needed to define relevant observables for open-shell systems and keep consistent notations. For equations (7.1) $\delta_{\sigma\sigma'}$ is the Kroenecker-delta function, σ and σ'define spin projections α or β, $v_{\sigma\sigma'}^{\mathrm{eff}}(\vec{\mathrm{r}})$ is the spin-dependent external potential, and $\varphi_{i\sigma}(\vec{r})$ is a spin-dependent KSO. Self-consistent DFT electronic structure calculations with spin-dependent external potentials equation (7.2)

$$\sum_{\sigma,\sigma'=\alpha,\beta}(-\delta_{\sigma\sigma'}\nabla^2 + v_{\sigma\sigma'}^{eff}(\vec{r}))\varphi_{i\sigma}(\vec{r}) = \varepsilon_{i,\sigma\sigma'}\,\varphi_{i\sigma'}(\vec{r}) \tag{7.1}$$

$$v_{SP}^{eff}(\vec{r}) = = \begin{pmatrix} \mathrm{v}_{\alpha\alpha}^{\mathrm{eff}}(\vec{\mathrm{r}}) & 0 \\ 0 & \mathrm{v}_{\beta\beta}^{\mathrm{eff}}(\vec{\mathrm{r}}) \end{pmatrix} \tag{7.2}$$

provide SP KSOs $\varphi_{i,\sigma}^{SP}(\vec{r})$ with energy $\varepsilon_{i,\sigma}^{SP}$ with $\sigma = \alpha$ or β defining orthogonal spin-projections. SP KSOs obey the orthogonality relation.

$$\int d\vec{r}\varphi_{i\sigma}^{*}(\vec{r})\,\varphi_{j\sigma'}(\vec{r}) = \delta_{ij}\delta_{\sigma\sigma'} \tag{7.3}$$

Spin polarization parameter $\Delta N_{\uparrow\downarrow} = N_\alpha - N_\beta$ defines the spin multiplicity S = $\Delta N_{\uparrow\downarrow}/2$ and the magnitude of the magnetization vector $|\overrightarrow{\mathrm{M}}| = \Delta N_{\uparrow\downarrow}$. It is noted that in a SP basis the magnetization vector magnitude is constant during excited-state dynamics i.e. spin is conserved.

7.2.2. Computational Details

The ground-state electronic structure of our atomistic model was found using SP DFT with the either LDA or GGA PBE functional[74] in a plane-wave basis set along with (PAW)[75-76] in VASP[77] software. From the ground-state nuclear configuration computed with the either LDA or GGA functional, single point calculations where done using noncollinear spin DFT including the SOC interaction which where used to compute observables of the system. All calculations were performed at the Γ point. A simulation cell size of 31x31x31 Å with 7 Å of vacuum in each direction.

The Mn-doped $CsPbBr_3$ NC structure was found from substitutionally replacing the central most Pb2+ ion of the model used in **Sections 4** and **5** with a Mn^{2+} ion. The Mn-doped $CsPbCl_3$ NC structure was constructed from craving out a 2x2x2 unit cell from the bulk $CsPbCl_3$ and passivating the surface with Cs-Cl ions. The 2D RP phased DA_2PbCl_4 atomistic structure was found from published experimental crystallography measurements.

For open shell systems spin-polarized calculations where implemented. Mn^{2+} surrounded by a weak ligand field is expected to take a high spin configuration $\Delta N_{\uparrow\downarrow} = 5$ as opposed to being in a strong ligand field where $\Delta N_{\uparrow\downarrow} = 1$. SP DFT calculations showed that $\Delta N_{\uparrow\downarrow} = 5$ provided the lowest total energy for all systems investigated with one Mn^{2+} dopant. For the models which contain two Mn^{2+} dopants it was found that the models with the lowest total energy took the antiferromagnetic low spin configuration $\Delta N_{\uparrow\downarrow} = 0$ as opposed to the ferromagnetic high spin configuration $\Delta N_{\uparrow\downarrow} = 10$.

7.3. Results

7.3.1. Mn-Doped $CsPbBr_3$ Nanocrystal DOS and Spectra

For the doped NC, SP PBE geometry optimization was done for two spin configurations: low spin S=1/2 and high spin S=5/2. The spin configuration for the *doped* QD that provided the lowest total energy was S=5/2 which is expected for weak-field halide ligands. During geometry optimization for the S=5/2 spin configuration, the Br^- ligand field surrounding the Mn^{2+} dopant adapted to a square pyramidal geometry. For the spin α DOS, see **Figure 7.2(a)**, it is seen that there are two states that appear within the bandgap, above the valence band edge. pDOS analysis, see **Figure 7.2(c)**, shows that these states are dopant Mn^{2+} hybridized with atoms of the perovskite QD. Further analysis shows these states are Mn^{2+} $3d_{z2}$ and $3d_{x2-y2}$ states hybridizing with Br *4p.* For the spin β component, there is a manifold of unoccupied Mn^{2+} *3d* states that appear 0.19 eV below the conduction band edge, see **Figure 7.2(c)**. The bandgap for the spin α and spin β components are 2.37 eV and 3.14 eV, respectively. The SOC DOS calculation, see **Figure 7.2(b)**, shows a bandgap of 1.77 eV. pDOS, see **Figure 7.2(d)**, shows that the valence band edge is composed primarily of spin α components. In the conduction band, it is seen that the band edge orbitals were composed of perovskite states, which screen the dopant states and places them deep within the conduction band. Further analysis shows the band edge is composed of Pb 6*p* SKSOs.

7.3.2. Mn-Doped $CsPbCl_3$: Nanocrystal, Bulk Crystal, and Ruddellsdon Popper DOS and Spectra

We investigate the electronic structure of Mn-doped $CsPbCl_3$ LHP for three different structures: (i) 0D $CsPbCl_3$ nanocrystal, (ii) 2D Ruddelsdon-Popper phase DA_2PbCl_4, and (iii) 3D bulk $CsPbCl_3$ LHP. For each model we compare the electronic density of states to the pristine,

undoped structure. For the 0D NC, **Figure 7.3,** it is found that the pristine NC the HO and LU SKSOs are delocalized throughout the entire NC while for the NC with a Mn^{2+} dopant the HO SKSO is localized to the 3d orbital of the Mn^{2+} atom while the LU shows hybridization between surface states of the NC and the 3d orbital of the Mn^{2+} dopant.

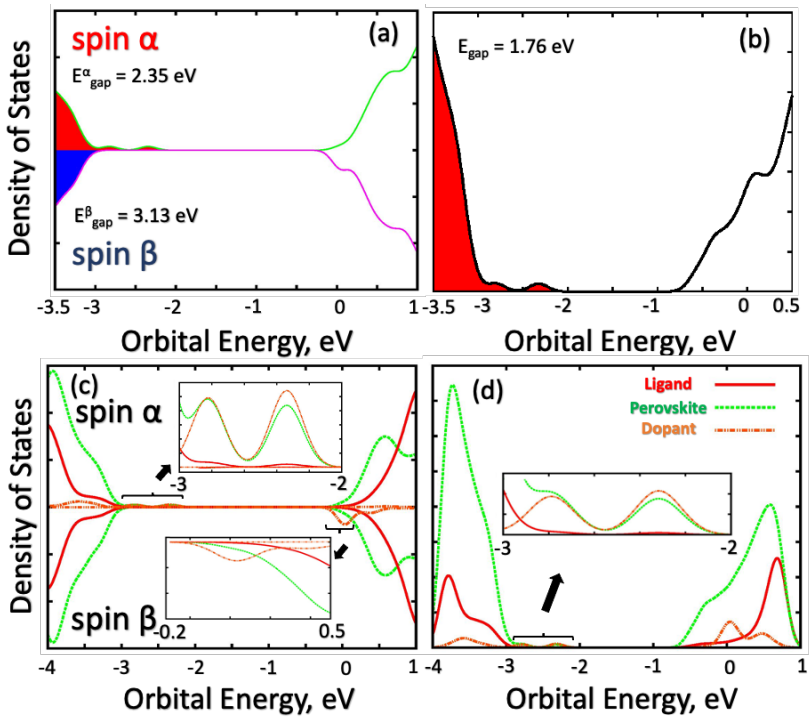

Figure 7.2: (a)-(b) Density of states and **(c)-(d)** partial density density of states for spin-polarized and spinor electronic basis. It is observed that in the spin-polarized basis both the occupied and unoccupied Mn-3d KS orbitals (orange) are located inside the perovskite NC bandgap while the inclusion of SOC lowers the Pb-6p (green) states in the conduction band lower in energy than the Mn-3d state

For the 2D RP phased DA_2PbCl_4 models, shown in **Figure 7.4(a)-(c),** we compare the electronic DOS in **Figure 7.4(d)-(f)** for **(d)** the pristine lattice, **(e)** the lattice with one Mn^{2+} dopant (Mn/Pb = 0.25), and **(f)** with two Mn^{2+} dopants (Mn/Pb=0.5). It is observed that with increasing Mn doping concentration that additional electronic states are introduced inside the pristine lattice bandgap. Inspection of the HO and LU SKSOs show that the charge densities are localized to the 3d orbitals of the Mn^{2+}.

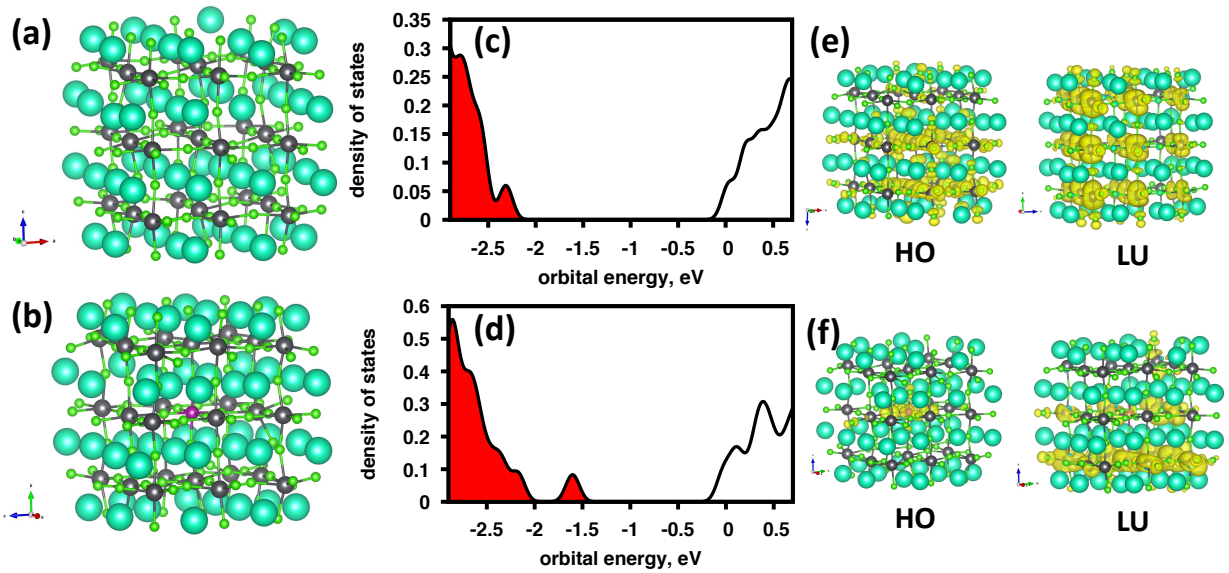

Figure 7.3: (a)-(b) $CsPbCl_3$ NC atomistic model for **(a)** pristine lattice and **(b)** one Mn^{2+} dopant. **(c)-(d)** Electronic DOS for **(c)** pristine lattice and **(d)** one Mn^{2+} dopant. **(e)-(f)** HO and LU KSOs for **(e)** pristine lattice and **(f)** one Mn^{2+} dopant. It is observed that for the doped NC the HO state is localized to the Mn^{2+} dopant while for the LU the dopant hybridizes with surface states.

For the 3D bulk $CsPbCl_3$ LHP, shown in **Figure 7.5(a)-(c),** we show the electronic DOS in **Figure 1(d)-(f)** for **(d)** the pristine lattice, **(e)** the lattice with one Mn^{2+} dopant (Mn/Pb = 0.037), and **(c)** with two Mn^{2+} dopants (Mn/Pb=0.074). Again It is observed that with increasing Mn doping concentration that additional electronic states are introduced inside the pristine lattice bandgap. Inspection of the HO and LU SKSOs show that the charge densities are localized to the 3d orbitals of the Mn^{2+} dopants. For the rest of the manuscript we will focus on the 2D RP phased DA_2PbCl_4, and 3D bulk $CsPbCl_3$ LHP.

Structural characterization of the LHP structures are determined using pRDF Specifically, we focus on the Pb-Cl and Mn-Cl nearest neighbor coordination distances and angles. In **Figure 7.6(a)-(b)** we show the pRDF for **(a)** 2D RP phased DA_2PbCl_4 and **(b)** 3D bulk $CsPbCl_3$. For each model we plot the Pb-Cl pRDF for the pristine lattice (red, solid), doped with one Mn2+ (red, dot), and two Mn2+ (red, dash-dot) along with Mn-Cl pRDF for when the structures are doped with one (black, dot) and two (black, dash-dot). For both LHP phases it is

observed that the Mn-Cl coordination distances are ~0.3nm shorter than the Pb-Cl coordination distances. Overall, this shows that the 2D RP phased DA_2PbCl_4 shows lower structural stability, attributed to the high Mn/Pb doping concentrations, and allows the Mn^{2+} to take on tetrahedral coordination while in the 3D bulk $CsPbCl_3$, with lower Mn/Pb doping concentrations, the Mn-Cl coordination remains octahedral

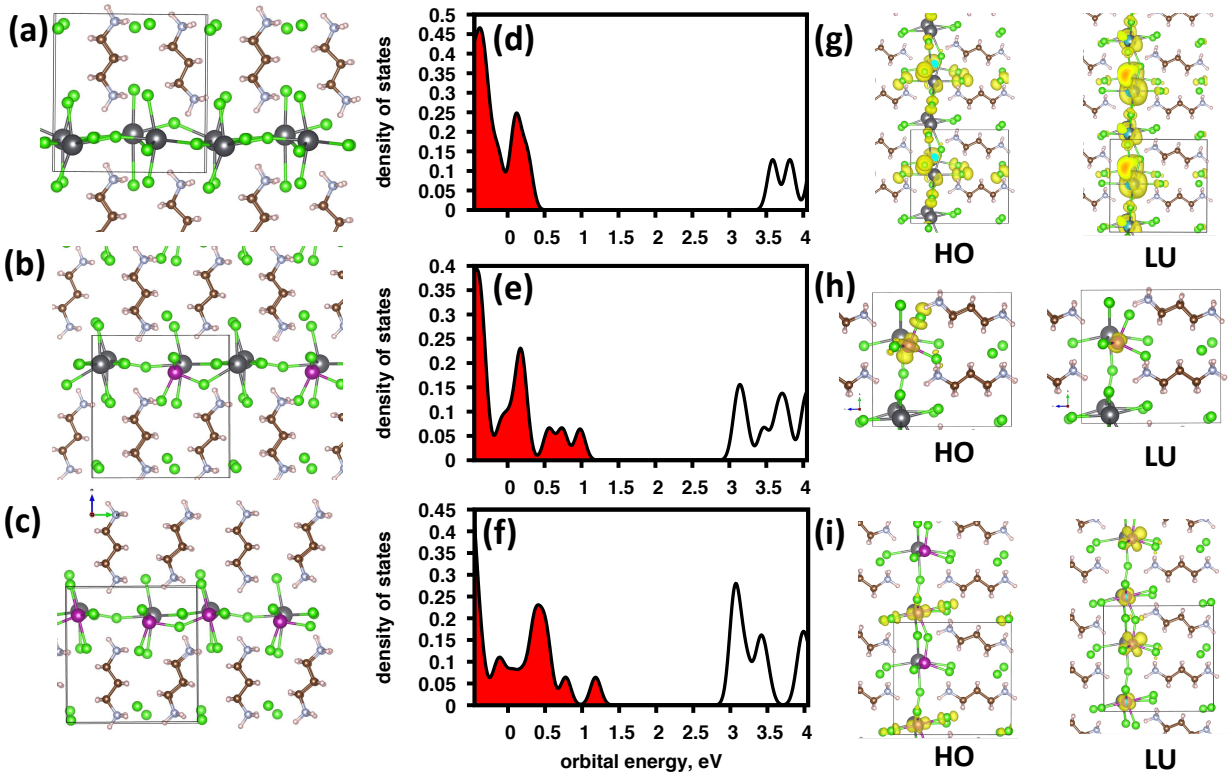

Figure 7.4: (a)-(c) RP phased DA_2PbCl_4 LHP atomistic model for **(a)** pristine lattice, **(b)** one Mn^{2+} dopant, and **(c)** two Mn^{2+} dopant. **(c)-(e)** Electronic DOS for **(c)** pristine lattice, **(d)** one Mn^{2+} dopant, and **(e)** two Mn^{2+} dopant. **(g)-(i)** HO and LU KSOs **(g)** pristine lattice, **(h)** one Mn^{2+} dopant, and **(i)** two Mn^{2+} dopant.

To investigate the optical properties of the LHP structures we compute transition dipoles and oscillator strengths using a spinor KSO basis which naturally allows the description of d-d transitions for the Mn^{2+} dopants. **Figure 7.7(a)-(b)** shows the absorption spectrum, in $\log_{10}$ scale, for **(a)** 2D RP phased DA_2PbCl_4 and **(b)** 3D bulk $CsPbCl_3$. For both structures it is seen that the pristine lattices (red, solid) show wide bandgap absorption onsets above 3 eV with the 2D RP

phased DA_2PbCl_4 showing a larger bandgap than the 3D bulk $CsPbCl_3$. With the introduction of one Mn^{2+} dopant into the lattice (green, solid) it is observed that there is a large redshift in the absorption onset around 2.1 eV and a 3-4 order of magnitude reduction in the intensity of the peak. These are attributed to the d-d optical transitions of the Mn^{2+} dopant. When two Mn^{2+} dopants are in the lattice an additional red-shift is observed for both LHP phases. This is attributed to the delocalization of the LU KSOs for both phases, see **Figures 7.4(g)-(i)** and **7.5(g)-(i)**. Note that the delocalization in the RP phased DA_2PbCl_4 extends across the entire unit cell while for 3D bulk $CsPbCl_3$ the KSO is delocalized across just the two Mn^{2+} dopants. This is likely why the RP phased DA_2PbCl_4 shows a much larger red-shift than the 3D bulk $CsPbCl_3$.

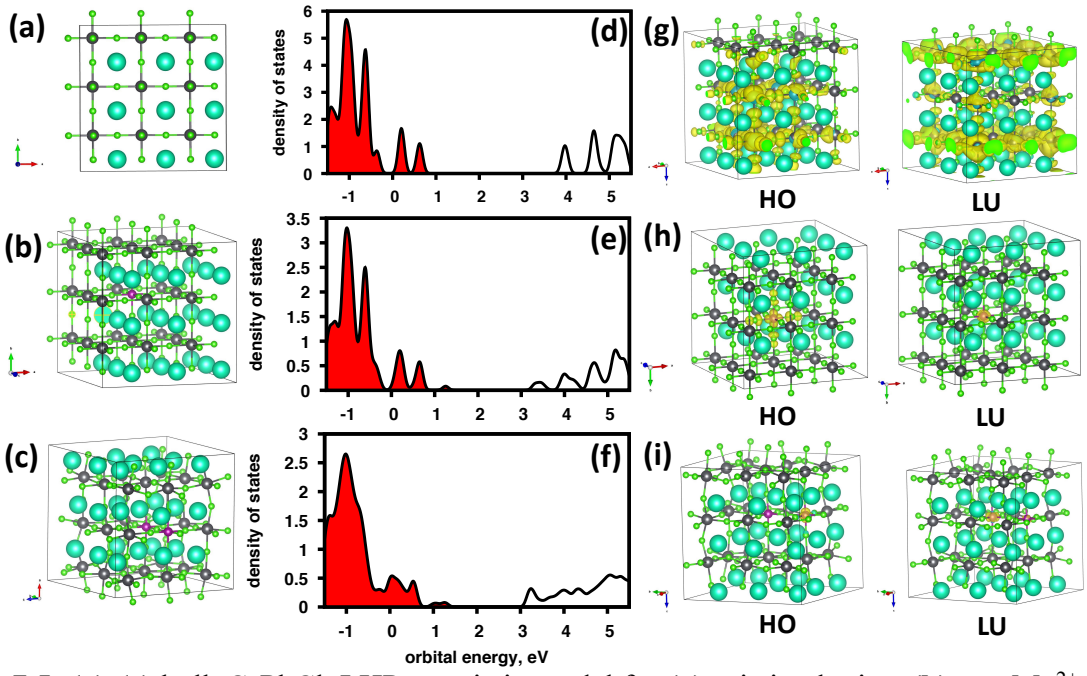

Figure 7.5: (a)-(c) bulk $CsPbCl_3$ LHP atomistic model for **(a)** pristine lattice, **(b)** one Mn^{2+} dopant, and **(c)** two Mn^{2+} dopant. **(c)-(e)** Electronic DOS for **(c)** pristine lattice, **(d)** one Mn^{2+} dopant, and **(e)** two Mn^{2+} dopant. **(g)-(i)** HO and LU KSOs **(g)** pristine lattice, **(h)** one Mn^{2+} dopant, and **(i)** two Mn^{2+} dopant.

7.3.3. Excited-State Dynamics

Next the focus will be on the photo-induced excited-state dynamics. Here the focus will be on the pristine lattices and lattices with only one Mn^{2+} dopant. Non-radiative state-to-state

transitions are found from computing non-adiabatic couplings along a MD trajectory. In **Figure 7.8(a)-(d)** the Redfield tensors, representing the state-to-state transitions, are shown for **(a)-(b)** RP phased DA_2PbCl_4 with a **(a)** pristine lattice and **(b)** with one Mn^{2+} dopant along with **(c)-(d)** 3D bulk $CsPbCl_3$ with a **(c)** the pristine lattice, and **(d)** one Mn^{2+} dopant. The x-axis and y-axis represent the KSO electronic states and the z-axis represent the transition rates in ps^{-1}. For the pristine lattices it is observed there are alternating high intensity peaks near the main diagonal and lower intensity peaks further away from the diagonal while for the Mn doped structures lack the high-intensity peaks. This is attributed to the Mn doped structures breaking the two-fold band degeneracy for pristine LHP lattices due to the ferromagnetic interactions of the dopant with the electronic bands.

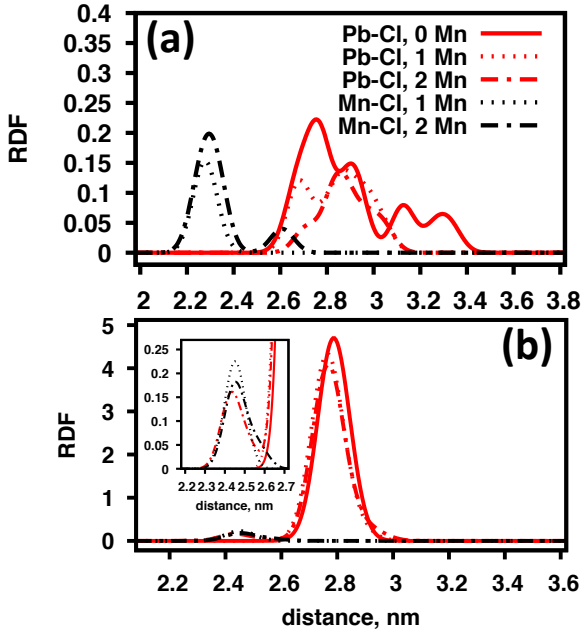

Figure 7.6: Computed partial RDF of Pb-Cl and Mn-Cl coordination for **(a)** RP phased DA_2PbCl_4 LHP and **(b)** bulk $CsPbCl_3$. For each panel the Pb-Cl coordination for pristine lattice (red, solid), with one Mn dopant (red, dotted), and with two Mn dopants (red, dash-dot) and Mn-Cl coordination for one Mn dopant (black, dotted) and two Mn dopants (black, dash-dot). In **(b)** the inset zooms in on the low intensity features between 2.2-2.7nm. For each model it is observed that the Mn-Cl coordination distances are shorter than the Pb-Cl coordination distance.

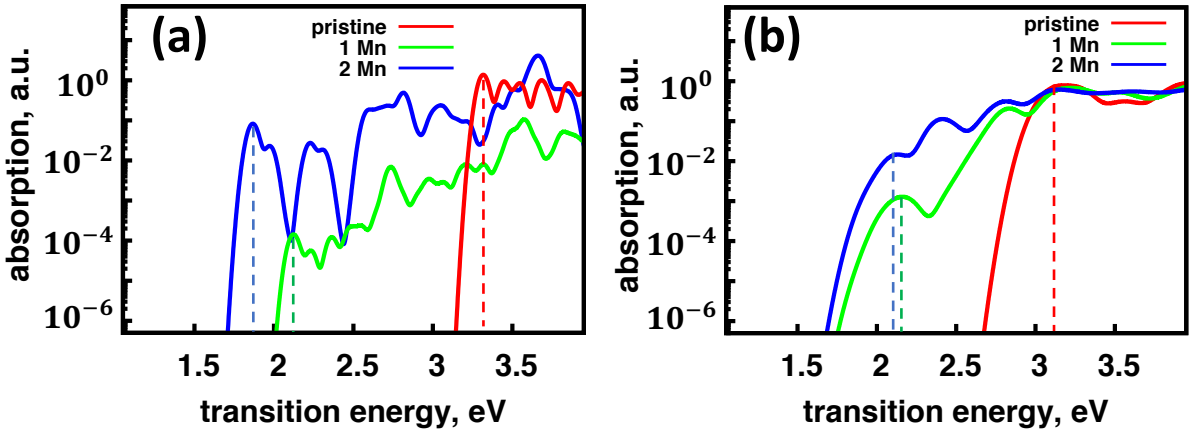

Figure 7.7: Computed absorption spectra for **(a)** RP phased DA_2PbCl_4 LHP and **(b)** bulk $CsPbCl_3$. For each panel the pristine lattice (red, solid) show wide bandgap absorption onsets above 3 eV. The Mn^{2+} doped models (1/2 Mn dopant, green/blue) show low intensity absorption onsets at transition energies near 2 eV. For both models the structures with two Mn^{2+} dopants show a red-shifted transition energy

In **Figure 7.9(a)-(c)** we show the excited-state dynamics for the 2D RP phased DA_2PbCl_4 LHP for the **(a)-(c)** pristine lattice where we show **(a)** non-radiative relaxation with **(b)** time-resolved photoluminescence and **(c)** time-integrated luminescence along the excited-state trajectory. In **Figure 7.9(d)-(f)** we show the excited-state dynamics for the Mn-doped 2D RP phased DA_2PbCl_4 LHP where **(d)** shows non-radiative relaxation with **(e)** time-resolved photoluminescence and **(f)** time-integrated luminescence along the excited-state trajectory. Comparing the non-radiative carrier-cooling of the intrinsic and doped structure it is observed that the doped structure shows sub-picosecond electron cooling (2.32 1/ps) while the cooling in the pristine structure an order of magnitude slower (0.13 1/ps), as noted in **Table 7.1.** The hot-hole cooling rates are essentially the same for both intrinsic and doped structures. For the radiative dynamics the pristine structure shows some transient PL before decaying to the band edges where it emits wide-bandgap PL whereas the Mn-doped structure shows neglectable transient signal and completely quenches the intrinsic wide-gap PL. The Mn-doped structure

results in low intensity d-d PL after the non-radiative sensitization. Overall the pristine structure shows relatively efficient PL with PLQY=35% while the d-d transitions in the doped structure shows low PLQY = 0.2%.

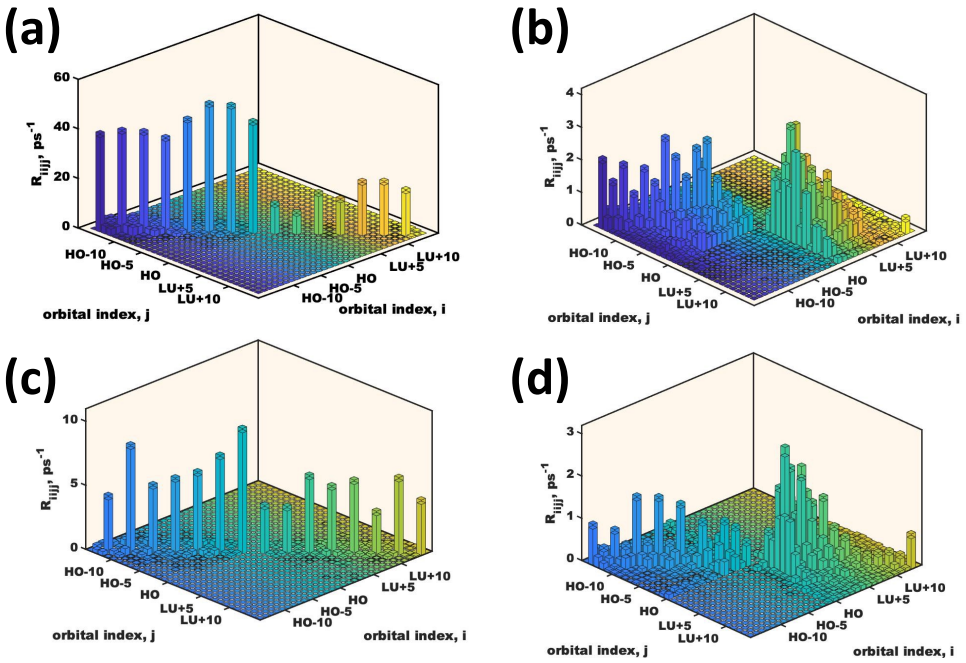

Figure 7.8: Redfield tensors for **(a)-(b)** RP phased DA_2PbCl_4 LHP with **(a)** the pristine lattice and **(b)** one Mn^{2+} doped and **(c)-(d)** bulk $CsPbCl_3$ with **(c)** pristine lattice and **(d)** one Mn^{2+} dopant.

In **Figure 7.10(a)-(c)** we show the excited-state dynamics for the 3D bulk $CsPbCl_3$ LHP for the **(a)-(c)** pristine lattice where we show **(a)** non-radiative relaxation with **(b)** time-resolved photoluminescence and **(c)** time-integrated luminescence along the excited-state trajectory. In **Figure 7.10(d)-(f)** we show the excited-state dynamics for the Mn-doped 3D bulk $CsPbCl_3$ LHP where **(d)** shows non-radiative relaxation with **(e)** time-resolved photoluminescence and **(f)** time-integrated luminescence along the excited-state trajectory. Comparing the non-radiative carrier-cooling of the intrinsic and doped structure it is observed that the doped structure shows faster electron and hole cooling, see **Table 7.1**, which is a sign of efficient sensitization of the Mn^{2+} dopant. Overall the pristine structure shows relatively efficient PL with PLQY=8% while the d-d transitions in the doped structure shows low PLQY = 0.3%.

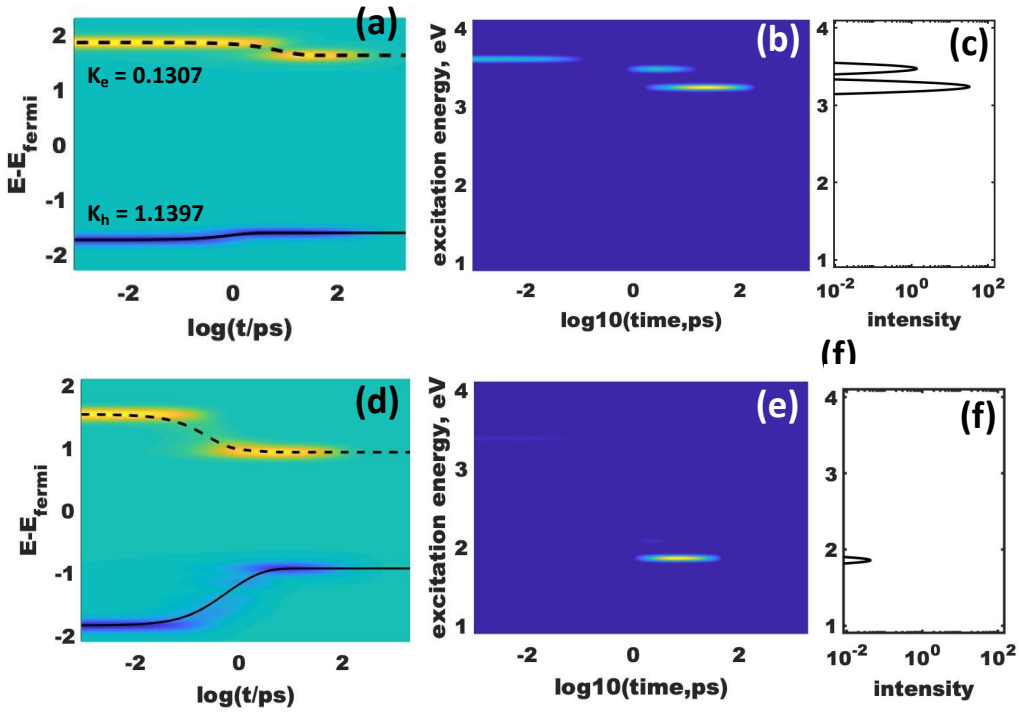

Figure 7.9: Non-radiative and radiative excited-state dynamics for RP phased DA_2PbCl_4 LHP with **(a)-(c)** the pristine lattice and **(d)-(f)** one Mn^{2+} dopant.

Table 7.1: Initial conditions for the dynamics show in Figure 7.9 and Figure 7.10 with hot-carrier cooling rates k_h/k_e, non-radiative recombination rate k_{nr} radiative recombination rate k_r ,and the resultant PLQY.

Model	HO-x	LU+y	k_h (1/ps)	k_e (1/ps)	k_{nr} (1/ns)	k_r (1/ns)	PLQY
DA_2PbCl_4 - Pristine	HO-2	LU+2	1.14	0.13	3.60	0.78	35 x 10^{-2}
DA_2PbCl_4 - Mn-Doped	HO-6	LU+5	1.08	2.32	14.3	0.005	2 x 10^{-3}
$CsPbCl_3$ - Pristine	HO-6	LU+6	0.20	0.28	1.90	0.20	8 x 10^{-2}
$CsPbCl_3$ - Mn-Doped	HO-5	LU+11	0.48	0.95	4.70	0.01	3 x 10^{-3}

For the radiative dynamics in **Figure 7.9** and **Figure 7.10** the PL linewidths are artificially narrow due to neglect of electron-phonon interactions giving vibronic progressions. In

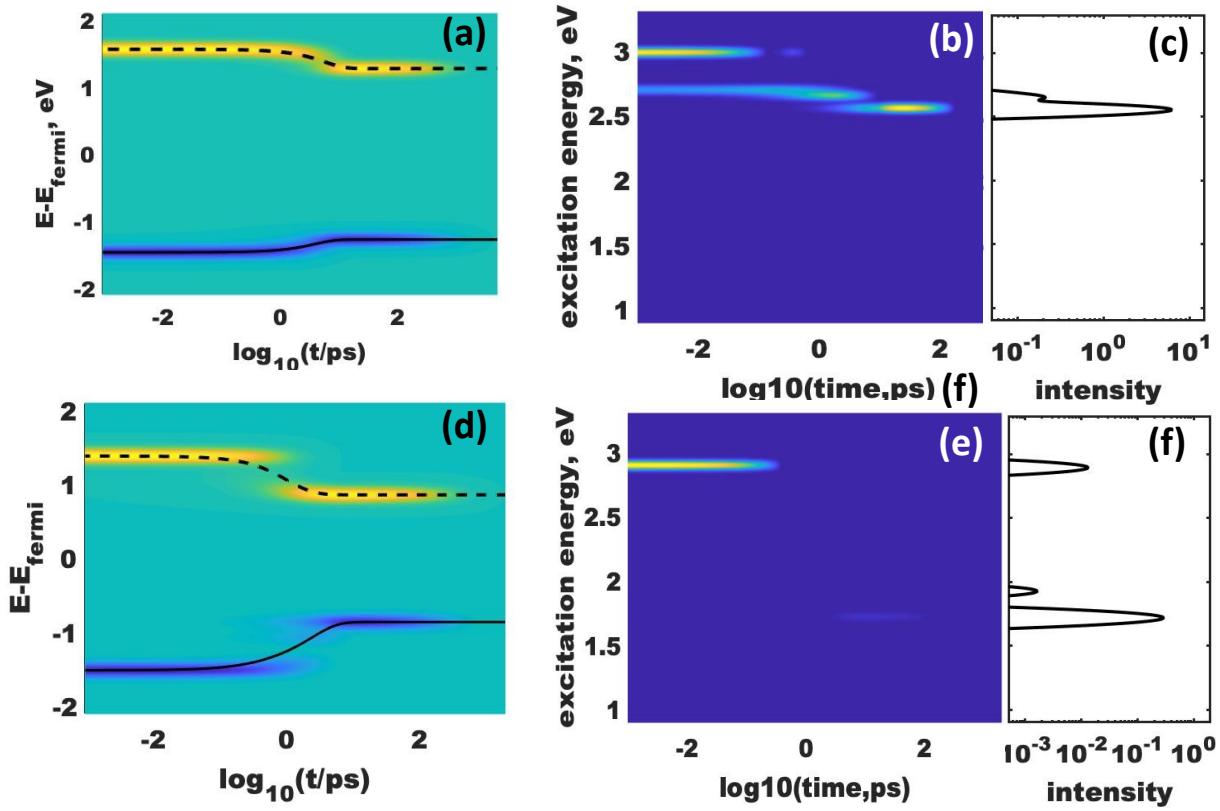

Figure 7.10: Non-radiative and radiative excited-state dynamics for bulk phased $CsPbCl_3$ LHP with **(a)-(c)** the pristine lattice and **(d)-(f)** one Mn^{2+} dopant.

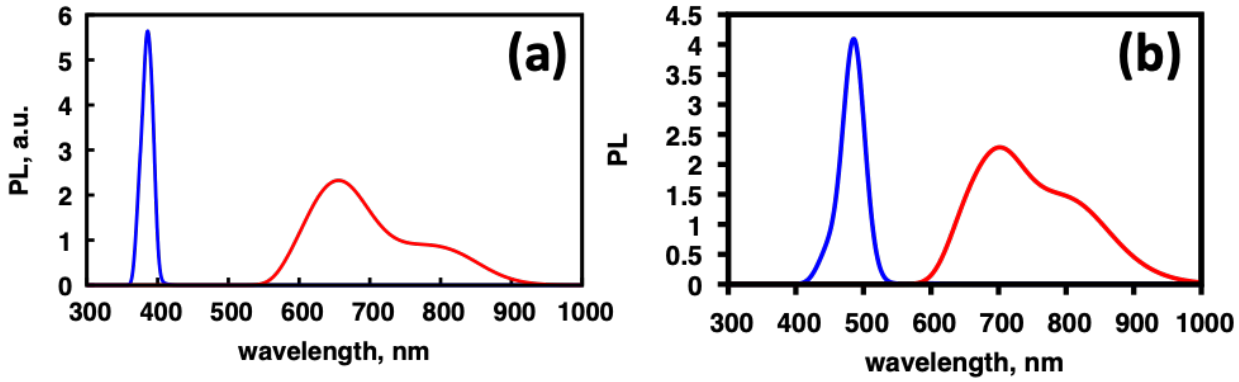

Figure 7.11: MDPL for (a) RP phased DA_2PbCl_4 LHP and (b) bulk phased $CsPbCl_3$ LHP.

experimental samples of Mn doped LHP it is observed that the intrinsic emission from the LHP lattice provides a narrow 'blue' emission and that the Mn dopant provides broadband 'red'

emission. To account for the thermal broadening of the transition energy, due to electron-phonon interactions, we implement MDPL which computes photo-physical properties, such as transition energies and oscillator strengths, along the MD trajectory. In **Figure 7.11(a)-(b)** we show the MDPL spectra for **(a)** 2D RP phased DA_2PbCl_4 and **(b)** 3D bulk $CsPbCl_3$ LHP. For both models it is observed that PL from the pristine lattice is narrow while the lattices doped with one Mn show broadband emission with extended shoulders which are red-shifted from the main peak.

7.4. Conclusion

Doping LHP nanocrystals and nanomaterials with Mn^{2+} ions shows promise for extending the photo-physical properties as spectral down-converters for broadband orange emission and dual emission from both the LHP and Mn^{2+} dopant. Here we explore the photo-physical response of Mn^{2+} dopants for various halides (chlorine, bromide) and crystal structures (bulk, 0D NC, 2D RP phase). From analyzing the energy levels of the Mn^{2+} 3d orbitals relative to the HO and LU orbitals of the LHP material it was found that the $CsPbBr_3$ and $CsPbCl_3$ NCs provide thermodynamically unfavorable alignment to give rise d-d luminescence from the dopant. In both cases the occupied Mn^{2+} 3d orbital where aligned inside the LHP bandgap, but the unoccupied states resided deep in the conduction band of the $CsPbBr_3$ NC and hybridizes with surface states for the $CsPbCl_3$ NC. But in the case of the bulk $CsPbCl_3$ lattice and 2D RP phased BA_2PbCl_4 that the Mn^{2+} states reside inside the LHP bandgap. This indicated that experimentally broadband d-d luminescence from experimental samples must come from weakly confined, larger NCs which has greater contribution form the bulk lattice.

To explore the PL properties of Mn-doped LHPs we computed excited-state dynamics simulations exploring the photo-induced excitation of the perovskite lattice which then sensitizes the Mn^{2+} dopant through non-radiative charge-transfer. Once sensitized the Mn^{2+} nonradiative

and radiative recombination dynamics are propagated with the possibility of d-d luminescence. For the Mn-doped bulk $CsPbCl_3$ there are signs of dual luminescence with a low intensity 'blue' feature from the LHP and a 'red' feature from the Mn^{2+} dopant. We also explore the PL linewidths for these models and find agreement with broadband 'red' emission from the dopant and narrow 'blue' emission from the LHP. One drawback is that the PLQY for the Mn-doped models show are low for the 2D RP phase (2×10^{-3}) and the 3D bulk (3×10^{-3}). This is attributed to the radiative and non-radiative lifetimes being much quicker (~1 ns) than what is typically observed in experiment (~1 ms). The much faster recombination rates are attributed to the single reference character of DFT which fails to enforce spin-conservation.

REFERENCES

1. Pringle, T. A.; Hunter, K. I.; Brumberg, A.; Anderson, K. J.; Fagan, J. A.; Thomas, S. A.; Petersen, R. J.; Sefannaser, M.; Han, Y.; Brown, S. L.; Kilin, D. S.; Schaller, R. D.; Kortshagen, U. R.; Boudjouk, P. R.; Hobbie, E. K., Bright Silicon Nanocrystals from a Liquid Precursor: Quasi-Direct Recombination with High Quantum Yield. *ACS Nano* **2020,** *14* (4), 3858-3867.
2. Brus, L. E., Electron–electron and electron-hole interactions in small semiconductor crystallites: The size dependence of the lowest excited electronic state. *The Journal of Chemical Physics* **1984,** *80* (9), 4403-4409.
3. Deveaud, B.; Clérot, F.; Roy, N.; Satzke, K.; Sermage, B.; Katzer, D. S., Enhanced radiative recombination of free excitons in GaAs quantum wells. *Physical Review Letters* **1991,** *67* (17), 2355-2358.
4. Cragg, G. E.; Efros, A. L., Suppression of Auger Processes in Confined Structures. *Nano Letters* **2010,** *10* (1), 313-317.
5. Chen, Y.; Vela, J.; Htoon, H.; Casson, J. L.; Werder, D. J.; Bussian, D. A.; Klimov, V. I.; Hollingsworth, J. A., "Giant" multishell CdSe nanocrystal quantum dots with suppressed blinking. *Journal of the American Chemical Society* **2008,** *130* (15), 5026-5027.
6. Lim, J.; Park, Y.-S.; Wu, K.; Yun, H. J.; Klimov, V. I., Droop-Free Colloidal Quantum Dot Light-Emitting Diodes. *Nano Letters* **2018,** *18* (10), 6645-6653.
7. Schaller, R. D.; Klimov, V. I., High efficiency carrier multiplication in PbSe nanocrystals: Implications for solar energy conversion. *Physical Review Letters* **2004,** *92* (18).
8. Ellingson, R. J.; Beard, M. C.; Johnson, J. C.; Yu, P. R.; Micic, O. I.; Nozik, A. J.; Shabaev, A.; Efros, A. L., Highly efficient multiple exciton generation in colloidal PbSe and PbS quantum dots. *Nano Letters* **2005,** *5* (5), 865-871.
9. Murphy, J. E.; Beard, M. C.; Norman, A. G.; Ahrenkiel, S. P.; Johnson, J. C.; Yu, P. R.; Micic, O. I.; Ellingson, R. J.; Nozik, A. J., PbTe colloidal nanocrystals: Synthesis, characterization, and multiple exciton generation. *Journal of the American Chemical Society* **2006,** *128* (10), 3241-3247.
10. Beard, M. C.; Knutsen, K. P.; Yu, P.; Luther, J. M.; Song, Q.; Metzger, W. K.; Ellingson, R. J.; Nozik, A. J., Multiple Exciton Generation in Colloidal Silicon Nanocrystals. *Nano Letters* **2007,** *7* (8), 2506-2512.
11. Li, M.; Begum, R.; Fu, J.; Xu, Q.; Koh, T. M.; Veldhuis, S. A.; Grätzel, M.; Mathews, N.; Mhaisalkar, S.; Sum, T. C., Low threshold and efficient multiple exciton generation in halide perovskite nanocrystals. *Nature Communications* **2018,** *9* (1), 4197.
12. Semonin, O. E.; Luther, J. M.; Choi, S.; Chen, H.-Y.; Gao, J.; Nozik, A. J.; Beard, M. C., Peak External Photocurrent Quantum Efficiency Exceeding 100% via MEG in a Quantum Dot Solar Cell. *Science* **2011,** *334* (6062), 1530.
13. Beard, M. C.; Luther, J. M.; Semonin, O. E.; Nozik, A. J., Third Generation Photovoltaics based on Multiple Exciton Generation in Quantum Confined Semiconductors. *Accounts of Chemical Research* **2013,** *46* (6), 1252-1260.
14. Nozik, A. J., Spectroscopy and hot electron relaxation dynamics in semiconductor quantum wells and quantum dots. *Annual Review of Physical Chemistry* **2001,** *52*, 193-231.

15. Klimov, V. I.; McBranch, D. W., Femtosecond 1 P-to-1S Electron Relaxation in Strongly Confined Semiconductor Nanocrystals. *Physical Review Letters* **1998,** *80* (18), 4028-4031.
16. Kilina, S. V.; Kilin, D. S.; Prezhdo, O. V., Breaking the Phonon Bottleneck in PbSe and CdSe Quantum Dots: Time-Domain Density Functional Theory of Charge Carrier Relaxation. *Acs Nano* **2009,** *3* (1), 93-99.
17. Kennehan, E. R.; Doucette, G. S.; Marshall, A. R.; Grieco, C.; Munson, K. T.; Beard, M. C.; Asbury, J. B., Electron–Phonon Coupling and Resonant Relaxation from 1D and 1P States in PbS Quantum Dots. *ACS Nano* **2018,** *12* (6), 6263-6272.
18. Wang, L.; Chen, Z.; Liang, G.; Li, Y.; Lai, R.; Ding, T.; Wu, K., Observation of a phonon bottleneck in copper-doped colloidal quantum dots. *Nature Communications* **2019,** *10* (1), 4532.
19. Rego, L. G. C.; Batista, V. S., Quantum dynamics simulations of interfacial electron transfer in sensitized TiO2 semiconductors. *Journal of the American Chemical Society* **2003,** *125* (26), 7989-7997.
20. Duncan, W. R.; Stier, W. M.; Prezhdo, O. V., Ab initio nonadiabatic molecular dynamics of the ultrafast electron injection across the alizarin-TiO2 interface. *Journal of the American Chemical Society* **2005,** *127* (21), 7941-7951.
21. Stier, W.; Prezhdo, O. V., Nonadiabatic Molecular Dynamics Simulation of Light-Induced Electron Transfer from an Anchored Molecular Electron Donor to a Semiconductor Acceptor. *The Journal of Physical Chemistry B* **2002,** *106* (33), 8047-8054.
22. Kojima, A.; Teshima, K.; Shirai, Y.; Miyasaka, T., Organometal Halide Perovskites as Visible-Light Sensitizers for Photovoltaic Cells. *Journal of the American Chemical Society* **2009,** *131* (17), 6050-6051.
23. Michael M. Lee, J. T., Tsutomu Miyasaka, Takurou N. Murakami, Henry J. Snaith, Efficient Hybrid Solar Cells Based on Meso-Superstructured Organometalic Halide Perovskites. *Science* **2012,** *338*, 643-647.
24. Nie, W.; Tsai, H.; Asadpour, R.; Blancon, J.-C.; Neukirch, A. J.; Gupta, G.; Crochet, J. J.; Chhowalla, M.; Tretiak, S.; Alam, M. A.; Wang, H.-L.; Mohite, A. D., High-efficiency solution-processed perovskite solar cells with millimeter-scale grains. *Science* **2015,** *347* (6221), 522-525.
25. Ling, X.; Zhou, S.; Yuan, J.; Shi, J.; Qian, Y.; Larson, B. W.; Zhao, Q.; Qin, C.; Li, F.; Shi, G.; Stewart, C.; Hu, J.; Zhang, X.; Luther, J. M.; Duhm, S.; Ma, W., 14.1% CsPbI3 Perovskite Quantum Dot Solar Cells via Cesium Cation Passivation. *Advanced Energy Materials* **2019,** *9* (28), 1900721.
26. Tsai, H.; Nie, W.; Blancon, J.-C.; Stoumpos, C. C.; Asadpour, R.; Harutyunyan, B.; Neukirch, A. J.; Verduzco, R.; Crochet, J. J.; Tretiak, S.; Pedesseau, L.; Even, J.; Alam, M. A.; Gupta, G.; Lou, J.; Ajayan, P. M.; Bedzyk, M. J.; Kanatzidis, M. G.; Mohite, A. D., High-efficiency two-dimensional Ruddlesden–Popper perovskite solar cells. *Nature* **2016,** *536*, 312.
27. Sun, S.; Isikgor, F. H.; Deng, Z.; Wei, F.; Kieslich, G.; Bristowe, P. D.; Ouyang, J.; Cheetham, A. K., Factors Influencing the Mechanical Properties of Formamidinium Lead Halides and Related Hybrid Perovskites. *ChemSusChem* **2017,** *10* (19), 3740-3745.

28. Zhu, X. Y.; Podzorov, V., Charge Carriers in Hybrid Organic–Inorganic Lead Halide Perovskites Might Be Protected as Large Polarons. *The Journal of Physical Chemistry Letters* **2015,** *6* (23), 4758-4761.
29. Protesescu, L.; Yakunin, S.; Bodnarchuk, M. I.; Krieg, F.; Caputo, R.; Hendon, C. H.; Yang, R. X.; Walsh, A.; Kovalenko, M. V., Nanocrystals of Cesium Lead Halide Perovskites (CsPbX(3), X = Cl, Br, and I): Novel Optoelectronic Materials Showing Bright Emission with Wide Color Gamut. *Nano Lett* **2015,** *15* (6), 3692-6.
30. Kohn, W.; Sham, L., Self-Consistent Equations Including Exchange and Correlation Effects. *Phys. Rev. A* **1965,** *140*, 1133-1138.
31. Hohenberg, P.; Kohn, W., Inhomogeneous Electron Gas. *Physical Review B* **1964,** *136* (3B), B864-B871.
32. Perdew, J. P.; Burke, K.; Ernzerhof, M., Generalized Gradient Approximation Made Simple. *Physical Review Letters* **1996,** *77* (18), 3865-3868.
33. Heyd, J.; Scuseria, G. E.; Ernzerhof, M., Hybrid functionals based on a screened Coulomb potential. *Journal of Chemical Physics* **2003,** *118* (18), 8207-8215.
34. Yanai, T.; Tew, D. P.; Handy, N. C., A new hybrid exchange-correlation functional using the Coulomb-attenuating method (CAM-B3LYP). *Chemical Physics Letters* **2004,** *393* (1-3), 51-57.
35. Sakurai, J. J.; Napolitano, J., *Modern Quantum Mechanics*. 2 ed.; Cambridge University Press: Cambridge, 2017.
36. Vogel, D. J.; Kryjevski, A.; Inerbaev, T.; Kilin, D. S., Photoinduced Single- and Multiple-Electron Dynamics Processes Enhanced by Quantum Confinement in Lead Halide Perovskite Quantum Dots. *The Journal of Physical Chemistry Letters* **2017,** *8* (13), 3032-3039.
37. Han, Y.; Meng, Q.; Rasulev, B.; May, P. S.; Berry, M. T.; Kilin, D. S., Photoinduced Charge Transfer versus Fragmentation Pathways in Lanthanum Cyclopentadienyl Complexes. *Journal of Chemical Theory and Computation* **2017,** *13* (9), 4281-4296.
38. Kilina, S.; Kilin, D.; Tretiak, S., Light-Driven and Phonon-Assisted Dynamics in Organic and Semiconductor Nanostructures. *Chemical Reviews* **2015,** *115* (12), 5929-5978.
39. Kryjevski, A.; Mihaylov, D.; Kilina, S.; Kilin, D., Multiple exciton generation in chiral carbon nanotubes: Density functional theory based computation. *The Journal of Chemical Physics* **2017,** *147* (15), 154106.
40. Vogel, D. J.; Kilin, D. S., First-Principles Treatment of Photoluminescence in Semiconductors. *Journal of Physical Chemistry C* **2015,** *119* (50), 27954-27964.
41. Kilina, S.; Kilin, D.; Tretiak, S., Light-Driven and Phonon-Assisted Dynamics in Organic and Semiconductor Nanostructures. *Chemical Reviews* **2015,** *115* ((12)), 5929–5978.
42. Einstein, A., On the Quantum Theory of Radiation. *Physikalische Zeitschrift* **1917,** *18* (121).
43. Devreese, J. T.; Alexandrov, A. S., Fröhlich polaron and bipolaron: recent developments. *Reports on Progress in Physics* **2009,** *72* (6), 066501.
44. Feynman, R. P., Slow Electrons in a Polar Crystal. *Physical Review* **1955,** *97* (3), 660-665.
45. Giustino, F., Electron-phonon interactions from first principles. *Reviews of Modern Physics* **2017,** *89* (1), 015003.
46. Han, P.; Bester, G., First-principles calculation of the electron-phonon interaction in semiconductor nanoclusters. *Physical Review B* **2012,** *85* (23).

47. Kresse, G.; Hafner, J., Ab initio molecular dynamics for liquid metals. *Physical Review B* **1993,** *47* (1), 558-561.
48. Han, Y.; Vogel, D. J.; Inerbaev, T. M.; May, P. S.; Berry, M. T.; Kilin, D. S., Photoinduced dynamics to photoluminescence in Ln3+ (Ln = Ce, Pr) doped β-NaYF4 nanocrystals computed in basis of non-collinear spin DFT with spin-orbit coupling. *Molecular Physics* **2018,** *116* (5-6), 697-707.
49. Forde, A.; Inerbaev, T.; Kilin, D., Spinor Dynamics in Pristine and Mn2+-Doped CsPbBr3 NC: Role of Spin–Orbit Coupling in Ground- and Excited-State Dynamics. *The Journal of Physical Chemistry C* **2018,** *122* (45), 26196-26213.
50. Tully, J. C., Molecular dynamics with electronic transitions. *The Journal of Chemical Physics* **1990,** *93* (2), 1061-1071.
51. Hammes-Schiffer, S.; Tully, J. C., Proton Transfer in Solution - Molecular Dynamics With Quantum Transitions. *Journal of Chemical Physics* **1994,** *101* (6), 4657-4667.
52. Kilina, S. V.; Craig, C. F.; Kilin, D. S.; Prezhdo, O. V., Ab Initio Time-Domain Study of Phonon-Assisted Relaxation of Charge Carriers in a PbSe Quantum Dot. *Journal of Physical Chemistry C* **2007,** *111* (12), 4871-4878.
53. Ben-Nun, M.; Quenneville, J.; Martinez, T. J., Ab initio multiple spawning: Photochemistry from first principles quantum molecular dynamics. *Journal of Physical Chemistry A* **2000,** *104* (22), 5161-5175.
54. Tao, H.; Levine, B. G.; Martínez, T. J., Ab Initio Multiple Spawning Dynamics Using Multi-State Second-Order Perturbation Theory. *J. Phys. Chem. A* **2009,** *113* (49), 13656-13662.
55. Travis, W.; Glover, E. N. K.; Bronstein, H.; Scanlon, D. O.; Palgrave, R. G., On the application of the tolerance factor to inorganic and hybrid halide perovskites: a revised system. *Chemical Science* **2016,** *7* (7), 4548-4556.
56. Saparov, B.; Mitzi, D. B., Organic–Inorganic Perovskites: Structural Versatility for Functional Materials Design. *Chemical Reviews* **2016,** *116* (7), 4558-4596.
57. Zhang, D.; Yu, Y.; Bekenstein, Y.; Wong, A. B.; Alivisatos, A. P.; Yang, P., Ultrathin Colloidal Cesium Lead Halide Perovskite Nanowires. *J Am Chem Soc* **2016,** *138* (40), 13155-13158.
58. Efros, A. L.; Rosen, M., The Electronic Structure of Semiconductor Nanocrystals. *Annual Review of Materials Science* **2000,** *30* (1), 475-521.
59. Brus, L., Electronic wave functions in semiconductor clusters: experiment and theory. *The Journal of Physical Chemistry* **1986,** *90* (12), 2555-2560.
60. Beard, M. C.; Luther, J. M.; Nozik, A. J., The promise and challenge of nanostructured solar cells. *Nature Nanotechnology* **2014,** *9*, 951.
61. He, J.; Vasenko, A. S.; Long, R.; Prezhdo, O. V., Halide Composition Controls Electron–Hole Recombination in Cesium–Lead Halide Perovskite Quantum Dots: A Time Domain Ab Initio Study. *The Journal of Physical Chemistry Letters* **2018,** *9* (8), 1872-1879.
62. Madjet, M. E.; Berdiyorov, G. R.; El-Mellouhi, F.; Alharbi, F. H.; Akimov, A. V.; Kais, S., Cation Effect on Hot Carrier Cooling in Halide Perovskite Materials. *The Journal of Physical Chemistry Letters* **2017,** *8* (18), 4439-4445.
63. Hopper, T. R.; Gorodetsky, A.; Frost, J. M.; Müller, C.; Lovrincic, R.; Bakulin, A. A., Ultrafast Intraband Spectroscopy of Hot-Carrier Cooling in Lead-Halide Perovskites. *ACS Energy Letters* **2018,** *3* (9), 2199-2205.

64. Evans, T. J. S.; Miyata, K.; Joshi, P. P.; Maehrlein, S.; Liu, F.; Zhu, X. Y., Competition Between Hot-Electron Cooling and Large Polaron Screening in CsPbBr3 Perovskite Single Crystals. *The Journal of Physical Chemistry C* **2018,** *122* (25), 13724-13730.
65. Park, M.; Neukirch, A. J.; Reyes-Lillo, S. E.; Lai, M.; Ellis, S. R.; Dietze, D.; Neaton, J. B.; Yang, P.; Tretiak, S.; Mathies, R. A., Excited-state vibrational dynamics toward the polaron in methylammonium lead iodide perovskite. *Nature Communications* **2018,** *9* (1), 2525.
66. Miyata, K.; Meggiolaro, D.; Trinh, M. T.; Joshi, P. P.; Mosconi, E.; Jones, S. C.; De Angelis, F.; Zhu, X. Y., Large polarons in lead halide perovskites. *Science Advances* **2017,** *3* (8).
67. Li, M.; Bhaumik, S.; Goh, T. W.; Kumar, M. S.; Yantara, N.; Grätzel, M.; Mhaisalkar, S.; Mathews, N.; Sum, T. C., Slow cooling and highly efficient extraction of hot carriers in colloidal perovskite nanocrystals. *Nature Communications* **2017,** *8*, 14350.
68. Becker, M. A.; Vaxenburg, R.; Nedelcu, G.; Sercel, P. C.; Shabaev, A.; Mehl, M. J.; Michopoulos, J. G.; Lambrakos, S. G.; Bernstein, N.; Lyons, J. L.; Stöferle, T.; Mahrt, R. F.; Kovalenko, M. V.; Norris, D. J.; Rainò, G.; Efros, A. L., Bright triplet excitons in caesium lead halide perovskites. *Nature* **2018,** *553*, 189.
69. Kang, J.; Wang, L.-W., High Defect Tolerance in Lead Halide Perovskite CsPbBr3. *The Journal of Physical Chemistry Letters* **2017,** *8* (2), 489-493.
70. Walsh, A.; Scanlon, D. O.; Chen, S.; Gong, X. G.; Wei, S.-H., Self-Regulation Mechanism for Charged Point Defects in Hybrid Halide Perovskites. *Angewandte Chemie International Edition* **2014,** *54* (6), 1791-1794.
71. Even, J.; Pedesseau, L.; Jancu, J.-M.; Katan, C., Importance of Spin–Orbit Coupling in Hybrid Organic/Inorganic Perovskites for Photovoltaic Applications. *The Journal of Physical Chemistry Letters* **2013,** *4* (17), 2999-3005.
72. Umari, P.; Mosconi, E.; De Angelis, F., Relativistic GW calculations on CH3NH3PbI3 and CH3NH3SnI3 Perovskites for Solar Cell Applications. *Scientific Reports* **2014,** *4*.
73. Li, W.; Zhou, L.; Prezhdo, O. V.; Akimov, A. V., Spin–Orbit Interactions Greatly Accelerate Nonradiative Dynamics in Lead Halide Perovskites. *ACS Energy Letters* **2018,** *3* (9), 2159-2166.
74. Perdew, J. P.; Burke, K.; Ernzerhof, M., Generalized Gradient Approximation Made Simple [Phys. Rev. Lett. 77, 3865 (1996)]. *Phys. Rev. Lett.* **1997,** *78* (7), 1396-1396.
75. Blöchl, P. E., Projector augmented-wave method. *Physical Review B* **1994,** *50* (24), 17953-17979.
76. Kresse, G.; Joubert, D., From ultrasoft pseudopotentials to the projector augmented-wave method. *Physical Review B* **1999,** *59* (3), 1758-1775.
77. Kresse, G.; Furthmuller, J., Efficiency of ab-initio total energy calculations for metals and semiconductors using a plane-wave basis set. *Computational Materials Science* **1996,** *6* (1), 15-50.
78. Kilina, S.; Ivanov, S.; Tretiak, S., Effect of Surface Ligands on Optical and Electronic Spectra of Semiconductor Nanoclusters. *Journal of the American Chemical Society* **2009,** *131* (22), 7717-7726.
79. Makarov, N. S.; Guo, S.; Isaienko, O.; Liu, W.; Robel, I.; Klimov, V. I., Spectral and Dynamical Properties of Single Excitons, Biexcitons, and Trions in Cesium-Lead-Halide Perovskite Quantum Dots. *Nano Lett* **2016,** *16* (4), 2349-62.

80. Brennan, M. C.; Herr, J. E.; Nguyen-Beck, T. S.; Zinna, J.; Draguta, S.; Rouvimov, S.; Parkhill, J.; Kuno, M., Origin of the Size-Dependent Stokes Shift in CsPbBr3 Perovskite Nanocrystals. *Journal of the American Chemical Society* **2017,** *139* (35), 12201-12208.
81. Maes, J.; Balcaen, L.; Drijvers, E.; Zhao, Q.; De Roo, J.; Vantomme, A.; Vanhaecke, F.; Geiregat, P.; Hens, Z., Light Absorption Coefficient of CsPbBr3 Perovskite Nanocrystals. *The Journal of Physical Chemistry Letters* **2018,** *9* (11), 3093-3097.
82. Telfah, H.; Jamhawi, A.; Teunis, M. B.; Sardar, R.; Liu, J., Ultrafast Exciton Dynamics in Shape-Controlled Methylammonium Lead Bromide Perovskite Nanostructures: Effect of Quantum Confinement on Charge Carrier Recombination. *The Journal of Physical Chemistry C* **2017,** *121* (51), 28556-28565.
83. Chung, H.; Jung, S. I.; Kim, H. J.; Cha, W.; Sim, E.; Kim, D.; Koh, W.-K.; Kim, J., Composition-Dependent Hot Carrier Relaxation Dynamics in Cesium Lead Halide (CsPbX3, X=Br and I) Perovskite Nanocrystals. *Angewandte Chemie International Edition* **2017,** *56* (15), 4160-4164.
84. Vogel, D. J.; Kilin, D. S., First-Principles Treatment of Photoluminescence in Semiconductors. *The Journal of Physical Chemistry C* **2015,** *119* (50), 27954-27964.
85. Krieg, F.; Ochsenbein, S. T.; Yakunin, S.; ten Brinck, S.; Aellen, P.; Süess, A.; Clerc, B.; Guggisberg, D.; Nazarenko, O.; Shynkarenko, Y.; Kumar, S.; Shih, C.-J.; Infante, I.; Kovalenko, M. V., Colloidal CsPbX3 (X = Cl, Br, I) Nanocrystals 2.0: Zwitterionic Capping Ligands for Improved Durability and Stability. *ACS Energy Letters* **2018,** *3* (3), 641-646.
86. Filip, M. R.; Giustino, F., GW quasiparticle band gap of the hybrid organic-inorganic perovskite CH3NH3PbI3: Effect of spin-orbit interaction, semicore electrons, and self-consistency. *Physical Review B* **2014,** *90* (24).
87. Isarov, M.; Tan, L. Z.; Bodnarchuk, M. I.; Kovalenko, M. V.; Rappe, A. M.; Lifshitz, E., Rashba Effect in a Single Colloidal CsPbBr3 Perovskite Nanocrystal Detected by Magneto-Optical Measurements. *Nano Letters* **2017,** *17* (8), 5020-5026.
88. Mosconi, E.; Etienne, T.; De Angelis, F., Rashba Band Splitting in Organohalide Lead Perovskites: Bulk and Surface Effects. *J Phys Chem Lett* **2017,** *8* (10), 2247-2252.
89. Kilina, S.; Velizhanin, K. A.; Ivanov, S.; Prezhdo, O. V.; Tretiak, S., Surface Ligands Increase Photoexcitation Relaxation Rates in CdSe Quantum Dots. *Acs Nano* **2012,** *6* (7), 6515-6524.
90. Yazdani, N.; Bozyigit, D.; Vuttivorakulchai, K.; Luisier, M.; Infante, I.; Wood, V., Tuning Electron–Phonon Interactions in Nanocrystals through Surface Termination. *Nano Letters* **2018,** *18* (4), 2233-2242.
91. Lu, H.; Carroll, G. M.; Neale, N. R.; Beard, M. C., Infrared Quantum Dots: Progress, Challenges, and Opportunities. *ACS Nano* **2019,** *13* (2), 939-953.
92. Steenbergen, E. H.; Connelly, B. C.; Metcalfe, G. D.; Shen, H.; Wraback, M.; Lubyshev, D.; Qiu, Y.; Fastenau, J. M.; Liu, A. W. K.; Elhamri, S.; Cellek, O. O.; Zhang, Y. H., Significantly improved minority carrier lifetime observed in a long-wavelength infrared III-V type-II superlattice comprised of InAs/InAsSb. *Applied Physics Letters* **2011,** *99* (25), 251110.
93. Lei, W.; Antoszewski, J.; Faraone, L., Progress, challenges, and opportunities for HgCdTe infrared materials and detectors. *Applied Physics Reviews* **2015,** *2* (4), 041303.
94. Saha, A.; Gifford, B. J.; He, X.; Ao, G.; Zheng, M.; Kataura, H.; Htoon, H.; Kilina, S.; Tretiak, S.; Doorn, S. K., Narrow-band single-photon emission through selective aryl

functionalization of zigzag carbon nanotubes. *Nature Chemistry* **2018,** *10* (11), 1089-1095.
95. Katan, C.; Mercier, N.; Even, J., Quantum and Dielectric Confinement Effects in Lower-Dimensional Hybrid Perovskite Semiconductors. *Chemical Reviews* **2019,** *119* (5), 3140-3192.
96. Keldysh, L. V., Coulomb interaction in thin semiconductor and semimetal films. *JETP Letters* **1979,** *29* (11), 658.
97. Chen, G.; Tien, C. L., Thermal conductivities of quantum well structures. *Journal of Thermophysics and Heat Transfer* **1993,** *7* (2), 311-318.
98. Zhang, D.; Eaton, S. W.; Yu, Y.; Dou, L.; Yang, P., Solution-Phase Synthesis of Cesium Lead Halide Perovskite Nanowires. *Journal of the American Chemical Society* **2015,** *137* (29), 9230-9233.
99. Stranks, S. D.; Snaith, H. J., Metal-halide perovskites for photovoltaic and light-emitting devices. *Nature Nanotechnology* **2015,** *10*, 391.
100. Neukirch, A. J.; Nie, W.; Blancon, J.-C.; Appavoo, K.; Tsai, H.; Sfeir, M. Y.; Katan, C.; Pedesseau, L.; Even, J.; Crochet, J. J.; Gupta, G.; Mohite, A. D.; Tretiak, S., Polaron Stabilization by Cooperative Lattice Distortion and Cation Rotations in Hybrid Perovskite Materials. *Nano Letters* **2016,** *16* (6), 3809-3816.
101. Kartheuser, E.; Evrard, R.; Devreese, J., Mechanism of Absorption of Light by Free Continuum Polarons. *Physical Review Letters* **1969,** *22* (3), 94-97.
102. Emin, D., Optical properties of large and small polarons and bipolarons. *Physical Review B* **1993,** *48* (18), 13691-13702.
103. Munson, K. T.; Kennehan, E. R.; Doucette, G. S.; Asbury, J. B., Dynamic Disorder Dominates Delocalization, Transport, and Recombination in Halide Perovskites. *Chem* **2018,** *4* (12), 2826-2843.
104. Munson, K. T.; Doucette, G. S.; Kennehan, E. R.; Swartzfager, J. R.; Asbury, J. B., Vibrational Probe of the Structural Origins of Slow Recombination in Halide Perovskites. *The Journal of Physical Chemistry C* **2019,** *123* (12), 7061-7073.
105. Forde, A.; Inerbaev, T.; Hobbie, E. K.; Kilin, D. S., Excited-State Dynamics of a CsPbBr3 Nanocrystal Terminated with Binary Ligands: Sparse Density of States with Giant Spin–Orbit Coupling Suppresses Carrier Cooling. *Journal of the American Chemical Society* **2019,** *141* (10), 4388-4397.
106. Vogel, D. J.; Kryjevski, A.; Inerbaev, T. M.; Kilin, D. S.; , Photoinduced Single- and Multiple- Electron Dynamics Processes Enhanced by Quantum Confinement in Lead Halide Perovskite Quantum Dots. *The Journal of Physical Chemistry Letters* **2017,** 8 (13), 3032–3039
107. Inerbaev, T. M.; Hoefelmeyer, J. D.; Kilin, D. S., Photoinduced Charge Transfer from Titania to Surface Doping Site. *The Journal of Physical Chemistry C* **2013,** *117* (19), 9673-9692.
108. Barth, U. v.; Hedin, L., A local exchange-correlation potential for the spin polarized case. i. *Journal of Physics C: Solid State Physics* **1972,** *5* (13), 1629-1642.
109. Kubler, J.; Hock, K. H.; Sticht, J.; Williams, A. R., DENSITY FUNCTIONAL THEORY OF NON-COLLINEAR MAGNETISM. *Journal of Physics F-Metal Physics* **1988,** *18* (3), 469-483.

110. Yao, G.; Berry, M.; May, P. S.; Wang, J.; Kilin, D. S., Relationship between Site Symmetry, Spin State, and Doping Concentration for Co(II) or Co(III) in β-NaYF4. *The Journal of Physical Chemistry C* **2016,** *120* (14), 7785-7794.
111. Neukirch, A. J.; Abate, I. I.; Zhou, L.; Nie, W.; Tsai, H.; Pedesseau, L.; Even, J.; Crochet, J. J.; Mohite, A. D.; Katan, C.; Tretiak, S., Geometry Distortion and Small Polaron Binding Energy Changes with Ionic Substitution in Halide Perovskites. *The Journal of Physical Chemistry Letters* **2018,** *9* (24), 7130-7136.
112. Buin, A.; Pietsch, P.; Xu, J.; Voznyy, O.; Ip, A. H.; Comin, R.; Sargent, E. H., Materials Processing Routes to Trap-Free Halide Perovskites. *Nano Letters* **2014,** *14* (11), 6281-6286.
113. Meggiolaro, D.; Ambrosio, F.; Mosconi, E.; Mahata, A.; De Angelis, F., Polarons in Metal Halide Perovskites. *Advanced Energy Materials* **2019,** *n/a* (n/a), 1902748.
114. Poncé, S.; Schlipf, M.; Giustino, F., Origin of Low Carrier Mobilities in Halide Perovskites. *ACS Energy Letters* **2019,** *4* (2), 456-463.
115. Chu, W.; Zheng, Q.; Prezhdo, O. V.; Zhao, J.; Saidi, W. A., Low-frequency lattice phonons in halide perovskites explain high defect tolerance toward electron-hole recombination. *Science Advances* **2020,** *6* (7), eaaw7453.
116. ten Brinck, S.; Zaccaria, F.; Infante, I., Defects in Lead Halide Perovskite Nanocrystals: Analogies and (Many) Differences with the Bulk. *ACS Energy Letters* **2019,** *4* (11), 2739-2747.
117. Perez, C. M.; Ghosh, D.; Prezhdo, O.; Tretiak, S.; Neukirch, A. J., Excited-State Properties of Defected Halide Perovskite Quantum Dots: Insights from Computation. *The Journal of Physical Chemistry Letters* **2021,** *12* (3), 1005-1011.
118. Kim, Y.; Yassitepe, E.; Voznyy, O.; Comin, R.; Walters, G.; Gong, X.; Kanjanaboos, P.; Nogueira, A. F.; Sargent, E. H., Efficient Luminescence from Perovskite Quantum Dot Solids. *ACS Appl Mater Interfaces* **2015,** *7* (45), 25007-13.
119. Yan, F.; Xing, J.; Xing, G.; Quan, L.; Tan, S. T.; Zhao, J.; Su, R.; Zhang, L.; Chen, S.; Zhao, Y.; Huan, A.; Sargent, E. H.; Xiong, Q.; Demir, H. V., Highly Efficient Visible Colloidal Lead-Halide Perovskite Nanocrystal Light-Emitting Diodes. *Nano Letters* **2018,** *18* (5), 3157-3164.
120. Forde, A.; Hobbie, E.; Kilin, D., Role of Pb2+ Adsorbents on the Opto-Electronic Properties of a CsPbBr3 Nanocrystal: A DFT Study. *MRS Advances* **2019,** *4* (36), 1981-1988.
121. Bodnarchuk, M. I.; Boehme, S. C.; ten Brinck, S.; Bernasconi, C.; Shynkarenko, Y.; Krieg, F.; Widmer, R.; Aeschlimann, B.; Günther, D.; Kovalenko, M. V.; Infante, I., Rationalizing and Controlling the Surface Structure and Electronic Passivation of Cesium Lead Halide Nanocrystals. *ACS Energy Letters* **2019,** *4* (1), 63-74.
122. Forde, A.; Inerbaev, T.; Kilin, D., Spectral Signatures of Positive and Negative Polarons in Lead-Halide Perovskite Nanocrystals. *The Journal of Physical Chemistry C* **2020,** *124* (1), 1027-1041.
123. Boehme, S. C.; Brinck, S. t.; Maes, J.; Yazdani, N.; Zapata, F.; Chen, K.; Wood, V.; Hodgkiss, J. M.; Hens, Z.; Geiregat, P.; Infante, I., Phonon-Mediated and Weakly Size-Dependent Electron and Hole Cooling in CsPbBr3 Nanocrystals Revealed by Atomistic Simulations and Ultrafast Spectroscopy. *Nano Letters* **2020,** *20* (3), 1819-1829.

124. Li, W.; Long, R.; Tang, J.; Prezhdo, O. V., Influence of Defects on Excited-State Dynamics in Lead Halide Perovskites: Time-Domain ab Initio Studies. *The Journal of Physical Chemistry Letters* **2019,** *10* (13), 3788-3804.
125. Almeida, G.; Goldoni, L.; Akkerman, Q.; Dang, Z.; Khan, A. H.; Marras, S.; Moreels, I.; Manna, L., Role of Acid–Base Equilibria in the Size, Shape, and Phase Control of Cesium Lead Bromide Nanocrystals. *ACS Nano* **2018,** *12* (2), 1704-1711.
126. Frost, J. M.; Butler, K. T.; Brivio, F.; Hendon, C. H.; van Schilfgaarde, M.; Walsh, A., Atomistic Origins of High-Performance in Hybrid Halide Perovskite Solar Cells. *Nano Letters* **2014,** *14* (5), 2584-2590.
127. Amat, A.; Mosconi, E.; Ronca, E.; Quarti, C.; Umari, P.; Nazeeruddin, M. K.; Grätzel, M.; De Angelis, F., Cation-Induced Band-Gap Tuning in Organohalide Perovskites: Interplay of Spin–Orbit Coupling and Octahedra Tilting. *Nano Letters* **2014,** *14* (6), 3608-3616.
128. Quarti, C.; Mosconi, E.; De Angelis, F., Interplay of Orientational Order and Electronic Structure in Methylammonium Lead Iodide: Implications for Solar Cell Operation. *Chemistry of Materials* **2014,** *26* (22), 6557-6569.
129. Kennehan, E. R.; Munson, K. T.; Doucette, G. S.; Marshall, A. R.; Beard, M. C.; Asbury, J. B., Dynamic Ligand Surface Chemistry of Excited PbS Quantum Dots. *The Journal of Physical Chemistry Letters* **2020,** *11* (6), 2291-2297.
130. De Roo, J.; Ibanez, M.; Geiregat, P.; Nedelcu, G.; Walravens, W.; Maes, J.; Martins, J. C.; Van Driessche, I.; Kovalenko, M. V.; Hens, Z., Highly Dynamic Ligand Binding and Light Absorption Coefficient of Cesium Lead Bromide Perovskite Nanocrystals. *ACS Nano* **2016,** *10* (2), 2071-81.
131. Quarta, D.; Imran, M.; Capodilupo, A.-L.; Petralanda, U.; van Beek, B.; De Angelis, F.; Manna, L.; Infante, I.; De Trizio, L.; Giansante, C., Stable Ligand Coordination at the Surface of Colloidal CsPbBr3 Nanocrystals. *The Journal of Physical Chemistry Letters* **2019,** *10* (13), 3715-3726.
132. Forde, A.; Fagan, J. A.; Schaller, R. D.; Thomas, S. A.; Brown, S. L.; Kurtti, M. B.; Petersen, R. J.; Kilin, D. S.; Hobbie, E. K., Brightly Luminescent CsPbBr3 Nanocrystals through Ultracentrifugation. *The Journal of Physical Chemistry Letters* **2020,** *11* (17), 7133-7140.
133. Li, J.; Gan, L.; Fang, Z.; He, H.; Ye, Z., Bright Tail States in Blue-Emitting Ultrasmall Perovskite Quantum Dots. *The Journal of Physical Chemistry Letters* **2017,** *8* (24), 6002-6008.
134. Brennan, M. C.; Forde, A.; Zhukovskyi, M.; Baublis, A. J.; Morozov, Y. V.; Zhang, S.; Zhang, Z.; Kilin, D. S.; Kuno, M., Universal Size-Dependent Stokes Shifts in Lead Halide Perovskite Nanocrystals. *The Journal of Physical Chemistry Letters* **2020**, 4937-4944.
135. Norris, D. J.; Efros, A. L.; Erwin, S. C., Doped nanocrystals. *Science* **2008,** *319* (5871), 1776-1779.
136. Sahu, A.; Kang, M. S.; Kompch, A.; Notthoff, C.; Wills, A. W.; Deng, D.; Winterer, M.; Frisbie, C. D.; Norris, D. J., Electronic Impurity Doping in CdSe Nanocrystals. *Nano Letters* **2012,** *12* (5), 2587-2594.
137. Kramer, K. W.; Biner, D.; Frei, G.; Gudel, H. U.; Hehlen, M. P.; Luthi, S. R., Hexagonal sodium yttrium fluoride based green and blue emitting upconversion phosphors. *Chemistry of Materials* **2004,** *16* (7), 1244-1251.

138. Zhang, F.; Wan, Y.; Yu, T.; Zhang, F.; Shi, Y.; Xie, S.; Li, Y.; Xu, L.; Tu, B.; Zhao, D., Uniform Nanostructured Arrays of Sodium Rare-Earth Fluorides for Highly Efficient Multicolor Upconversion Luminescence. *Angewandte Chemie International Edition* **2007,** *46* (42), 7976-7979.
139. Soo, Y. L.; Ming, Z. H.; Huang, S. W.; Kao, Y. H.; Bhargava, R. N.; Gallagher, D., Local structures around Mn luminescent centers in Mn-doped nanocrystals of ZnS. *Physical Review B* **1994,** *50* (11), 7602-7607.
140. Milstein, T. J.; Kroupa, D. M.; Gamelin, D. R., Picosecond Quantum Cutting Generates Photoluminescence Quantum Yields Over 100% in Ytterbium-Doped CsPbCl3 Nanocrystals. *Nano Letters* **2018,** *18* (6), 3792-3799.
141. Vlaskin, V. A.; Janssen, N.; van Rijssel, J.; Beaulac, R.; Gamelin, D. R., Tunable Dual Emission in Doped Semiconductor Nanocrystals. *Nano Letters* **2010,** *10* (9), 3670-3674.
142. Liu, W.; Lin, Q.; Li, H.; Wu, K.; Robel, I.; Pietryga, J. M.; Klimov, V. I., Mn2+-Doped Lead Halide Perovskite Nanocrystals with Dual-Color Emission Controlled by Halide Content. *J Am Chem Soc* **2016,** *138* (45), 14954-14961.
143. Parobek, D.; Roman, B. J.; Dong, Y.; Jin, H.; Lee, E.; Sheldon, M.; Son, D. H., Exciton-to-dopant energy transfer in Mn-doped cesium lead halide perovskite nanocrystals. *Nano Lett.* **2016,** *16*, 7376.
144. Erwin, S. C.; Zu, L. J.; Haftel, M. I.; Efros, A. L.; Kennedy, T. A.; Norris, D. J., Doping semiconductor nanocrystals. *Nature* **2005,** *436* (7047), 91-94.
145. Proshchenko, V.; Dahnovsky, Y., Tunable Luminescence in CdSe Quantum Dots Doped by Mn Impurities. *The Journal of Physical Chemistry C* **2014,** *118* (48), 28314-28321.